Florian Mayer, BSc

Electronic Couplings in Molecular Crystals: Development and Benchmarking of Advanced Strategies

MASTER'S THESIS

to achieve the university degree of

Diplom-Ingenieur

Master's degree programme: Technical Physics

submitted to

Graz University of Technology

Supervisor

Ao.Univ.-Prof. Dipl.-Ing. Dr.techn. Egbert Zojer

Institute of Solid State Physics

Graz, May 2019

AFFIDAVIT

I declare that I have authored this thesis independently, that I have not used other than the declared sources/resources, and that I have explicitly indicated all material which has been quoted either literally or by content from the sources used. The text document uploaded to TUGRAZonline is identical to the present master's thesis.

_____   _____
Date   Signature

Abstract

The applicability of materials in electronic devices depends mostly on their charge transport properties. The description of charge transport on a microscopic level requires a quantum mechanical treatment. In general transport mechanisms can be divided into two limiting regimes, namely band- and hopping transport. For the latter, a great variety of models has been developed in recent years. However, the description requires different parameters, whereby electronic couplings play a major role. Due to the importance of those couplings this thesis is dedicated to their calculation by quantum mechanical methods. The different approaches are discussed, implemented and benchmarked. These include the simple Electronic Splitting in Dimers method and the well-known Fragment Orbital approach, representing cluster-based approaches. Beyond that, this work presents also the development of two new methodologies. The first one, called Block Decomposition, allows to accurately estimate electronic couplings with reduced computational effort. Furthermore, different validation steps are shown to demonstrate the functionality of the above-mentioned implementations. Notably, cluster-based methodologies just serve as approximation for electronic couplings in periodic structures. Therefore, an alternative approach is pursued with the application of tight-binding fits. The use of suitable tight-binding functions to fit electronic band structures provides an alternative way for estimating electronic couplings. This concept includes the 3D chemical environment of the molecules in contrast to simple dimer approaches. The algorithms developed in this work are tested on quinacridone and pentacene, where the results of the tight-binding fits are also compared to the outcome of cluster-based methods.

Kurzfassung

Die Einsatzmöglichkeit von Materialien in elektronischen Bauteilen ist großteils durch deren Eigenschaften gegeben. Einen wesentlichen Faktor spielt dabei die Fähigkeit einer Substanz Ladung transportieren zu können. Diese Transporteigenschaft beruht auf mikroskopischen Prozessen, welche in weiterer Folge in Band- und Hopping-transport unterteilt werden können. Für beide Mechanismen ist die elektronische Struktur eines Materials ausschlaggebend. Das Verhalten von Bandtransport ist maßgeblich durch die Dispersion der elektronischen Bänder bestimmt. Im Gegensatz dazu, wird für die Beschreibung von Hopping-Transport, die elektronische Kopplung zwischen den einzelnen Gitterplätzen benötigt. Diese Arbeit widmet sich verschiedenen Methoden und Ansätzen zur Bestimmung dieses wichtigen Parameters. Zu diesem Zweck, werden zuerst bereits etablierte Konzepte, wie die einfache Electronic Splitting in Dimers Methode und der Fragment Orbital Ansatz, getestet. Aufbauend auf Überlegungen zu diesen Methoden wird die Entwicklung eines neuen Konzepts, genannt Block Decomposition, gezeigt. Zur Validierung dieser implementierten Ansätze, wurden sie auf verschiedenen organischen Materialien angewendet. Das Ziel dieser Arbeit ist allerdings die akkurate Beschreibung von elektronischen Kopplungen in molekularen Kristallen. Die obengenannten Methoden sind in vielen Fällen ausreichend um diese Kopplungen anzunähern, jedoch inkludieren sie nicht die periodische Umgebung der Materialien. Aus diesem Grund wird ein alternativer Ansatz gezeigt, welcher auf dem Tight-Binding Konzept beruht. Die wesentliche Idee besteht dabei aus der Herleitung einer geeigneten Modelfunktion, welche in weiterer Folge an die mittels Dichtefunktionaltheorie berechnete elektronische Bandstruktur gefittet wird. Durch dieses Vorgehen können elektronische Kopplungen für die periodischen Struktur extrahiert werden. Die Zuverlässigkeit dieses Konzept wird an zwei organischen Molekülkristallen, Quinacridone und Pentacene, getestet. Ferner, werden die Resultate der Tight-Binding Methode mit den Ergebnissen der oben genannten clusterbasierten Methoden verglichen.

Acknowledgements

First of all, I want to thank Prof. Egbert Zojer for giving me the opportunity to work in his group. The working atmosphere and the people in the group made it possible to work and enjoy it at the same time. I also appreciate, that I was allowed to follow my own ideas, which I take not for granted.

Further, I want to thank Christian Winkler for supporting me in my work. He gave me a lot of advice, be it creating appropriate presentations or how to perform accurate calculations. I think the outcome of our research during the last year provides a good basis for future projects within the topic of electronic couplings.

This thesis marks also the end of my student days. Therefore I want to thank especially my parents for many reasons. My father has inspired me since my young ages, excited my curiosity for discovering new things. My mother always supported me in any kind of problem, be it the search for a flat or organizing other things. Not to forget, the financial support through out all the years, which is something that I really appreciate.

Contents

1 Introduction and Motivation

The rapid development of new materials and the ever-growing interest in their respective properties are a big field of contemporary research. In former days, the estimation of material properties was more or less exclusively carried out by experiments. However, in the last decades a huge improvement in computational methods led to the possibility of analysing materials even before they are synthesized. This includes nearly every kind of property which can be estimated by using quantum mechanical models. Further, the application of such methodologies is not restricted to one kind of materials. For sure, different chemical environments require different models to describe them, but for almost every system a suitable approach is available. In this work, the materials of interest are organic semiconductors, which nowadays are found in quite many applications. These include organic field effect transistors (OFET's), organic light emitting diodes (OLED's) or even solar cells. All of them represent opto-electronic applications and, therefore, the question arises, how suitable a specific material is, for this purpose. That can be answered by studying the electronic properties of materials, particularly the capability to transport charge. Charge transport, constitutes the core topic of this thesis. Due to the importance of this property, a lot of research is dedicated to it. The selection of approaches reaches from quantum mechanic calculations up to stochastic methods. This work focusses on the former, which are also known as ab-initio calculations. Therefore, a short introduction into density functional theory (DFT) is given at the beginning of this work. The estimation of charge transport properties affords models beyond such calculations. That means results of the quantum mechanical treatment are plugged into different models to finally calculate the desired quantities. In general, there are two limiting processes for charge transport, namely band- and hopping transport. For the former, the electronic structure of a system determines mostly the behaviour of propagating charges. In the hopping regime quite different mechanisms are relevant. They can be described by a variety of models. However, many of those models have in common that they depend on electronic couplings. These electronic couplings are essential for an accurate estimation of charge transport properties. Therefore, the present thesis is dedicated to the estimation of such couplings. This includes the discussion and implementation of already existing approaches but also the development of new methodologies. The available approaches, discussed in this work, are the Electronic Splitting in Dimers (ESD) and the Fragment Orbital method. Those are representatives of so-called cluster-based methodologies, which estimate the electronic coupling by using clusters of molecules. Furthermore, a new approach inspired by the above-mentioned methods is developed, which is called Block Decomposition. For the sake of validation, a test set of different organic molecules is evaluated to benchmark features and functionality of the different methods. Beyond cluster approaches, the aim of this thesis is to provide accurate electronic couplings in molecular crystals. The use of cluster-based methodologies to approximate those couplings for the periodic case is often justified. Nevertheless, the call for an alternative approach led to a quite different idea. A tight-binding function as fundamental model is used to perform a fit to electronic structures of certain materials.

This methodology allows to reproduce the electronic band structure by an analytical function and, further, to extract electronic couplings. The derivation of an analytical function also provides the possibility to calculate the effective mass as ingredient for band transport, which is also shown within this work. Notably, a new methodology is just as good as its results. Therefore, two organic materials are studied to validate the suitability of this approach. Those materials are the quinacridone α-phase and pentacene. Moreover, the cluster-based approaches are used to benchmark all the obtained methodologies, including tight-binding fits, against each other.

2 Fundamentals

2.1 Electronic Structure

The present chapter gives a brief introduction to the basics of electronic structure theory. The starting point is the Schrödinger equation, where the focus lies on numerical approaches to solve it. Therefore, the commonly used concept of density functional theory (DFT) will be discussed. That includes a short explanation of the derivation based on the Kohn-Sham formalism. Furthermore, the application and theory of relevant exchange-energy functionals are shown. The use of atom-centred (localized) basis functions is also part of this chapter. The density functional theory part of this chapter is mainly based on the book by Richard M. Martin, Electronic Structure [1].

2.1.1 Many-Particle Systems

Computational physics nowadays represents a major part of research in materials. The aim of this field is to calculate microscopic properties on a quantum mechanic level for a specific system. That reaches from single atoms via molecules up to complex periodic structures. The starting point of nearly every quantum mechanic calculation is the Hamiltonian operator. For systems including more than one electron, a many-particle operator as stated in Eq. (2.1) is required. The first two parts represent the kinetic energy of the electrons and the nuclei. The mass of electrons is given by m_e, whereas $\hbar$ represents the reduced Planck's constant. The mass of nuclei is stated by m_a. The Coulomb interaction between nuclei and electrons is given by the third sum. The charge of the nuclei is given by the number Z_a times the elementary charge e. The value ϵ_0 represents the electric constant. It follows the electron-electron interaction and the Coulomb repulsion between the nuclei.

$$\hat{H} = -\sum_i \frac{\hbar^2}{2m_e}\nabla_i^2 - \sum_a \frac{\hbar^2}{2m_a}\nabla_a^2 - \sum_{i,a} \frac{Z_a e^2}{4\pi\epsilon_0|\mathbf{r_i}-\mathbf{r_a}|} + \sum_{i<j} \frac{Z_a e^2}{4\pi\epsilon_0|\mathbf{r_i}-\mathbf{r_j}|} + \sum_{a<b} \frac{Z_a Z_b e^2}{4\pi\epsilon_0|\mathbf{r_a}-\mathbf{r_b}|}$$

$$(2.1)$$

The Born-Oppenheimer approximation [2,3] can be used to decouple the electronic part from nuclear motion. A very simplified explanation for this would be that electrons move by orders of magnitude faster than nuclei, which justifies the decoupling. That

results in the electronic Hamiltonian as shown in Eq. (2.2), whereby atomic units were used to simplify the expression.

$$\hat{H}_{elec} = -\sum_i \frac{1}{2}\nabla_i^2 - \sum_{i,a} \frac{Z_a}{|\mathbf{r_i} - \mathbf{r_a}|} + \sum_{i<j} \frac{Z_a}{|\mathbf{r_i} - \mathbf{r_j}|} + \sum_{a<b} \frac{Z_a Z_b}{|\mathbf{r_a} - \mathbf{r_b}|} \tag{2.2}$$

The corresponding time-independent Schrödinger equation for the electronic part is stated in Eq. (2.3). The ground state of the system is given by the many-electron wave function $\Psi_0(\mathbf{r_1}...\mathbf{r_N})$, with the corresponding energy E_0. One of the main tasks and also one of the most challenging ones in computational physics is to solve this equation. The difficulty lies in the electron-electron interaction, which is not solvable analytically.

$$\hat{H}\,|\Psi_0\rangle = E_0\,|\Psi_0\rangle \tag{2.3}$$

Nevertheless, there are several approaches to tackle this problem. Most famous are the Hartree-Fock (HF) method and density functional theory (DFT). Since the DFT-method builds the foundation for later shown concepts, a short introduction of its main ingredients is provided in the next chapter.

2.1.2 Density Functional Theory (DFT)

In general, there are two different strategies to solve the electronic Schrödinger equation. The first one would be wave function based approaches, which can be related to the Hartree-Fock method. This strategy is often used, but unfortunately the computational costs are rather high for bigger systems. At this point, density functional theory becomes of great interest. Hohenberg and Kohn [4] stated two theorems which form the basis of the DFT formalism. As a first step, one starts with the electronic Hamiltonian from above, which is simplified by taking identifiers of letters for the single contributions. The corresponding equation is shown in Eq. (2.4), whereby the kinetic energy of the electrons is given by $\hat{T}_k$. The external potential arising from the positively charged nuclei is expressed by $\hat{V}_{ext}$ and the electron-electron interactions are given by $\hat{V}_{e-e}$. Another important expression is found in Eq. (2.5), which defines the electron density $n(\mathbf{r})$. The total number of electrons in the system is given by N. The electron density will be the point of interest for further considerations.

$$\hat{H} = \hat{T}_k + \hat{V}_{ext} + \hat{V}_{e-e} \tag{2.4}$$

$$n(\mathbf{r}) = N \int d\mathbf{r_1} \dots d\mathbf{r_N} \mathbf{\Psi_0}^*(\mathbf{r_1}...\mathbf{r_N})\mathbf{\Psi_0}(\mathbf{r_1}...\mathbf{r_N}) \tag{2.5}$$

$$E_{HK} = T_k[n] + E_{int}[n] + \int d\mathbf{r} V_{ext}(\mathbf{r})n(\mathbf{r}) + E_{II} \tag{2.6}$$

The main advantage of using the electron density is found in its respective dependencies. The density depends on just three variables instead of $3N$ for wave functions. The definitions from above can now be used to understand the theorems of Hohenberg

and Kohn. The first theorem states that for an interacting ensemble of particles in an external potential $\hat{V}_{ext}$, the potential is determined uniquely by the ground state electron density. The second theorem states, that an universal functional $E[n(\mathbf{r})]$ can be defined. For any external potential $\hat{V}_{ext}$, the minimum of this functional and therefore the corresponding electron density $n(\mathbf{r})$, which minimizes the energy, is the exact ground state density. The total energy can be expressed by splitting the Hamiltonian and using functionals as shown in Eq. (2.6). The contributions are kinetic energy, electron-electron interactions, external potential, and nuclei-nuclei interaction. For a more detailed description and the proof of those theorems see [1,4]. In other words, by finding the right density it is possible to calculate the ground state of the system. Those theorems are the basis for the functionality of density functional theory, but, unfortunately, the universal functional is not known yet. Therefore, people are trying to approximate the energy by finding appropriate expressions for the universal functional. A quite interesting approach to do so is the concept developed by Kohn and Sham [5]. Of course, one of the main advantages regarding DFT is the reduction of the dimension by using the density. Nevertheless, the Kohn-Sham (KS) formalism introduces single-electron functions ψ_i (so-called KS-orbitals) again to establish a systematic way to solve the Schrödinger equation in a self-consistent way. The main idea of the KS-formalism is to define an auxiliary system which can be solved more easily. It is assumed that the ground state of an interacting system can be solved by mapping the problem to a non-interacting system. The following derivation of the KS-formalism is taken from the book of Richard M. Martin, Electronic Structure [1]. First of all, definitions of several physical quantities in relation to KS-orbitals are presented. The electron density, shown in Eq. (2.7), is given by the sum over all occupied KS-orbitals.

$$n(\mathbf{r}) = \sum_i^N |\psi_i(\mathbf{r})|^2 \tag{2.7}$$

The kinetic energy can be calculated by applying the gradient to the orbitals and integrating over the whole space, which is stated in Eq. (2.8). This kinetic energy corresponds to non-interacting particles, which is the above-mentioned auxiliary system. The Coulomb interaction between particles in terms of energy is derived by Eq. (2.9). The division by two is required to avoid double counting.

$$T_k[n] = \frac{1}{2} \sum_{i=1} \int d^3r |\nabla\psi_i(\mathbf{r})|^2 \tag{2.8}$$

$$E_{Hartree}[n] = \frac{1}{2} \int d^3r d^3r' \frac{n(\mathbf{r})n(\mathbf{r}')}{|\mathbf{r} - \mathbf{r}'|} \tag{2.9}$$

With the definitions from above, it is possible to specify the total energy in the KS-formalism. The corresponding equation, describing the non-interacting reference system, is stated in Eq. (2.10).

$$E_{KS} = T_k[n] + \int d\mathbf{r} V_{ext}(\mathbf{r})n(\mathbf{r}) + E_{Hartree}[n] + E_{II} + E_{xc}[n] \tag{2.10}$$

The kinetic energy T_k presents the first term in this equation. The external potential V_{ext} must be multiplied by the electron density and integrated over space to obtain the corresponding potential energy arising from the interaction between nuclei and electrons. It follows the Hartree energy $E_{Hartree}$ as functional of the density, as shown in the definition in Eq. (2.9). The nuclei-nuclei interaction is represented by E_{II}, which is within the Born-Oppenheimer approximation just a constant. The last term is the so-called exchange-correlation energy E_{xc}, which also depends on the electron density. The exchange-correlation energy is used to express all quantum mechanical effects which are not included in the first three contributions. For example that would be exchange-energies and correlation phenomena. Furthermore, the error occurring from the non-interacting kinetic energy is also included here. Due to that, the main problem of this concept becomes evidently, namely the functional $E_{xc}[n]$ is unknown. As a consequence one has to approximate this contribution, whereby a great variety of different models is nowadays available. An overview of important exchange-correlation functionals and their respective approximations is given in Ch. 2.1.3. The definitions and expressions from above are now used to formulate a solvable problem, which is similar to the time-independent Schrödinger equation. Therefore, the so-called Kohn-Sham differential equation is stated in Eq. (2.11). The Kohn-Sham potential is shown in Eq. (2.12). The potential is calculated by taking the first derivative of the energy E_{KS} with respect to the electron density.

$$\left(-\frac{1}{2}\nabla^2 + V_{KS}(\mathbf{r}) \right) \psi_i(\mathbf{r}) = \epsilon_i \psi_i(\mathbf{r}) \tag{2.11}$$

$$V_{KS}(\mathbf{r}) = V_{ext}(\mathbf{r}) + V_{Hartree}(\mathbf{r}) + V_{xc}(\mathbf{r}) \tag{2.12}$$

In summary, it can be said, that to solve the electronic structure of any system by applying the KS-formalism one has to consider the following steps. First, an appropriate basis set is required to construct the KS-orbitals. How this can be realized and what possibilities are available is shown in Chap. 2.1.4. After that, the differential KS-equations have to be solved in a self-consistent way by minimizing the total energy E_{KS}.

2.1.3 Functionals

One of the main challenges in DFT is to approximate the exchange-correlation functional in an appropriate way for a given system. For example, one can consider isolated molecules on one side and periodic structures on the other side. It is obvious that the electron density for both systems will be quite different. For the former, the density will be localized whereby for the latter the density can be delocalized. Therefore, a common approximation, which accurately works for both systems is hard to find. Nevertheless, there are several approximations for the exchange-correlation energy which do their job in a quite satisfying way. This chapter gives a short overview of the most common functionals, starting with the local density approximation. It is followed by the generalized gradient approximation and finally hybrid functionals are discussed. For further details on functionals, the original works of their developers are recommended. The following

brief introduction into functionals is based on the book of Richard M. Martin [1], Electronic Structure. In general, the exchange-correlation part in the Kohn-Sham potential can be stated as shown in Eq. (2.13). I.e. it is the derivative of the exchange-correlation energy E_{xc} with respect to the electron density $n(\mathbf{r})$. Note that the case of different spin channels is not discussed in this overview due to the fact that it is not relevant for this work.

$$V_{xc}(\mathbf{r}) = \frac{\delta E_{xc}}{\delta n(\mathbf{r})} \tag{2.13}$$

- Local density approximation (LDA): The LDA approximation is based on the idea, that a delocalized density can be approximated by using a uniformly distributed electron density. This is motivated by a material which has quite freely moving electrons like a metal. Hence, the electron density of a homogenous electron gas and its exchange-correlation energy ϵ_{xc}^{hom} are used for approximating such systems. In order to justify the application of this functional, the electron density of the calculated system has to be delocalized. The definition of the exchange-correlation energy for the Kohn-Sham formalism is stated in Eq. (2.14).

$$E_{xc}^{LDA}[n] = \int d^3 n(\mathbf{r}) \epsilon_{xc}^{hom}(n(\mathbf{r})) \tag{2.14}$$

- Generalized gradient approximation (GGA): For systems with electron densities differing from an actual homogenous electron gas, other approximations have to be made. An example of such a model is the so-called generalized gradient approximation (GGA). The basic idea is to extend the electron density, in contrast to the LDA approximation, by also including the gradient of the density. Two very common examples of GGA functionals are PW91 [6] and PBE [7]. Both were invented by Perdew and his coworkers. The general expression for GGA exchange-correlation energies is given in Eq. (2.15).

$$E_{xc}^{GGA}[n] = \int d^3 n(\mathbf{r}) \epsilon_{xc}^{hom}(n(\mathbf{r}), |\boldsymbol{\nabla} n|, ...) \tag{2.15}$$

- Hybrid functionals: Another class of exchange-correlation approximations are so-called hybrid functionals. Those are "mixtures" of GGA functionals with Hartree-Fock exchange energy. In the present case, the advantage is the inclusion of non-local exchange, which originates from Hartree-Fock. The disadvantage would be the increase in computational effort since the Hartree-Fock exchange part has to be solved at every iteration additionally to the other KS-parts. Nevertheless, those functionals provide an accurate way to estimate the electronic structure of a wide variety of different materials. The selection of different hybrid functionals is almost infinite. An often used functional is the PBE0 [7], in which the authors suggested a combination of 1/4 Hartree-Fock exchange and 3/4 of PBE [8] exchange. The

correlation energy is entirely taken from the PBE functional. The corresponding mathematical description is given in Eq. (2.16).

$$E_{XC} = \frac{1}{4}E_x^{HF} + \frac{3}{4}E_x^{PBE} + E_c^{PBE} \tag{2.16}$$

2.1.4 Atom-Centred Basis Functions

In Chap. 2.1.2, the Kohn-Sham formalism was discussed, which uses so-called single electron functions $\{\psi_i\}$ to solve the electronic part of the Schrödinger equation. The $\{\psi_i\}$'s are typically constructed as linear combinations of so-called basis functions. There are two conceptually different types of such basis functions. One flavour of basis sets builds at plane waves. Such basis sets are often found in periodic calculations but can also be used in the cluster case. The second possibility is to use atom-centred (localized) basis functions. In this work, the former case is not discussed because all further calculations are performed with the latter approach. The following discussion is based on the work of Blum et al. [9], which is also the groundwork of the DFT-package called FHI-*aims*. This package was used throughout the entire thesis when systems had to be solved with DFT. The single electron wave functions of the KS-formalism can be expressed by linear combinations of localized basis functions. The corresponding expression is stated in Eq. (2.17). Furthermore, one can derive the Schrödinger equation in matrix notation by using these localized basis functions. The result is stated in Eq. (2.18), whereby the matrix entries of Hamiltonian and overlap are given in Eq. (2.19) and (2.20).

$$\psi_i(\mathbf{r}) = \sum_{i,j} c_i \phi_j(\mathbf{r} - \mathbf{r_i}) \tag{2.17}$$

$$\sum_j h_{ij} c_{jl} = \epsilon_l \sum_j s_{ij} c_{jl} \tag{2.18}$$

$$h_{ij} = \int d^3\mathbf{r} \, \langle \phi_i(\mathbf{r} - \mathbf{r_i}) | \hat{h}_{ks} | \phi_j(\mathbf{r} - \mathbf{r_i}) \rangle \tag{2.19}$$

$$s_{ij} = \int \langle \phi_i(\mathbf{r} - \mathbf{r_i}) | \phi_j(\mathbf{r} - \mathbf{r_j}) \rangle \tag{2.20}$$

The further procedure is analogous to the above-mentioned general solution of the KS-formalism. Therefore, the Schrödinger equation has to be solved in a self-consistent way. It is obvious that at every iteration step, the matrix entries of the Hamiltonian have to be integrated again. For larger systems, including a high number of basis functions, this becomes computational very expensive. Nevertheless, the big advantage of such localized basis functions is the opportunity to use the individual contributions of the formalism for further calculations. This is also the basis for all cluster-based approaches for obtaining electronic couplings as shown later in this work.

2.1.5 Periodic Systems

The present chapter provides a short introduction to the adaption of the DFT formalism to periodic structures. As mentioned above, for the periodic case one can also consider plane wave basis sets. Nevertheless, atom centred basis functions are used in this work. The mathematical expressions of this chapter are taken from the work of Blum et al. [9]. The adaption affords a new basis, which can describe the translational properties of a lattice structure. Following Bloch's-theorem [10,11], explained in Ch. 3.4, one can use a linear combination of atom-centred basis functions to create Bloch-type basis functions. These new basis functions $\chi_{i,\mathbf{k}}(\mathbf{r})$ are given in Eq. (2.21), whereby the ϕ_i's are the atom-centred basis functions from the previous chapter. The translation operator $\mathbf{T}(\mathbf{N})$ represents the shift to another unit cell according to the vector $\mathbf{N}$. The exponential factor is the corresponding phase factor for every unit cell. With the new basis, one can now evaluate the Hamiltonian matrix analogous to the procedure for the non-periodic case. The entries of the corresponding matrix are given by Eq. (2.22). The main difference compared to the non-periodic case is the k-dependence of the Hamiltonian and the phase factors. The former implies that the Schrödinger equation has to be solved at different k-points with the requirement of convergence. Furthermore, for every k-point, the corresponding Kohn-Sham orbitals can be estimated, which results in an electronic band structure.

$$\chi_{i,\mathbf{k}}(\mathbf{r}) = \sum_{\mathbf{N}} e^{i\mathbf{k}\mathbf{T}(\mathbf{N})} \phi_i(\mathbf{r} - \mathbf{R_{at}} - \mathbf{T}(\mathbf{N})) \tag{2.21}$$

$$h_{ij}(\mathbf{k}) = \langle \chi_{i,\mathbf{k}}(\mathbf{r}) | \hat{h}_{ks} | \chi_{j,\mathbf{k}}(\mathbf{r}) \rangle = \sum_{\mathbf{M},\mathbf{N}} e^{i\mathbf{k}(\mathbf{T}(\mathbf{N})-\mathbf{T}(\mathbf{M}))} \langle \phi_{i,\mathbf{M}} | \hat{h}_{ks} | \phi_{j,\mathbf{N}} \rangle \tag{2.22}$$

2.2 Electronic Couplings

The present chapter gives a brief introduction into the definition and explanation of electronic couplings. The field of application of such couplings will be explained in the discussion of charge transport in the next chapter. As a first step, one can state the most general definition of electronic coupling as shown in Eq. (2.23). The shape is in principle of a quantum mechanical matrix element. The indices A, B represent the localization site of single electron wave functions ψ_i. Note that at this point of view, every kind of wave function could be considered. However, this work deals with electronic couplings in molecular crystals and clusters of molecules and therefore single electron wave functions derived with DFT are used. Furthermore, the Hamiltonian has to be a single particle operator, e.g the KS-Hamiltonian, to be consistent with the type of wave function. The indices i, j identify the wave functions with its corresponding energy states. For example, in the picture of electronic states in a molecule, those indexes could refer to the HOMO (highest occupied molecular orbital) or to the HOMO-1.

$$\boxed{t_{AB}^{ij} = \langle \psi_i(\mathbf{r} - \mathbf{r_A}) | \hat{H} | \psi_j(\mathbf{r} - \mathbf{r_B}) \rangle} \tag{2.23}$$

To summarize, electronic couplings are in general Hamiltonian matrix elements. The wave functions can be of equal type and localized at the same site. The corresponding values are called on-site couplings or on-site energies. If they are of different type or/and localized at different sites one speaks of transfer integrals or electronic couplings. Notably, the t_{AB}'s represent values in units of energy. An alternative interpretation can be stated from hopping transport as explained in the next chapter. Many models within that regime of transport describe propagating charges by transfer rates. The electronic coupling is found in those models by its squared value. That leads to an interpretation of the coupling as the probability for charge to move from one site to another.

2.3 Charge Transport

A particularly relevant process for the applicability of materials in electronic devices is charge transport. In general, charge transport is the capability of a material to transport charge by applying an external electric field. The macroscopic observable is the electrical conductivity σ which is the inverse of the resistivity. Another important quantity is the electrical mobility μ, which represents the ability of charges to move in a material. Notably, the mobility is direct proportional to the conductivity. In order to characterize materials by its electrical properties, the estimation of those parameters is of great interest. The theoretical study of charge transport is tackled on a microscopic level since fundamentally different materials, e.g. inorganic and organic structures, will show deviating behaviour. In general, there are two limiting processes for charge transport, namely band- and hopping transport. The main difference between those processes is found in the localization of charge carriers. That means, if charge carriers are delocalized, one speaks of band transport. On the other hand, if the carriers are localized at lattice sites, the prevailing mechanism will be hopping transport. In this chapter, an introduction into the main concepts of both mechanisms is provided. For further details regarding charge transport in organic systems, the reviews of Coropceanu et al. [12] and Oberhofer et al. [13] are recommended.

2.3.1 Band Transport

For many systems, especially inorganic materials, the prevailing microscopic mechanism is band transport. Nevertheless, also for organic materials that process plays an important role, particularly at low temperatures. For that purpose, this chapter provides an introduction into the semi-classical description of band transport. The following section is based on the book by R. Gross and A. Marx, Festkörperphysik [14]. In Ch. 2.1, the time-independent Schrödinger equation for periodic systems has been discussed. The solution to this equation is an electronic band structure $E(\mathbf{k})$, which describes the energy of crystal electrons. However, the treatment of transport phenomena requires the inclusion of the time-dependence of the Schrödinger equation. As a consequence, the complexity of finding a solution heavily increases. Because of that, a semi-classical description of transport is used. For that purpose, external forces are treated classically, whereas the electronic band structure is calculated quantum mechanically without time-

dependence. The idea of the semi-classical model is to construct wave packages $\Psi_n(\mathbf{r}, t)$ for the electrons. Furthermore, those localized wave packages are linear superimpositions of de-localized Bloch waves $\Psi_{n,\mathbf{k}}(\mathbf{r})$ in an interval of $k \pm \frac{\Delta k}{2}$. The mathematical expression for such a wave package is presented in Eq. (2.24). The index n refers to the nth-band of the electronic band structure $E_n(\mathbf{k})$. The function $u_{\mathbf{k}}(\mathbf{r})$ is part of the Bloch wave, whereas $a(\mathbf{k})$ represents a k-depended coefficient. The wave package has a specified momentum and describes the movement of electrons in a particle model. Furthermore, the propagation speed of the wave package is given by the group velocity as stated in Eq. (2.25).

$$\Psi_n(\mathbf{r}, t) = \sum_{k-\frac{\Delta k}{2}}^{k+\frac{\Delta k}{2}} a(\mathbf{k}) u_{\mathbf{k}}(\mathbf{r}) e^{i\left(\mathbf{k}\mathbf{r} - \frac{E_n(\mathbf{k})}{\hbar}t\right)} \tag{2.24}$$

$$\mathbf{v}_n = \frac{1}{\hbar} \frac{\partial E_n(\mathbf{k})}{\partial \mathbf{k}} \tag{2.25}$$

The equations of motions can be derived by using Newton's second law. The first equation is already given by the group velocity as shown in Eq. (2.25). The second equation connects the external forces with the crystal momentum. The corresponding equation is stated in Eq. (2.26). The external electric field is represented by $E(\mathbf{r}, t)$, whereas a possible present magnetic field is given by $B(\mathbf{r}, t)$.

$$\hbar \frac{d\mathbf{k}}{dt} = -e \left[E(\mathbf{r}, t) + v_n(\mathbf{k}) \times B(\mathbf{r}, t) \right] \tag{2.26}$$

The derivative of the group velocity $v_n(\mathbf{k})$ with respect to the time t leads to an acceleration as stated in Eq. (2.27). The last term in this equation can be replaced by Eq. (2.26). That results in an expression for the acceleration of a particle analogously to Newton's second law. The corresponding equation is given in Eq. (2.28), where the external force is represented by F_j. The proportionality between acceleration and external force is given by the inverse effective mass tensor $[(m^*)^{-1}(\mathbf{k})]_{ij}$, as stated in Eq. (2.29).

$$\frac{dv_n(\mathbf{k})}{dt} = \frac{1}{\hbar} \frac{d}{dt} \left(\frac{\partial E_n(\mathbf{k})}{\partial \mathbf{k}} \right) = \frac{1}{\hbar} \sum_{j=1}^{3} \frac{\partial^2 E(\mathbf{k})}{\partial k_i \partial k_j} \frac{dk_j}{dt} \tag{2.27}$$

$$\frac{dv_n(\mathbf{k})}{dt} = \frac{1}{\hbar^2} \sum_{j=1}^{3} \frac{\partial^2 E_n(\mathbf{k})}{\partial k_i \partial k_j} F_j \tag{2.28}$$

$$[(m^*)^{-1}(\mathbf{k})]_{ij} = \frac{1}{\hbar^2} \frac{\partial^2 E_n(\mathbf{k})}{\partial k_i \partial k_j} \tag{2.29}$$

From that, one can see that the effective mass tensor represents an important ingredient for the description of band transport. The effective mass depends on the curvature of the electronic band structure $E_n(\mathbf{k})$. Therefore, a large dispersion of a band will lead

to a small effective mass, which at the same time indicates a larger acceleration. Another important parameter is the probability of occupancy. For electrons, which are fermions, the Fermi-Dirac statistic represents the distribution of occupied/unoccupied energy states. That means, states according to the electronic band structure $E_n(\mathbf{k})$ are filled by electrons up to the Fermi-energy. The remaining energy states above the Fermi-energy remain unoccupied. The knowledge about the occupancy is relevant, since transport requires charge carriers as well as empty states in the same band. That requirement allows that charge carriers can occupy empty states and are able to propagate through the structure. Nevertheless, there is also a chance for transport in fully occupied bands if excitations of electrons into other bands create empty states. The mathematical expression of the Fermi-Dirac distribution is presented in Eq. (2.30). The temperature is represented by T, whereas μ is the total chemical potential.

$$f[E_n(\mathbf{k}), T] = \frac{1}{e^{\frac{E_n(\mathbf{k}) - \mu}{k_B T}} + 1} \tag{2.30}$$

However, the semi-classical model from above does not include scattering processes at this stage. That would lead to a constant velocity of the particles if an external electric field is applied. Owing to that, scattering processes play a major role due to the fact that the conductivity is limited by them. Notably, in an exact periodic lattice, scattering does not occur. Nevertheless, in reality, structures include vacancies, dislocations and impurities, which lead to scattering. Furthermore, vibrations of the lattice, so-called phonons, scatter with electrons in the structure. Finally, there is also scattering between electrons, which are not included in the one-particle model from above. However, the former processes are the prevailing ones and therefore the latter are often neglected. Notably, the description of scattering events is often pursued employing perturbation theory. To summarize, band transport is a constant interplay between acceleration of electrons induced by an external field and deceleration by scattering events. A mathematical description of this process can be found in the Boltzmann transport equation (BTE). In general, the BTE describes changes in the probability of occupancy induced by an external field and scattering events. Therefore, the statistical behaviour apart from the equilibrium is studied. The Boltzmann equation, which is a differential equation of order 1, is presented in Eq. (2.31). It relates the time-dependence of the distribution function $f(\mathbf{r}, \mathbf{k}, t)$ to the following three ingredients: The spatial dependence of the distribution function f, which is included by calculating $\nabla_\mathbf{r} f$. The corresponding expression is also called diffusion term, due to occupation gradients in real space. The contributions from external fields, like an electric field $\mathbf{E}$ or a magnetic field $\mathbf{B}$, define the second term in Eq. (2.31). The transport limiting scattering events, as described above, are expressed by the last term.

$$\frac{\partial f(\mathbf{r}, \mathbf{k}, t)}{\partial t} = -\mathbf{v} \nabla_\mathbf{r} f - \frac{e}{\hbar}(\mathbf{E} + \mathbf{v} \times \mathbf{B}) \nabla_\mathbf{k} f + \left(\frac{\partial f(\mathbf{r}, \mathbf{k}, t)}{\partial t} \right)_{scattering} \tag{2.31}$$

The solution of the BTE is quite complex due to the scattering term within this equation. The scattering term transforms the differential equation into an integro-differential

equation which requires sophisticated methods to solve it. These often build of density matrices or Green's functions. Their description, goes beyond the scope of this introduction into band transport. To summarize, band transport can be treated by using a semi-classical model. That leads to a description of propagating charges in a particle picture, whereby scattering events have to be included with perturbation theory. Furthermore, charge transport can be treated in a statistical way, which can be described by the Boltzmann theory.

2.3.2 Hopping Transport

In comparison to band transport, hopping occurs if electrons are localized at individual sites. These sites can comprise molecules, parts of molecules or even clusters of them. Therefore, hopping describes the movement of electrons/holes by discrete jumps from one site to another. In order to describe such processes, different models have been developed. A rather old but very useful approach has been derived from the Marcus Theory [15,16], which was originally developed to explain rates in electron-transfer reactions. The basic concept of his theory is discussed in more detail in the next subchapter. Another model, which includes also the influence of thermal fluctuations on charge transport, would be the transient-localization model [17, 18]. Those models are just two representatives amongst many others, but most of them have in common that also in these methods the electronic coupling (see Ch. 2.2) between sites plays a decisive rule.

2.3.2.1 Marcus Theory

In general, Marcus theory [15, 16, 19, 20] deals with transfer rates for describing discrete jumps of electrons in a chemical system. For this purpose, one can consider electrons localized at an electron donor (initial state) and their respective possibility to jump from there to an electron acceptor (final state). The originally developed model described so-called outer electron transfers. Those are processes, which are characterized by charge transfer between a donor and an acceptor, assuming only small structural changes. Furthermore, the donor and acceptor are separated from each other. In contrast, inner electron transfer occurs if there is a chemical bridge between donor and acceptor. In fact, both flavours of transfer can be found in the basic equation of Marcus Theory [21] as stated in Eq. (2.32).

$$k_{ET} = \frac{2\pi}{\hbar} |t_{AB}|^2 \frac{1}{(4\pi k_B T \lambda)^{\frac{1}{2}}} exp \left(-\frac{(\lambda + \Delta G^0)^2}{4 k_B T \lambda} \right) \tag{2.32}$$

The calculation of the transfer rate k_{ET} requires three main parameters amongst other physical constants and the temperature T, which are described further below. To understand the functionality of this model, a schematic energy surface of an electron transfer process is presented in Fig. 2.1. The solid lines represent adiabatic energy surfaces, whereas the dashed lines are the corresponding diabatic ones. If the electronic coupling t_{AB} is weak, the transfer process will be diabatic. On the other hand, a stronger coupling implies that the transfer is adiabatic. The electronic coupling between
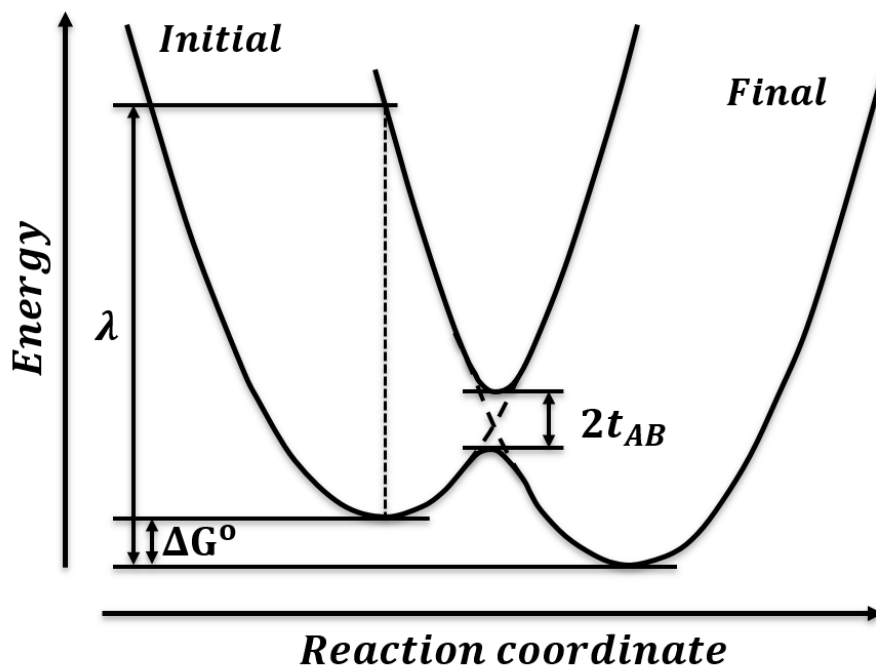
Fig. 2.1: Marcus Theory: A schematic energy surface for electron transfer. The graph shows the reorganization energy λ, the change in Gibbs free energy ΔG^o and the electronic coupling t_{AB}. The initial state is presented on the left side, whereas the final state is on the right side. The vertical axis represents the energy. The horizontal axis is the reaction coordinate of electron transfer.

molecules/fragments is explained in Ch. 2.2. Furthermore, the initial state with charge localized on the electron donor, is represented by the situation on the left side in Fig. 2.1. If charge is transferred adiabatically to the electron acceptor, the system will stay on the lower adiabatic curve. The final state, representing charge localized on the electron acceptor, is found at the right valley of the potential energy surface. From that, one can calculate the difference in free energy between the initial and final state. That change in Gibbs free energy ΔG^o is another important parameter for Marcus theory. Finally, structural changes induced by the transfer process are included in the reorganization energy λ. This energy takes inner- and outer sphere transfer processes into account. In general, it gives value to the energy needed to reorganize the structure by moving from the initial to the final state. The sum of reorganization energy and the difference in Gibbs free energy can be interpreted as the activation energy for the transfer process.

The relation between transfer rates and hopping mobilities is given by a direct proportionality $\mu \propto k_{ET}$. For further details on this topic, the work of Oberhofer and Blumberger [22] is recommended. A detailed description of Marcus theory and other hopping models can be found in Atkins' book of Physical Chemistry [23].

3 Calculating the Electronic Coupling: Established Techniques and New Approaches

The present chapter constitutes the main part of this thesis. It includes the description, theory, and implementation of different approaches to estimate electronic couplings. First of all, one can distinguish between cluster-based methodologies and approaches based on periodic calculations. For the former, there is a selection of established methods. They include the Electronic Splitting in Dimers [24] (ESD) method, Block Diagonalization [25, 26], Generalized Mulliken-Hush theory [27–29], the Fragment Orbital [30] (FO-DFT) approach and Constrained Density Functional Theory [31, 32] (CDFT), amongst others. In this work, the Electronic Splitting in Dimers method and the Fragment Orbital approach will be discussed. For the latter, which represents a more sophisticated method, an implementation as a post-processing tool is realized. Furthermore, different considerations lead to the development of a new methodology, called Block Decomposition. The corresponding theory and implementation of this approach is also part of this chapter. The above-mentioned methods are based on extracting electronic couplings from cluster calculations. For the sake of including the chemical environment of periodic structures, an alternative approach is found in tight-binding fits. The idea and theory behind that method constitutes the fourth part of this chapter.

3.1 Electronic Splitting in Dimers

The Electronic Splitting in Dimers [24, 33, 34] (ESD) method is one of the simplest approaches to estimate electronic couplings. The system considered in this approach is a dimer. Furthermore, that dimer is assumed to be symmetric and it can be divided into two identical fragments A and B. An illustrative picture of such a system is shown in Fig. 3.1. As a next step, the concept behind this approach is discussed: The aim is to calculate the electronic coupling between the two fragments building the dimer. For example, one can consider charge q localized at fragment A, which represents the initial state $\mathbf{A^q B}$. Then, there is a probability for this charge to move to the second fragment B by some kind of transport process. The configuration with charge localized at fragment B constitutes the final state $\mathbf{AB^q}$. The corresponding probability for such a process can be found in the electronic coupling between the two fragments.

For a further investigation and derivation of the splitting method, a short discussion of adiabatic- and diabatic states is necessary. The dimer system from above also here serves as an object of interest. First of all, the diabatic basis will be discussed. Therefore, one can derive a potential energy surface for both molecules. In the present case, just one state (E_A, E_B) for each fragment is considered. For example, the HOMO states of the individual molecules. These states are treated in the so-called diabatic basis. The illustration in Fig. 3.2 shows those separated energy surfaces as dotted lines. The electron transfer coordinate represents the nuclear coordinate of the system. Both lines indicate a crossing, which implies a vanishing coupling in the corresponding Hamiltonian
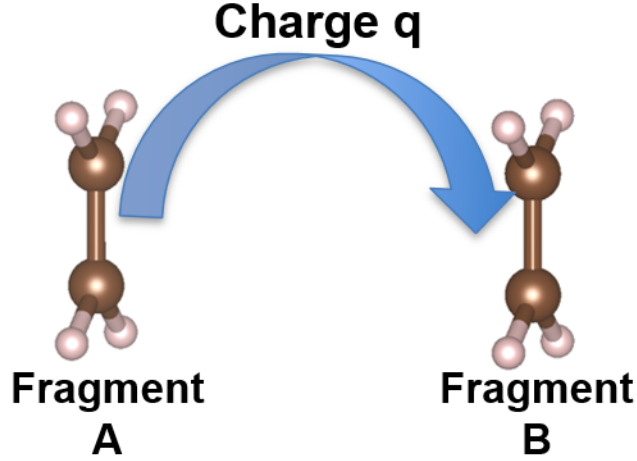
Fig. 3.1: Schematic illustration of charge transport in a dimer. First, charge is localized at fragment A, which represents the initial state. After transfer through the spatial splitting, charge is localized at fragment B, presenting the final state.

matrix for the diabatic basis as stated in Eq. (3.1).

$$\begin{pmatrix} E_A & 0 \\ 0 & E_B \end{pmatrix} \tag{3.1}$$

The diabatic system describes two individual molecules, whereby the coupling between the representative states is zero. However, for characterizing the combined system, the interaction between those states is relevant. An illustrative way to add the interaction would be to treat it like a perturbation of the separated system. Therefore, a new quantity t_{AB}, representing the interaction/coupling, is added to the Hamiltonian (see Eq. (3.2)).

$$\begin{pmatrix} E_A & 0 \\ 0 & E_B \end{pmatrix} + \begin{pmatrix} 0 & t_{AB} \\ t_{AB} & 0 \end{pmatrix} \rightarrow \begin{pmatrix} E_A & t_{AB} \\ t_{AB} & E_B \end{pmatrix} \tag{3.2}$$

The new Hamiltonian matrix, including the interaction, can be solved. This results in two eigenstates $E_{+,-}$. Solving the obtained eigenvalue problem, i.e. diagonalizing the matrix, corresponds to a transformation into an adiabatic basis. The new states are given by the solid lines in Fig. 3.2. It appears that the two states avoid a crossing, whereby they split by a certain amount of energy. Furthermore, one can take the difference between the adiabatic states, which is shown in Eq. (3.4). That means the splitting ΔE_{+-} is given by the difference of the energies E_A, E_B and the coupling t_{AB}.

$$\begin{pmatrix} E_A & t_{AB} \\ t_{AB} & E_B \end{pmatrix} \rightarrow E_{+,-} = \frac{E_A + E_B}{2} \pm \frac{1}{2}\sqrt{(E_A - E_B)^2 - (2t_{AB})^2} \tag{3.3}$$

$$\Delta E_{+-} = E_+ - E_- = \sqrt{(E_A - E_B)^2 - (t_{AB})^2} \tag{3.4}$$

15
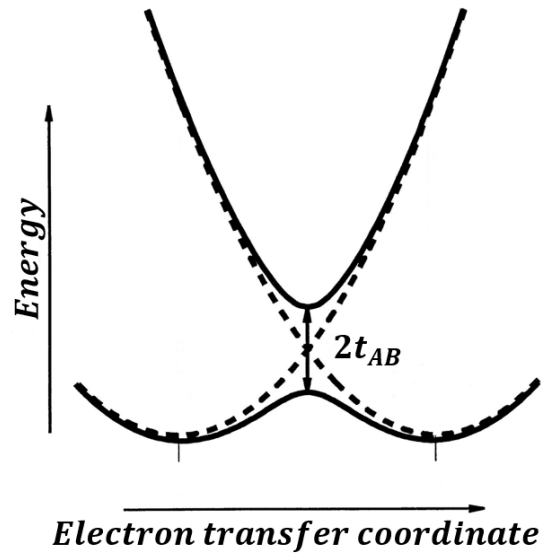
Fig. 3.2: Schematic potential energy surface of the symmetric ethylene dimer. The dotted lines represent diabatic states of the single molecules. The solid lines represent the corresponding adiabatic states of the dimer. Furthermore, the initial state considering charge on fragment A is indicated by $A^q B$, whereas the final state is given by AB^q. The transition state is given by the crossing of the diabatic lines. At this point, the adiabatic states split by two times the electronic coupling t_{AB}.

The diabatic quantities $E_{A,B}$ represent so-called on-site energies. They correspond to the energy of localized electrons on the molecules. The assumption from the beginning, namely the symmetry of the dimer, becomes relevant now. Due to the fact that both molecules experience the same symmetric environment, the on-site energies are equal. That results in a simple relation between coupling and adiabatic energies expressed by Eq. (3.5). From that, one can derive the Electronic Splitting in Dimers method. The idea is to use the energy splitting at the transition point (see Fig. 3.2), i.e. the point where the diabatic states cross. That means, at the transition point the splitting is assumed to be two times the electronic coupling t_{AB}. This assumption is just valid if the geometries at the transition point are used to calculate the adiabatic energies E_+ and E_-. However, it turned out that the adiabatic energies obtained by using a neutral dimer are a good approximation [12]. Therefore, the electronic coupling t_{AB} of symmetric dimers can be estimated by taking half of the difference ΔE_{+-} of adiabatic energies.

$$t_{AB} = \frac{E_+ - E_-}{2} = \frac{\Delta E_{+-}}{2} \tag{3.5}$$

For a real application of the ESD method, one can rewrite Eq. (3.5) by identifying A and B with actual orbital energies of the dimer. For example, the estimation of hole/electron couplings employs the following procedure. The electronic coupling, describing the electron case, is calculated by assuming E_+ and E_- are the LUMO/LUMO-1 energies. For

hole couplings, one would have to use the HOMO and HOMO-1 energies of the corresponding DFT-calculation on the dimer. The final result for the ESD-method is then given in Eq. (3.6).

$$t_{hole[electron]} = \frac{E_{HOMO-1[LUMO]} - E_{HOMO[LUMO+1]}}{2} \tag{3.6}$$

To summarize, the Electronic Splitting in Dimers method is a fast approach, but with the requirement of symmetry. If the precondition of symmetry is not given, the on-site energies are no longer equal and then Eq. (3.6) cannot be used to estimate the coupling. The symmetry of systems indicates a big issue regarding the estimation of electronic couplings. For that purpose, the next chapter discusses the effects of polarization. i.e. symmetry breaking on dimers.

3.1.1 Polarization effects

Previous work on polarization effects regarding electronic couplings and other quantities of cluster systems was undertaken by Valeev et al. [35]. The research on this topic highlighted the importance of on-site energies which should be included by estimating couplings. The most relevant result that sums up the main issues with symmetry, on-site energies, and couplings is illustrated in Fig. 3.3. The underlying system of the discussion is an ethylene dimer. The first case, given on the left side of the illustration, shows a face-to-face configuration. Therefore, the system is symmetric and the on-site energies are equal. That means the electronic coupling t_{AB} can be calculated by taking the half of the splitting ΔE_{+-}. The latter is defined by the difference in orbital energies, as discussed in the previous chapter. The second case, stated at the right side shows a face-to-edge configuration, in which the system has not inversion symmetry. The rotation of one molecule relative to the second one needs a detailed description of the influenced quantities. The electronic splitting ΔE_{+-} remains almost constant for the different configurations. The electronic coupling t_{AB} starts equal to the splitting, whereas by entering the non-symmetric face-to-edge configuration it vanishes. That indicates that the energy splitting does not entirely arise from the electronic coupling at non-symmetric configurations. Furthermore, the explanation of this can be found in Eq. (3.4), which shows the mathematical relation between splitting ΔE_{+-}, on-site energies $E_{A,B}$ and electronic coupling t_{AB}. The on-site energies describe the energy originating from localized electrons on the single molecules. In the symmetric case, as already mentioned in the previous chapter, the on-site terms are equal. The rotation of one molecule causes polarization of the system and induces a shift in on-site energies. Therefore, the corresponding energy splitting at the face-to-edge configuration is entirely caused by the difference in the on-site energies associated with the two molecules forming the dimer. It is not caused by the electronic coupling. At intermediate configurations the mathematical relation, presented in Eq. (3.4), gives the contributions to the energy splitting. At this point, the collapse of the ESD method becomes obvious. That means by inconsiderably taking half of the splitting at every configuration, one would overestimate the electronic coupling. In the next chapters, two different methodologies are discussed, which allow the estimation of electronic couplings in non-symmetric cluster systems.
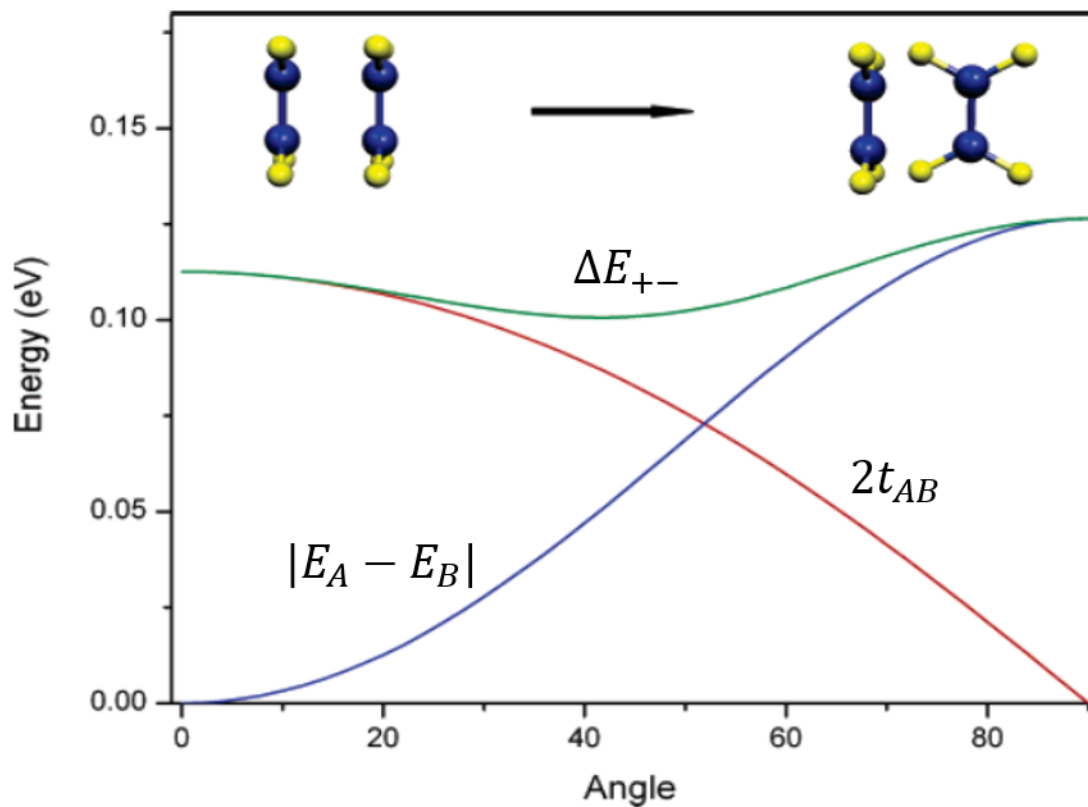
Fig. 3.3: Polarization effects due to symmetry breaking by the rotation of one ethylene molecule relative to the other. The left side shows the face-to-face configuration, whereas the right side illustrates the non-symmetric face-to-edge system. The green line represents the energy splitting ΔE_{+-}. The blue line shows the difference in on-site energies and the red line the electronic coupling t_{AB}. Adapted with permission from Valeev et al. [35]. Copyright (2019) American Chemical Society.

3.2 Fragment Orbital

The Fragment Orbital [36] approach, based on density functional theory, is one of the most commonly used methodologies for estimating electronic couplings. That approach includes also the estimation of couplings at non-symmetric configurations by taking the shift in on-site energies into account. In the next subchapter, the theory of Fragment Orbital DFT based on recent research [35] is discussed. To date, a certain number of implementations of this approach are available. However, an own implementation was customized for experimenting with different ideas and as foundation for developing a new theory.

3.2.1 Theory

The Fragment Orbital approach is based on the idea of using molecular orbitals of the single fragments to describe the final dimer system. That means, one orbital from each fragment contributes to the description of the combined system. The purpose is not to calculate the corresponding solution of this theoretical two state system but to extract the coupling between the states of the combined system. For example, the HOMOs of the isolated fragments can be used to calculate the coupling between HOMO and HOMO-1 of the combined system. That corresponds to the estimation of effective hole couplings. For the calculation of electron couplings, the LUMOs of the isolated fragments have to be used. Therefore, the starting point is a dimer, whereby it can consist of two equal or different molecules. The main advantage of this approach is, that it is not restricted to systems with inversion centres. For further progress, the dimer system is decomposed into its fragments, namely molecule A and B. As a first step, the electronic structure of both fragments has to be evaluated separately. This means that the time-independent Schrödinger equation has to be solved. This is realized here by using density functional theory (DFT) with an atom-centred basis. As a result, one gets eigenstates, eigenvalues, matrices and many more quantities. The eigenstates represent single electron wave functions as already discussed in Ch. 2.1. Therefore, for both molecules, a set of single electron wave functions is available. For fragment A, those functions are represented by the set $\{\psi_i(r - R_A)\}$. For fragment B, the set is given by the functions $\{\psi_j(r - R_B)\}$. For the theoretical two state system, the single electron wave functions from above are used to construct a matrix equation (Eq. (3.7)) for the combined (dimer) system. The corresponding matrices are given in Eq. (3.8). The entries of the Hamiltonian- and overlap matrix are derived by using all combinations of the two states as presented in Eq. (3.9), (3.10) and (3.11). The nature of Hamiltonian will be discussed in the next section. Nevertheless, the on-site energies are given by e_i and the electronic couplings are expressed by t_{ij}. The issue at this point is the non-orthogonality of the two different sets of single electron wave functions $\{\psi_i(r - R_A)\}, \{\psi_i(r - R_B)\}$.

$$\mathbf{HC} - E\mathbf{SC} = \mathbf{0} \tag{3.7}$$

$$\mathbf{H} = \begin{pmatrix} e_A & t_{AB} \\ t_{AB} & e_B \end{pmatrix}, \ \mathbf{S} = \begin{pmatrix} 1 & S_{AB} \\ S_{AB} & 1 \end{pmatrix} \tag{3.8}$$

$$e_i = \langle \psi_i(r - R_i)|\hat{H}|\psi_i(r - R_i)\rangle \, ; \; i \in \{A, B\} \tag{3.9}$$

$$t_{ij} = \langle \psi_i(r - R_i)|\hat{H}|\psi_j(r - R_j)\rangle \, ; \; i, j \in \{A, B\} \tag{3.10}$$

$$S_{ij} = \langle \psi_i(r - R_i)|\psi_j(r - R_j)\rangle \, ; \; i, j \in \{A, B\} \tag{3.11}$$

For a physically appropriate description of the combined system, a transformation to an orthogonal basis is essential. For that purpose, a Löwdin symmetry transformation is used. For a detailed explanation and the application of this procedure, the original work of P. Löwdin [37] is recommended. The basic idea of the orthogonalization is a linear transformation of the eigenvectors $\mathbf{C'} = \mathbf{S}^{-\frac{1}{2}}\mathbf{C}$, whereby $\mathbf{S}$ is the overlap matrix and $\mathbf{C}$ the coefficient matrix. As a result the generalized eigenvalue problem from Eq. (3.7) is transformed into a normal eigendecomposition (see Eq. (3.12)).

$$\mathbf{H^{eff}}\mathbf{C'} = E\mathbf{C'} \tag{3.12}$$

$$\mathbf{H^{eff}} = \begin{pmatrix} e_A^{eff} & t_{AB}^{eff} \\ t_{AB}^{eff} & e_B^{eff} \end{pmatrix} \tag{3.13}$$

$$e_{A,B}^{eff} = \frac{1}{2}\frac{(e_A + e_B) - 2t_{AB}S_{AB} \pm (e_A - e_B)\sqrt{1 - S_{AB}^2}}{1 - S_{AB}^2} \tag{3.14}$$

$$t_{AB}^{eff} = \frac{t_{AB} - \frac{1}{2}(e_A + e_B)S_{AB}}{1 - S_{AB}^2} \tag{3.15}$$

The entries of the new Hamiltonian matrix H^{eff} are given in Eq. (3.14) and (3.15). That includes the electronic coupling t_{AB}^{eff} and the on-site energies $e_{A,B}^{eff}$, which are now in an orthogonal basis. The expression given by Eq. (3.15) presents also the result of the Fragment Orbital approach, namely the estimation of the effective coupling t_{AB}^{eff}. Furthermore, one can solve the matrix equation to obtain the corresponding energies $\epsilon_{1,2}$. The expression for those eigenvalues are given in Eq. (3.16).

$$\epsilon_{1,2} = \frac{e_A^{eff} + e_B^{eff}}{2} \pm \frac{1}{2}\sqrt{(e_A^{eff} - e_B^{eff})^2 - (2t_{AB}^{eff})^2} \tag{3.16}$$

The solution of the Hamiltonian matrix includes two eigenstates, a bonding and an anti-bonding one. An illustration of corresponding orbitals, which illustrate the Fragment Orbital method in an schematic way, can be found in Fig. 3.4. Notably, the derived eigenvalues $\epsilon_{1,2}$ should be similar to the orbital energies, e.g. HOMO and HOMO-1 energies, obtained by the DFT-calculation of the combined system. To summarize the Fragment Orbital approach, the isolated fragments have to be calculated first. Taking two of the derived single electron wave functions, e.g. the HOMOs, of each molecule allow to describe the combined system in a two state system. The solution of this system gives the HOMO and HOMO-1 of the dimer system and the electronic coupling between those states is extracted.
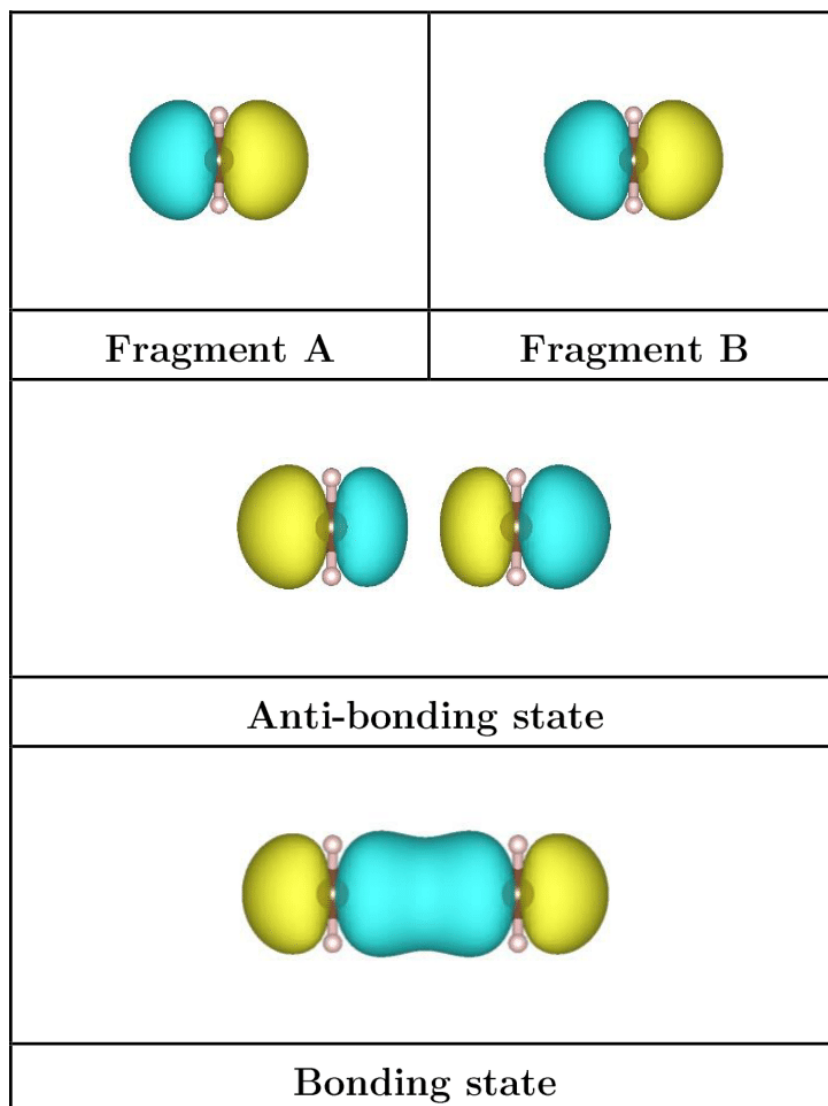
Fig. 3.4: The Fragment Orbital method explained by a schematic representation. First, the single electron wave functions are used as a new basis, i.e. one orbital for each molecule. Those orbitals are localized at their respective molecules. Solving the corresponding eigenvalue problem results in two states, describing the electronic structure of the dimer. The energetic higher lying anti-bonding state and the energetic more favourable bonding state.

3.2.2 Implementation

In this section, the implementation of the Fragment Orbital approach is discussed. First of all, a suitable DFT-package to solve the Schrödinger equation is required. Owing to the fact that the Fragment Orbital method involves the calculation of cluster structures, the focus lies on codes which are based on atom-centred basis functions. Therefore the FHI-*aims* [9] package was chosen since this code fulfils all requirements for the implementation. The present implementation is realized as a post-processing tool. As a first step of the implementation, one has to identify which quantities are of interest to realize the Fragment Orbital method. The most important ingredients are the fragment orbitals, i.e. single electron wave functions of the individual DFT-calculations. Those are determined by vectors **c**, which are the LCAO-coefficients for the atom-centred basis functions. For the sake of consistency within this chapter, molecular orbitals are synonymous to single electron wave functions. The latter are given in Eq. (3.17), whereby the coefficients $c_{i,l}$ correspond to the lth-eigenvector of the time-independent Schrödinger equation. The ϕ_i's are the atom-centred basis functions. The sum over i runs over the included basis functions N. Other important quantities are the Hamiltonian- and the overlap matrix in the atom-centred basis, which are needed for different purposes. Both of them are directly accessible in the FHI-*aims* package. Therefore, one gets all these quantities for fragment A, fragment B and for the combined (dimer) system as listed in Tab. 3.1.

Tab. 3.1: List of quantities derived from DFT-calculations of fragments and combined system. Dimension... represents the number of used basis functions for the corresponding calculation.

Quantity	Fragment A	Fragment B	Combined System
Dimension	N	M	$N + M$
Hamiltonian matrix	H_A	H_B	H_C
Overlap matrix	S_A	S_B	S_C
Eigenvalues	ϵ_A	ϵ_B	ϵ_C
Eigenvectors	c_l^A	c_l^B	c_l^C

As a next step, all quantities derived in the theory part have to be evaluated. The first ones are the on-site energies $e_{A,B}$ and the coupling t_{AB} in the non-orthogonal basis. For that purpose, one starts with plugging the definition of single electron wave functions (see Eq. (3.17)) of the isolated molecules (A,B) into the mathematical expression for the electronic coupling (Eq. (3.18)). That equation can be rearranged into Eq. (3.19).

$$\left| \psi_l^{A,B} \right\rangle = \sum_{i=1}^{N} c_{i,l}^{A,B} \phi_i^{A,B}(r - r_i) \tag{3.17}$$

$$t_{AB} = \langle \psi_n^A | \hat{h}_{ks} | \psi_m^B \rangle = \left\langle \sum_{i=1}^{N} c_{i,n}^A \phi_i^A (r - r_i) \left| \hat{h}_{ks} \right| \sum_{j=1}^{M} c_{j,m}^B \phi_j^B (r - r_j) \right\rangle \tag{3.18}$$

$$t_{AB} = \sum_{i=1}^{N} \sum_{j=1}^{M} (c_{i,n}^A)^\dagger c_{j,m}^B \left\langle \phi_i^A (r - r_i) \left| \hat{h}_{ks} \right| \phi_j^B (r - r_j) \right\rangle \tag{3.19}$$

$$h_{ij} = \left\langle \phi_i^A (r - r_i) \left| \hat{h}_{ks} \right| \phi_j^B (r - r_j) \right\rangle \tag{3.20}$$

From that, one can see that the matrix entries h_{ij} are given by atom-centred basis functions $\phi_i(r)$. The corresponding mathematical expression of those values is stated in Eq. (3.20). The single particle operator $\hat{h}_{ks}$ is the KS-Hamiltonian of the combined system. However, the sum over i and j in Eq. (3.19) includes basis functions localized at fragment A interacting with functions localized at fragment B. Those values are not included in the isolated fragment calculations. An approximation for the h_{ij} values can be found in the combined system solution. The Hamiltonian matrix of the combined system contains all possible combinations of basis functions (see Eq. (3.20)), i.e. also between basis functions of fragment A and B. Nevertheless, the electronic coupling t_{AB} has to be evaluated in the non-orthogonal basis. Therefore, the single electron wave functions of the isolated fragments are used in combination with the matrix elements h_{ij} of the combined system solution. The mathematical expression for the electronic coupling can be simplified by using matrix notation. That is possible due to the fact that the Hamiltonian matrix of the combined system $\mathbf{H_C}$ can be decomposed into blocks. A detailed description about how this works can be found in Ch. 3.3. The result is a matrix consisting of four blocks as shown in Eq (3.21). The first block $\mathbf{H}_\alpha$ includes all matrix entries h_{ij} of basis functions localized at fragment A, i.e. interactions just on A. Analogously is the case for fragment B, where $\mathbf{H}_\beta$ can be identified with the corresponding values. The remaining two blocks $\mathbf{H}_{\alpha\beta}$ and $\mathbf{H}_{\beta\alpha}$ contain the matrix elements between the two fragments. The electronic coupling t_{AB} in the non-orthogonal basis is now expressed by using the $\mathbf{H}_{\alpha\beta}$ block. The coefficient vectors $\mathbf{c_n^{A,B}}$ of the isolated fragments are multiplied from left and right to the block matrix which results in Eq. (3.22). The index n represents the corresponding state, e.g. for the hole coupling the HOMOs of the fragments. Note that the overlap S_{AB} is calculated analogous to the electronic coupling.

$$\mathbf{H_C} = \left(\begin{array}{c|c} \mathbf{H}_\alpha & \mathbf{H}_{\alpha\beta} \\ \hline \mathbf{H}_{\beta\alpha} & \mathbf{H}_\beta \end{array} \right) \tag{3.21}$$

$$t_{AB} = (\mathbf{c_n^A})^\dagger \mathbf{H}_{\alpha\beta} \mathbf{c_m^B} \tag{3.22}$$

For the on-site energies, one can derive the mathematical expression given in Eq. (3.23). The procedure for deriving this equation is analogous to the above-discussed electronic coupling. However, for the case of on-site energies, the single electron wave functions $\psi_l^{A,B}$ are localized at the same site, either fragment A or B. Notably, the matrix entries h_{ij} including the atom-centred basis functions $\phi_i^{A,B}$ are equally defined as shown for the

electronic coupling (see Eq. (3.20)). Those values are of great interest for the estimation of on-site energies. In principle, the h_{ij} values can be obtained by the isolated fragment calculations. However, if those values are used for the estimation of on-site energies, polarization effects will not be included. Therefore, the combined system solution can be used to include those effects. That means, the block matrices $\mathbf{H}_\alpha$ and $\mathbf{H}_\beta$ of the combined Hamiltonian matrix $\mathbf{H_C}$ are used to approximate the on-site energies in the non-orthogonal basis. For example, the block matrix $\mathbf{H}_\alpha$ includes the values h_{ij} of basis functions localized at fragment A, which are influenced by the presence of fragment B. As a result, the on-site energies of the fragments are calculated by using the coefficient vectors $\mathbf{c_n^{A,B}}$ of single electron wave functions of the isolated calculations and the h_{ij} values of the combined system. The final expression for on-site energies in the non-orthogonal basis is shown in Eq. (3.24).

$$e_{A,B} = \sum_{i=1}^{N} \sum_{j=1}^{N} (c_{i,n}^{A,B})^\dagger c_{j,m}^{A,B} \left\langle \phi_i^{A,B}(r - r_i) \middle| \hat{h}_{ks} \middle| \phi_j^{A,B}(r - r_j) \right\rangle \tag{3.23}$$

$$e_{A,B} = (\mathbf{c_n^{A,B}})^\dagger \mathbf{H}_{\alpha,\beta} \mathbf{c_m^{A,B}} \tag{3.24}$$

Finally, all necessary inputs for the Fragment Orbital approach are calculated. The last step is to use the Eqs. (3.14) and (3.15) to perform the Löwdin symmetry transformation. As a result, the effective on-site energies $e_{A,B}^{eff}$ and the electronic coupling t_{AB}^{eff} are estimated.

3.3 Block Decomposition

In the present chapter, the development of a new approach called Block Decomposition (BD) is discussed. First of all, this methodology belongs to the category of cluster-based approaches. That means, the electronic coupling between fragments in a cluster is calculated. As a representative example for such a system, an ethylene dimer is chosen. The structure of the dimer is presented in Fig. 3.5. It can be divided into two fragments A, B. The development of Block Decomposition is inspired by the Fragment Orbital approach and the Block Diagonalization [25] method. The latter allows to calculate electronic couplings without the individual fragment calculations. A short explanation of this methods follows next. First of all, the combined system (dimer) is solved with DFT. As a result, the Hamiltonian matrix is accessible. This matrix is decomposed into blocks, whereby the blocks are identified by their corresponding fragments. Then the blocks are diagonalized individually, which results in a set of eigenvectors for each block. Those eigenvectors have to be transformed into a common basis of the individual eigenvectors. Finally, the electronic coupling between the fragments can be extracted. However, the transformation into a common basis is not unique. That means, there is a degree of freedom for determining the electronic coupling. At this stage, the idea to search for an alternative way to extract the electronic coupling arose. As a first step, different functional requirements to the new approach were considered, which are listed below.

- The methodology should use results from density functional theory (DFT) to estimate the electronic coupling as a post-processing step.

- The estimation of the electronic coupling should be possible without the calculation of the individual fragments.

- Their should be no restrictions regarding the structure of the cluster, particularly that the system can have arbitrary symmetry.

- The accuracy of the estimation should match up with the Fragment Orbital and other cluster-based approaches.

Taking all of those points into account, a theoretical concept is developed. The starting point is the block decomposition similar to the Block Diagonalization method, which explains the choice of the new approach's name. From that, different theoretical steps are undertaken to find an alternative way for estimating the electronic coupling. The theory is explained in the next chapter, while the implementation can be found in Ch. 3.3.2.
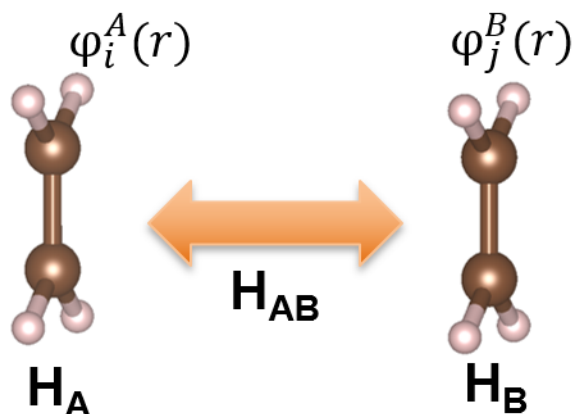
Fig. 3.5: Cluster (dimer) system consisting of two ethylene molecules A and B, representing the fragments. The basis functions localized on fragment A are indicated by ϕ_i^A. For localization on fragment B, the functions ϕ_j^B are present. $\mathbf{H_A}$, $\mathbf{H_B}$ and $\mathbf{H_{AB}}$ are representing block matrices of the entire Hamiltonian matrix in the atom-centred basis.

3.3.1 Theory

This section deals with the theoretical concept of the Block Decomposition (BD) method. Due to the complexity of the following mathematical derivation, an overview of the main concept is presented first. In this outline, one can see that the concept can be divided into six parts. All of those parts are explained in detail in the corresponding sub-chapters further below. The fundamental basis of the BD approach is the DFT-calculation (see Ch. 3.3.1.1) of the combined system. As a result of this calculation, the Hamiltonian- and overlap matrix are obtained. Those matrices are then decomposed into blocks (see Ch. 3.3.1.2). The decomposition allows to identify matrix entries of the Hamiltonian/overlap matrix with the individual fragments of the cluster. Furthermore, the matrices in block shape are used to rewrite the Schrödinger equation. This equation is evaluated for two eigenvectors/eigenvalues of the DFT-calculation (see Ch. 3.3.1.3). That results in different scalar values, which again can be identified with the individual fragments of the cluster. So far, the formalism includes a separation of the Schrödinger equation, which is indeed just an alternative representation of this equation. Nevertheless, the scalar values are used to construct a theoretical two-state system (see Ch. 3.3.1.4). That means, one equation for each eigenvector from above is defined. The theoretical construct is still correct and describes the relation between all energy parts. As a next step, both equations are combined by summing them. That results in the final theoretical two-state system. This construction is used to estimate the on-site energies (see Ch. 3.3.1.5) of the individual fragments. The obtained on-site energies are used to calculate the electronic coupling between the fragments (see Ch. 3.3.1.6), i.e. the electronic coupling between two orbitals of the combined system is calculated. The estimation is based on the energy splitting between those two orbitals. For example, the

estimation of hole couplings is referred to the coupling between HOMO and HOMO-1 of the combined system.

3.3.1.1 DFT-Calculation of the Combined System

The first step is the DFT-calculation of the cluster system. That means, for example, the above-mentioned ethylene dimer is solved by DFT using an atom-centred basis. In general, by performing that calculation, the time-independent Schrödinger equation, stated in Eq. 3.25, is solved. As a result, one is able to access all quantities of this equation. That includes the Hamiltonian matrix $\mathbf{H}$, the overlap matrix $\mathbf{S}$, eigenvalues ϵ, and the eigenvector matrix $\mathbf{C}$. The entries H_{ij} of the Hamiltonian matrix are given by all possible combinations of basis functions as stated in Eq. (3.26), whereby $\hat{h}_{KS}$ represents the KS-Hamiltonian of the dimer. Analogously, the entries of the overlap matrix are given by Eq. (3.27). In both equations, the atom-centred basis functions are represented by $\phi_i(\mathbf{r})$. Furthermore, the dimension of both matrices is given by the number of used basis functions. From that, one can see that the solution of the time-independent Schrödinger equation includes the same number of eigenvalues and eigenvectors as basis functions used.

$$\mathbf{HC} = \epsilon \mathbf{SC} \tag{3.25}$$

$$H_{ij} = \langle \phi_i(\mathbf{r})|\hat{h}_{KS}|\phi_j(\mathbf{r})\rangle \tag{3.26}$$

$$S_{ij} = \langle \phi_i(\mathbf{r})|\phi_j(\mathbf{r})\rangle \tag{3.27}$$

3.3.1.2 Decomposition of the Hamiltonian Matrix

In the present section, the decomposition of the Hamiltonian- and overlap matrix into blocks is discussed. First of all, the structure of those matrices has to be investigated. As discussed in the previous chapter, the dimension of the Hamiltonian matrix is given by the number of used basis functions. A certain number N of basis functions is localized at fragment A, whereas another number M of functions is localized at fragment B. From that, it is possible to sort the matrix entries in the Hamiltonian- and overlap matrix according to the following considerations. For a better understanding, an illustrative example of such a matrix is provided in Eq. (3.28). In that example, the same number n of basis functions is used for each fragment. The matrix entries with indices from 11 up to nn, correspond to fragment A. Those entries represent the first block in the Hamiltonian matrix, which is expressed by $\mathbf{H_A}$. Consequently, the entries with an index from $(n+1)(n+1)$ up to $(2n)(2n)$ can be identified with basis functions localized at fragment B. That corresponds to the second block and is represented by $\mathbf{H_B}$. The remaining entries in the Hamiltonian matrix include matrix elements H_{ij} with one basis function from each of the fragments. Therefore, the right upper block is represented by $\mathbf{H_{AB}}$, whereas the left block on the bottom is expressed by $\mathbf{H_{BA}}$. Notably, those blocks

are Hermitian $\mathbf{H_{AB}} = \mathbf{H_{BA}}^\dagger$. A schematic representation of the localization of basis function, on the sample of an ethylene dimer, is provided in Fig. 3.5.

$$\mathbf{H} = \begin{pmatrix} H_{11} & \dots & H_{1n} & H_{1(n+1)} & \dots & H_{1(2n)} \\ \vdots & \ddots & \vdots & \vdots & \ddots & \vdots \\ H_{n1} & \dots & H_{nn} & H_{n(n+1)} & \dots & H_{n(2n)} \\ H_{(n+1)1} & & H_{(n+1)n} & H_{(n+1)(n+1)} & \dots & H_{(n+1)(2n)} \\ \vdots & \ddots & \vdots & \vdots & \ddots & \vdots \\ H_{(2n)1} & \dots & H_{(2n)(n)} & H_{(2n)(n+1)} & \dots & H_{(2n)(2n)} \end{pmatrix} \tag{3.28}$$

Furthermore, also the overlap matrix is decomposed by following the same procedure as above. As a result, one is able to rewrite the Schrödinger equation by using the block notation as stated in Eq. (3.29). In this equation, the eigenvectors are defined as shown in Eq. (3.30). That means, the first n entries of the eigenvector correspond to fragment A, whereas the remaining values are connected to fragment B. The index l of the eigenvector refers to the corresponding energy state (eigenvalue).

$$\left(\begin{array}{c|c} \mathbf{H_A} & \mathbf{H_{AB}} \\ \hline \mathbf{H_{BA}} & \mathbf{H_B} \end{array} \right) \begin{pmatrix} \vec{c}_{A,l} \\ \vec{c}_{B,l} \end{pmatrix} = \epsilon_l \left(\begin{array}{c|c} \mathbf{S_A} & \mathbf{S_{AB}} \\ \hline \mathbf{S_{BA}} & \mathbf{S_B} \end{array} \right) \begin{pmatrix} \vec{c}_{A,l} \\ \vec{c}_{B,l} \end{pmatrix} \tag{3.29}$$

$$\begin{pmatrix} c_{1,l} \\ \vdots \\ c_{n,l} \\ \hline c_{n+1,l} \\ \vdots \\ c_{2n,l} \end{pmatrix} \rightarrow \begin{pmatrix} \vec{c}_{A,l} \\ \vec{c}_{B,l} \end{pmatrix} \tag{3.30}$$

As a next step, the block decomposition is used to separate the Hamiltonian- and overlap matrix. That means, the matrices are expressed by sums of their corresponding blocks. The mathematical expression for the Hamiltonian matrix is presented in Eq. 3.31, whereas the overlap matrix can be found in Eq. (3.32). Those expressions are plugged into the Schrödinger equation (see Eq. (3.25)), which results in an alternative representation of this equation as stated in Eq. (3.33).

$$\mathbf{H} = \left(\begin{array}{c|c} \mathbf{H_A} & \mathbf{0} \\ \hline \mathbf{0} & \mathbf{0} \end{array} \right) + \left(\begin{array}{c|c} \mathbf{0} & \mathbf{0} \\ \hline \mathbf{0} & \mathbf{H_B} \end{array} \right) + \left(\begin{array}{c|c} \mathbf{0} & \mathbf{H_{AB}} \\ \hline \mathbf{H_{BA}} & \mathbf{0} \end{array} \right) \tag{3.31}$$

$$\mathbf{S} = \left(\begin{array}{c|c} \mathbf{S_A} & \mathbf{0} \\ \hline \mathbf{0} & \mathbf{0} \end{array} \right) + \left(\begin{array}{c|c} \mathbf{0} & \mathbf{0} \\ \hline \mathbf{0} & \mathbf{S_B} \end{array} \right) + \left(\begin{array}{c|c} \mathbf{0} & \mathbf{S_{AB}} \\ \hline \mathbf{S_{BA}} & \mathbf{0} \end{array} \right) \tag{3.32}$$

$$\begin{pmatrix} \vec{c}_{A,l} \\ \vec{c}_{B,l} \end{pmatrix}^T \left[\left(\begin{array}{c|c} \mathbf{H_A} & \mathbf{0} \\ \hline \mathbf{0} & \mathbf{0} \end{array} \right) + \left(\begin{array}{c|c} \mathbf{0} & \mathbf{0} \\ \hline \mathbf{0} & \mathbf{H_B} \end{array} \right) + \left(\begin{array}{c|c} \mathbf{0} & \mathbf{H_{AB}} \\ \hline \mathbf{H_{BA}} & \mathbf{0} \end{array} \right) \right] \begin{pmatrix} \vec{c}_{A,l} \\ \vec{c}_{B,l} \end{pmatrix} =$$

$$\epsilon_l \begin{pmatrix} \vec{c}_{A,l} \\ \vec{c}_{B,l} \end{pmatrix}^T \left[\left(\begin{array}{c|c} \mathbf{S_A} & \mathbf{0} \\ \hline \mathbf{0} & \mathbf{0} \end{array} \right) + \left(\begin{array}{c|c} \mathbf{0} & \mathbf{0} \\ \hline \mathbf{0} & \mathbf{S_B} \end{array} \right) + \left(\begin{array}{c|c} \mathbf{0} & \mathbf{S_{AB}} \\ \hline \mathbf{S_{BA}} & \mathbf{0} \end{array} \right) \right] \begin{pmatrix} \vec{c}_{A,l} \\ \vec{c}_{B,l} \end{pmatrix} \tag{3.33}$$

Furthermore, the alternative representation of the time-independent Schrödinger equation, as stated in Eq. (3.33), was multiplied from the left with the eigenvector present on the right side of this equation. From that, six different scalar values can be calculated. Three of them are derived by evaluating the left side of Eq. (3.33), which are presented in Eq. (3.34),(3.35) and (3.36).

$$E_{A,l} = \begin{pmatrix} \vec{c}_{A,l}, & \vec{c}_{B,l} \end{pmatrix} \left(\begin{array}{c|c} \mathbf{H_A} & \mathbf{0} \\ \hline \mathbf{0} & \mathbf{0} \end{array} \right) \begin{pmatrix} \vec{c}_{A,l} \\ \vec{c}_{B,l} \end{pmatrix} \tag{3.34}$$

$$E_{B,l} = \begin{pmatrix} \vec{c}_{A,l}, & \vec{c}_{B,l} \end{pmatrix} \left(\begin{array}{c|c} \mathbf{0} & \mathbf{0} \\ \hline \mathbf{0} & \mathbf{H_B} \end{array} \right) \begin{pmatrix} \vec{c}_{A,l} \\ \vec{c}_{B,l} \end{pmatrix} \tag{3.35}$$

$$E_{AB,l} = \begin{pmatrix} \vec{c}_{A,l}, & \vec{c}_{B,l} \end{pmatrix} \left(\begin{array}{c|c} \mathbf{0} & \mathbf{H_{AB}} \\ \hline \mathbf{H_{BA}} & \mathbf{0} \end{array} \right) \begin{pmatrix} \vec{c}_{A,l} \\ \vec{c}_{B,l} \end{pmatrix} \tag{3.36}$$

The overlap values $S_{A,l}, S_{B,l}, S_{AB,l}$ are obtained by evaluating the right term in Eq. (3.33), whereby the corresponding mathematical definitions are analogous to the Eqs. (3.34),(3.35) and (3.36). The relation between the six scalar values is given by the Schrödinger equation, as stated in Eq. (3.37). That corresponds still to the solution of the DFT-calculation, with eigenvalues of ϵ_l. Notably, due to the orthogonality and the normalization of the eigenvectors, the sum of overlaps $(S_{A,l} + S_{B,l} + S_{AB,l})$ in Eq. (3.37) is equal to one. The physically meaning of those scalar values will be discussed in Ch. 3.3.1.5.

$$E_{A,l} + E_{B,l} + E_{AB,l} = \epsilon_l(S_{A,l} + S_{B,l} + S_{AB,l}) \tag{3.37}$$

3.3.1.3 Reduction of the System Size

In the previous chapter, a formalism to decompose the Hamiltonian- and overlap matrix was derived. Furthermore, it has been shown that it is possible to calculate different scalar values $(E_{A,l}, S_{A,l}...)$ by evaluating the alternative representation (see Eq. (3.33)) of the Schrödinger equation for a specific eigenvector. In consideration of the circumstance, that the estimation of electronic couplings is based on calculating the electronic coupling between two orbitals, a reduction of the system size is presented in this chapter. That means, the coupling between HOMO and HOMO-1 of the combined system is used to calculate the electronic coupling for holes. For the case of electrons, the LUMO and LUMO+1 are relevant. In the further course of this chapter, the case of hole couplings will be discussed. Therefore, the formalism of the previous chapter is used to evaluate the rewritten Schrödinger equation (see Eq. (3.37)) for the HOMO and HOMO-1 eigenvectors of the combined system. That results in 12 different scalar values, which are listed in Tab. 3.2. The corresponding mathematical expressions are given in Eq. (3.38) and (3.39).

$$E_{A,H} + E_{B,H} + E_{AB,H} = \epsilon_H(S_{A,H} + S_{B,H} + S_{AB,H}) \tag{3.38}$$

$$E_{A,H-1} + E_{B,H-1} + E_{AB,H-1} = \epsilon_{H-1}(S_{A,H-1} + S_{B,H-1} + S_{AB,H-1}) \tag{3.39}$$

To summarize, the system size is reduced by taking just two eigenvectors of the combined system. The obtained scalar values are the basis for the upcoming definition of a theoretical two-state system as presented in the next chapter.

Tab. 3.2: List of calculated values by using the Block Decomposition formalism. The two different orbitals are given by the HOMO and HOMO-1 of the combined system solution. $E_{X,l}$ represents energy parts of fragment X in the lth eigenstate. Analogous the overlaps $S_{X,l}$. The relation between those values is given in Eq. (3.37)

	$\mathbf{E_{A,l}}$	$\mathbf{E_{B,l}}$	$\mathbf{E_{AB,l}}$	$\mathbf{S_{A,l}}$	$\mathbf{S_{B,l}}$	$\mathbf{S_{AB,l}}$
HOMO	$E_{A,H}$	$E_{B,H}$	$E_{AB,H}$	$S_{A,H}$	$S_{B,H}$	$S_{AB,H}$
HOMO-1	$E_{A,H-1}$	$E_{B,H-1}$	$E_{AB,H-1}$	$S_{A,H-1}$	$S_{B,H-1}$	$S_{AB,H-1}$

3.3.1.4 Theoretical Two-State System

In the present chapter, a theoretical two-state system is constructed. That system is later used to obtain the on-site energies of the fragments in the combined system. The idea is to reproduce Eq. (3.38) and Eq. (3.39) by suitable matrix representations. For that purpose, one can define two matrix equations of the dimension 2×2 as stated in Eq. (3.40) and (3.41) by introducing $(1,1)$ vectors.

$$\begin{pmatrix} 1, & 1 \end{pmatrix} \begin{pmatrix} E_{A,H} & \frac{E_{AB,H}}{2} \\ \frac{E_{AB,H}}{2} & E_{B,H} \end{pmatrix} \begin{pmatrix} 1 \\ 1 \end{pmatrix} = \epsilon_H \begin{pmatrix} 1, & 1 \end{pmatrix} \begin{pmatrix} S_{A,H} & \frac{S_{AB,H}}{2} \\ \frac{S_{AB,H}}{2} & S_{B,H} \end{pmatrix} \begin{pmatrix} 1 \\ 1 \end{pmatrix} \tag{3.40}$$

$$\begin{pmatrix} 1, & 1 \end{pmatrix} \begin{pmatrix} E_{A,H-1} & \frac{E_{AB,H-1}}{2} \\ \frac{E_{AB,H-1}}{2} & E_{B,H-1} \end{pmatrix} \begin{pmatrix} 1 \\ 1 \end{pmatrix} = \epsilon_{H-1} \begin{pmatrix} 1, & 1 \end{pmatrix} \begin{pmatrix} S_{A,H-1} & \frac{S_{AB,H-1}}{2} \\ \frac{S_{AB,H-1}}{2} & S_{B,H-1} \end{pmatrix} \begin{pmatrix} 1 \\ 1 \end{pmatrix} \tag{3.41}$$

As a next step, both matrix equations (Eqs. (3.40),(3.41)) are summed, which results in Eq. (3.42). In that equation, the matrix $\mathbf{H_1 + H_2}$ is defined as stated in Eq. (3.43). Furthermore, the corresponding overlap matrices $\mathbf{S_{1,2}}$ are presented in Eq. (3.44). The vector $\mathbf{c}$ is defined by $(1,1)^T$. That represents also the final result for the theoretical two-state system. Important is the fact, that $\epsilon_{H,H-1}$ are indeed the HOMO and HOMO-1 energies of the DFT-calculation. However, this system has no further physically meaning at this stage.

$$\mathbf{c}^T(\mathbf{H_1 + H_2})\mathbf{c} = \mathbf{c}^T(\epsilon_H \mathbf{S_1} + \epsilon_{H-1}\mathbf{S_2})\mathbf{c} \tag{3.42}$$

$$\mathbf{H_1 + H_2} = \begin{pmatrix} E_{A,H} + E_{A,H-1} & \frac{E_{AB,H}}{2} + \frac{E_{AB,H-1}}{2} \\ \frac{E_{AB,H}}{2} + \frac{E_{AB,H-1}}{2} & E_{B,H} + E_{B,H-1} \end{pmatrix} \tag{3.43}$$

$$\mathbf{S_1} = \begin{pmatrix} S_{A,H} & \frac{S_{AB,H}}{2} \\ \frac{S_{AB,H}}{2} & S_{B,H} \end{pmatrix}, \mathbf{S_2} = \begin{pmatrix} S_{A,H-1} & \frac{S_{AB,H-1}}{2} \\ \frac{S_{AB,H-1}}{2} & S_{B,H-1} \end{pmatrix} \tag{3.44}$$

3.3.1.5 Estimation of On-Site Energies

The first part of this chapter discusses the solution of a general eigenvalue problem. In general, the problem can be defined as stated in Eq. (3.45), whereby $\mathbf{E}$ represents the identity matrix. For the discussion, an eigenvalue problem of the dimension 2×2, which is presented in Eq. (3.46), is investigated. The entries of the matrices are given by arbitrary on-site energies and an electronic coupling t_{AB}.

$$\mathbf{A}\mathbf{c} = \epsilon \mathbf{E}\mathbf{c} \tag{3.45}$$

$$\begin{pmatrix} e_1 & t_{12} \\ t_{21} & e_2 \end{pmatrix} \begin{pmatrix} c_1 \\ c_2 \end{pmatrix} = \epsilon_l \begin{pmatrix} 1 & 0 \\ 0 & 1 \end{pmatrix} \begin{pmatrix} c_1 \\ c_2 \end{pmatrix} \tag{3.46}$$

The solution of the eigenvalue problem is found by diagonalizing the matrix $\mathbf{A}$, i.e. the left matrix in Eq. (3.46). That results in two eigenvalues as stated in Eq. (3.47).

$$\epsilon_{1,2} = \frac{e_1 + e_2}{2} \pm \frac{1}{2}\sqrt{(e_1 - e_2)^2 + (2t_{12})^2} \tag{3.47}$$

Furthermore, one is able to calculate the difference of the eigenvalues, which is shown in Eq. (3.48).

$$\Delta E_{12} = \epsilon_1 - \epsilon_2 = \sqrt{(e_1 - e_2)^2 + (2t_{12})^2} \tag{3.48}$$

At this point, the results of the previous chapters get relevant. First of all, the eigenvalues $\epsilon_{1,2}$ are assumed to be the HOMO and HOMO-1 energies of the DFT-calculation, i.e. $\epsilon_1 = \epsilon_H$ and $\epsilon_2 = \epsilon_{H-1}$. Hence, the splitting ΔE_{12} can be expressed by using the mathematical relations stated in Eq. (3.38) and (3.39). Note, that the sum of the overlap parts equals one in those equations. As a result, the corresponding equation for the energy splitting ΔE_{12} is presented in Eq. (3.49).

$$\Delta E_{12} = E_{A,H} + E_{B,H} + E_{AB,H} - E_{A,H-1} - E_{B,H-1} - E_{AB,H-1} \tag{3.49}$$

The main idea of the Block Decomposition method is to use Eq. (3.48) to calculate the electronic coupling t_{12} from the known energy splitting ΔE_{12} between two eigenvalues, e.g. HOMO and HOMO-1. However, to be able to extract the electronic coupling, it is necessary to determine the on-site energies $e_{1,2}$. For that purpose, one can start with considering the relations between energy splitting, on-site energies and electronic coupling. An illustrative diagram of those values is provided in Fig. 3.6.
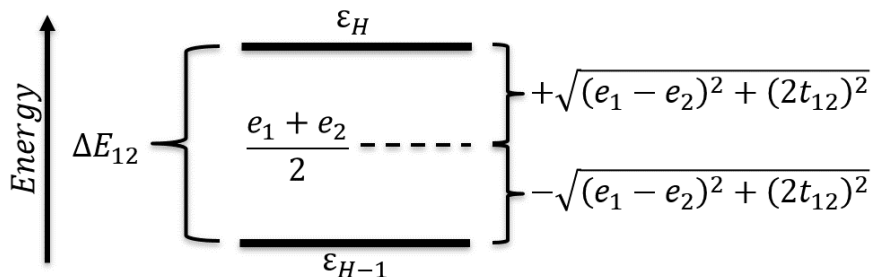
Fig. 3.6: Illustration of energy splitting ΔE_{12} between ϵ_H (HOMO) and ϵ_{H-1} (HOMO-1). The position of centre is given by the half of the sum of on-site energies $e_{1,2}$. Therefore, the energy of the orbitals are determined by adding/subtracting $\sqrt{(e_1 - e_2)^2 + (2t_{12})^2}$, whereby t_{12} represents the electronic coupling.

The diagram indicates, that the summation of the orbital energies $\epsilon_{H,H-1}$ results in a cancellation of the square-root terms. Therefore, a simple relation between the orbital energies and on-site energies $e_{1,2}$ is obtained, which is presented in Eq. (3.50). Unfortunately, that relation does not uniquely determine the on-site energies, i.e. there are infinite possibilities for the summation $e_1 + e_2$.

$$\epsilon_1 + \epsilon_2 \equiv \epsilon_H + \epsilon_{H-1} = e_1 + e_2 \tag{3.50}$$

Furthermore, this relation can be written in matrix notation as stated in Eq. (3.51), whereby the vectors have to be defined as (1,1).

$$\begin{pmatrix} 1, & 1 \end{pmatrix} \begin{pmatrix} e_1 & 0 \\ 0 & e_2 \end{pmatrix} \begin{pmatrix} 1 \\ 1 \end{pmatrix} = e_1 + e_2 = \epsilon_H + \epsilon_{H-1} \tag{3.51}$$

For the next step, the theoretical two-state system, stated in Eq. (3.42), is required. That system was constructed according to the shape of Eq. (3.51). However, there are deviations of the theoretical construct compared to the above-shown relation, namely the off-diagonal elements are non-zero. For tackling the deviations and to be able to estimate physically right on-site energies, the matrix $\mathbf{H_1} + \mathbf{H_2}$ is of great interest. The idea is to transform this matrix to identify the diagonal entries of the transformed matrix as an approximation for the on-site energies of the fragments. This transformation is based on the following considerations. Firstly, the diagonal elements of $\mathbf{H_1} + \mathbf{H_2}$ (see Eq. (3.43)) are given by $E_{A,H} + E_{A,H-1}$ and $E_{B,H} + E_{B,H-1}$. These sums of scalar values are assigned to fragment A and fragment B, respectively. However, those values just include small contributions of the interaction between the fragments in the combined system. Hence, the main amount of interaction is found in the off-diagonal elements in Eq. (3.43), i.e. $\frac{E_{AB,H}}{2} + \frac{E_{AB,H-1}}{2}$. Therefore, the off-diagonal and the diagonal elements must be combined by a suitable transformation $\mathbf{T}$ to allocate the amount of interaction to fragment A and fragment B. Furthermore, that allocation has to include the constraint of physically reasonable on-site energies as outcome. An additional requirement for the

transformation matrix is that it should have approximately the shape of an identity matrix. From that, the transformation matrix $\mathbf{T}$ is defined by means of the overlap matrices from Eq. (3.44) as stated in Eq. (3.52).

$$\mathbf{T} = (\mathbf{S_1} + \mathbf{S_2})^{-1} \tag{3.52}$$

As a next step, the transformation matrix is applied to the theoretical two-state system. That means, the matrix $\mathbf{T}$ is inserted between the vector $\mathbf{c}^T$ and the matrix $(\mathbf{H_1} + \mathbf{H_2})$ in Eq. (3.42), which results in Eq. (3.53). The right term equals to $\epsilon_H + \epsilon_{H-1}$ due to the overlap sum equals one.

$$\mathbf{c}^T(\mathbf{S_1} + \mathbf{S_2})^{-1}(\mathbf{H_1} + \mathbf{H_2})\mathbf{c} = \mathbf{c}^T(\epsilon_H\mathbf{S_1} + \epsilon_{H-1}\mathbf{S_2})\mathbf{c} \tag{3.53}$$

The left matrix in the transformed two-state system (see Eq. (3.53)) is defined as stated in Eq. (3.54), whereby $\mathbf{H} = \mathbf{H_1} + \mathbf{H_2}$. The values $\widetilde{e}_{1,2}$ represent the on-site energies of the fragments derived by the transformation, whereas the off-diagonal elements are without a physically meaning. Note that the issue with missing uniqueness of the relation stated in Eq. (3.51) is solved by inserting the transformation matrix, i.e. allocating the interaction to the fragments.

$$(\mathbf{S_1} + \mathbf{S_2})^{-1}(\mathbf{H_1} + \mathbf{H_2}) = \mathbf{TH} = \begin{pmatrix} \widetilde{e}_1 & \delta_{d_1} \\ \delta_{d_2} & \widetilde{e}_2 \end{pmatrix} \tag{3.54}$$

Furthermore, the transformed two-state system is rewritten in matrix notation (see Eq. (3.55)) in analogy to Eq. (3.51). The matrix in Eq. (3.55) includes off-diagonal elements. i.e. δ_{d_1} and δ_{d_2}, due to the imperfection of the transformation. Those values are neglected for the estimation of the electronic coupling (see Ch. 3.3.1.6) due to the fact that for the estimation of the electronic coupling only the difference between $\widetilde{e}_1$ and $\widetilde{e}_2$ is relevant.

$$(1, \quad 1) \begin{pmatrix} \widetilde{e}_1 & \delta_{d_1} \\ \delta_{d_2} & \widetilde{e}_2 \end{pmatrix} \begin{pmatrix} 1 \\ 1 \end{pmatrix} = \widetilde{e}_1 + \widetilde{e}_2 + \delta_{d_1} + \delta_{d_2} = \epsilon_H + \epsilon_{H-1} \tag{3.55}$$

The final on-site energies $\widetilde{e}_{1,2}$ derived by the transformation are explicitly given in Eq. (3.56) and (3.57), whereas the off-diagonal elements are stated in Eq. (3.58) and (3.59). For the sake of clarity, the factor c is defined separately in Eq. (3.60).

$$\widetilde{e}_1 = \frac{1}{c}\left[(S_B^H + S_B^{H-1})(E_A^H + E_A^{H-1}) - (\frac{S_{AB}^H}{2} + \frac{S_{AB}^{H-1}}{2})(\frac{E_{AB}^H}{2} + \frac{E_{AB}^{H-1}}{2})\right] \tag{3.56}$$

$$\widetilde{e}_2 = \frac{1}{c}\left[(S_A^H + S_A^{H-1})(E_B^H + E_B^{H-1}) - (\frac{S_{AB}^H}{2} + \frac{S_{AB}^{H-1}}{2})(\frac{E_{AB}^H}{2} + \frac{E_{AB}^{H-1}}{2})\right] \tag{3.57}$$

$$\delta_{d_1} = \frac{1}{c}\left[(S_B^H + S_B^{H-1})(\frac{E_{AB}^H}{2} + \frac{E_{AB}^{H-1}}{2}) - (\frac{S_{AB}^H}{2} + \frac{S_{AB}^{H-1}}{2})(E_B^H + E_B^{H-1})\right] \tag{3.58}$$

$$\delta_{d_2} = \frac{1}{c} \left[(S_A^H + S_A^{H-1}) \left(\frac{E_{AB}^H}{2} + \frac{E_{AB}^{H-1}}{2} \right) - \left(\frac{S_{AB}^H}{2} + \frac{S_{AB}^{H-1}}{2} \right) (E_A^H + E_A^{H-1}) \right] \quad (3.59)$$

$$c = (S_A^H + S_A^{H-1})(S_B^H + S_B^{H-1}) - \left(\frac{S_{AB}^H}{2} + \frac{S_{AB}^{H-1}}{2} \right)^2 \quad (3.60)$$

3.3.1.6   The Final Result of Block Decomposition

In the previous chapter, the on-site energies $\widetilde{e}_{1,2}$ were defined by using a theoretical two-state system. Those values are explicitly expressed in the Eqs. (3.56) and (3.57). Furthermore, the electronic splitting ΔE_{12} between two eigenvalues, e.g. HOMO and HOMO-1, is stated in Eq. (3.48). The mathematical relation of those values is given by Eq. (3.48). To calculate the electronic coupling, this equation is rearranged as shown in Eq. (3.61). That presents the final result for the Block Decomposition method.

$$\boxed{t_{12} = \pm\sqrt{(\Delta E_{12})^2 - (\widetilde{e}_1 - \widetilde{e}_2)^2}} \quad (3.61)$$

Notably, the Block Decomposition method estimates the absolute value of the electronic coupling, i.e. the sign is not determined. However, there are applications where the sign of the electronic couplings is important. For that purpose, the formalism has to be adapted, which is done by using the decomposed coefficient vectors, stated in Eq. (3.30). That adaption is still ongoing.

3.3.2 Implementation

The implementation of the Block Decomposition method is realized as post-processing tool for the DFT-package FHI-*aims*. That package is used to perform the DFT-calculation of the combined system. As a result, several quantities as described in the previous chapters are accessible. The right order of basis functions is crucial, in order to be able to decompose the Hamiltonian/overlap matrix into blocks. That is assured by sorting the atoms in the geometry input file by fragments. As a next step, the block decomposition of those matrices is performed. The block representatives are used to calculate all quantities which are listed in Tab. 3.2. That means, the HOMO and HOMO-1 are used for hole couplings, whereas the LUMO and LUMO+1 for electron couplings. However, there are a few exceptions to this choice of orbitals, which are discussed in Ch. 5.1.1.2. As a next step, the on-site energies are calculated according to Eqs. (3.56) and (3.57). Furthermore, the electronic splitting is evaluated by using Eq. (3.48). Finally, the mathematical relation, as stated in Eq. (3.61), allows to estimate the electronic coupling t_{12}. The source code, written in Python 2.7, is provided in the appendix.

3.4 Tight-Binding Fit

In this chapter the tight-binding concept is discussed and the mathematical formalism is derived step by step. That results in the derivation of two model functions, which are later used for the fitting approach. For the following procedure, an overview of the description of periodic systems and their respective electronic structures is given in Ch. 2.1.

3.4.1 Theory

The tight-binding formalism starts with the definition of a wave function describing the chemical environment in any unit cell of the lattice. That is based on a linear combination of orbitals, whereby only the frontier orbitals are used. Regarding the case of molecular crystals, this means the molecular HOMO or LUMO states and their corresponding single electron wave functions ϕ_i^{MO} are the origin for a linear ansatz to describe the frontier bands. This results in Eq. (3.62).

$$\Psi_{unitcell}(\mathbf{r}) = \sum_i c_i \phi_i^{MO}(\mathbf{r} - \mathbf{r_i}) \tag{3.62}$$

The next step is to rewrite the wave function in an appropriate way to describe the electronic structure considering the periodicity of the lattice. Therefore, Bloch's-theorem is used to construct a new function of the form given by Eq. (3.63). The concept of this theorem is given by Eq. (3.64), whereby $\hat{T}_{\mathbf{G'}}$ represents a translation operator. This operator shifts the wave function into another unit cell, indicated by the vector $\vec{G}$. The vector $\vec{G} = n\mathbf{a}_1 + m\mathbf{a}_2 + l\mathbf{a}_3$ is given by a linear combination of lattice vectors $\mathbf{a_i}$, including the integer numbers n, m, l. Finally, by applying the operator to the Bloch-like function $\Psi_{\mathbf{k}}$ one can see that the function remains unchanged but a phase factor has to be included.

$$\Psi_{\mathbf{k}}(\mathbf{r}) = \frac{1}{\sqrt{N}} \sum_{\mathbf{G}} e^{i\mathbf{k}\mathbf{G}} \Psi_{unitcell}(\mathbf{r} - \mathbf{G}) = \frac{1}{\sqrt{N}} \sum_{\mathbf{G}} e^{i\mathbf{k}\mathbf{G}} \sum_i c_i \phi_i^{MO}(\mathbf{r} - \mathbf{r_i} - \mathbf{G}) \tag{3.63}$$

$$\hat{T}_{\mathbf{G'}} \Psi_{\mathbf{k}}(\mathbf{r}) = \Psi_{\mathbf{k}}(\mathbf{r} + \mathbf{G'}) = e^{i\mathbf{k}\mathbf{G'}} \Psi_{\mathbf{k}}(\mathbf{r}) \tag{3.64}$$

The k-dependent wave function is now used to evaluate the Schrödinger equation as shown in Eq. (3.65). For doing so, one has to multiply a molecular orbital ϕ_n^{MO} from the left. Therefore, all functions which are used in the linear combination have to be included. A general expression of the extended Schrödinger equation is stated in Eq. (3.66). The first term represents the on-site energies. The next term includes an important assumption made in the tight-binding concept, namely just the nearest neighbours are included in the sum over m. Owing to this fact, a small deviation of δ_e is added to the equation. On the right side, the eigenenergy ϵ and the overlaps of the wave functions are present. Due to the fact that only frontier orbitals are used in the ansatz,

the assumption of zero overlap between neighbouring orbitals is made. Therefore, also here a small value indicated by δ_o is added.

$$\left\langle \phi_i^{MO} \middle| \hat{H} \middle| \Psi_\mathbf{k} \right\rangle = \epsilon \left\langle \phi_i^{MO} \middle| \Psi_\mathbf{k} \right\rangle \tag{3.65}$$

$$c_n \left\langle \phi_n^{MO} \middle| \hat{H} \middle| \phi_n^{MO} \right\rangle + \sum_m c_m \left\langle \phi_n^{MO} \middle| \hat{H} \middle| \phi_m^{MO} \right\rangle e^{i\mathbf{kG}} + \delta_e = \epsilon c_n \left\langle \phi_n^{MO} \middle| \phi_n^{MO} \right\rangle + \delta_o \tag{3.66}$$

The tight-binding principle is based on the above-mentioned assumptions. The next task is to derive two suitable model functions for the application of the fitting method. That starts with the final expression of the Schrödinger equation as stated in Eq. (3.66). Therefore, for every included wave function in the unit cell, there is one such equation, with the coefficients c_n. Here, it has to be distinguished between the case of more wave functions localized on one molecule or one wave function localized on different molecules. A combination of them is also possible, but in this work the focus lies on the latter one.

One molecule per unit cell:

First of all, the model function for one molecule A, described with one molecular orbital per unit cell $\phi_A^{MO}(\mathbf{r}-\mathbf{r_A})$, is discussed. For that purpose, the evaluated time-independent Schrödinger equation (see Eq. (3.66)) is used to derive Eq. (3.67). Here the small deviations are neglected and it is assumed that the wave functions corresponding to different unit cells are orthogonal. Furthermore, the on-site term is included in the sum over the neighbours, which means the null vector $m = \mathbf{G_0}$ is part of $\{\mathbf{G_m}\}$. As a next step, the electronic couplings, explicitly given in Eq. (3.68), are replaced with t_m to simplify the expression to Eq. (3.69). The latter also represents the final result for the model function.

$$\sum_{m \in \{\mathbf{G_m}\}} \left\langle \phi_n^{MO}(\mathbf{r} - \mathbf{r_A}) \middle| \hat{H} \middle| \phi_n^{MO}(\mathbf{r} - \mathbf{r_A} - \mathbf{G_m}) \right\rangle e^{i\mathbf{kG_m}} = \epsilon(\mathbf{k}) \tag{3.67}$$

$$t_m = \left\langle \phi_n^{MO}(\mathbf{r} - \mathbf{r_A}) \middle| \hat{H} \middle| \phi_n^{MO}(\mathbf{r} - \mathbf{r_A} - \mathbf{G_m}) \right\rangle \tag{3.68}$$

$$\epsilon(\mathbf{k}) = \sum_{m \in \{\mathbf{G_m}\}} t_m e^{i\mathbf{kG_m}} \equiv t_0 + \sum_{m \in \{\mathbf{G_m}\}, m \neq \mathbf{G_0}} t_m e^{i\mathbf{kG_m}} \tag{3.69}$$

Two molecules per unit cell:

The case of two molecules A, B per unit cell, described by one molecular orbital each $\phi_A(\mathbf{r} - \mathbf{r_A}), \phi_B(\mathbf{r} - \mathbf{r_B})$, is investigated next. Again, the first step is to evaluate the Schrödinger equation for both wave functions following Eq. (3.66). In the present case, one gets two equations, corresponding to each molecular orbital. The linear system of equations is shown in Eq. (3.70) and (3.71). The first terms in both equations include the couplings between equivalent molecules, therefore $A - A$ and $B - B$ interactions. The second term contains couplings between the different types of molecules in the unit cell, indicated by $A - B$. In order to solve this system, the equations are rewritten as

stated in Eq. (3.73) using matrix notation. For simplicity the electronic couplings are defined via Eq. (3.72), whereby X, Y represent the localization site.

$$I : c_A \sum_{m \in \{\mathbf{G_m}\}} t_m^{AA} e^{i\mathbf{kG_m}} + c_B \sum_{n \in \{\mathbf{G_n}\}} t_n^{AB} e^{i\mathbf{kG_n}} = c_A \epsilon(\mathbf{k}) \tag{3.70}$$

$$II : c_B \sum_{m \in \{\mathbf{G_m}\}} t_m^{BB} e^{i\mathbf{kG_m}} + c_A \sum_{n \in \{\mathbf{G_n}\}} t_n^{BA} e^{i\mathbf{kG_n}} = c_B \epsilon(\mathbf{k}) \tag{3.71}$$

$$t_m^{XY} = \left\langle \phi_X^{MO}(\mathbf{r} - \mathbf{r_X}) \middle| \hat{H} \middle| \phi_Y^{MO}(\mathbf{r} - \mathbf{r_Y} - \mathbf{G_m}) \right\rangle \tag{3.72}$$

$$\begin{pmatrix} \sum_{m \in \{\mathbf{G_m}\}} t_m^{AA} e^{i\mathbf{kG_m}} & \sum_{n \in \{\mathbf{G_n}\}} t_n^{AB} e^{i\mathbf{kG_n}} \\ \sum_{n \in \{\mathbf{G_n}\}} t_n^{BA} e^{i\mathbf{kG_n}} & \sum_{m \in \{\mathbf{G_m}\}} t_m^{BB} e^{i\mathbf{kG_m}} \end{pmatrix} \begin{pmatrix} c_A \\ c_B \end{pmatrix} = \epsilon_{\mathbf{k}} \begin{pmatrix} c_A \\ c_B \end{pmatrix} \tag{3.73}$$

The solution of the 2×2 eigenvalue problem is obtained by diagonalizing the matrix on the left side of Eq. (3.73). This results in two eigenvalues $\epsilon_{1,2}$, which also represent the k-dependent model function for two molecules per unit cell as stated in Eq. (3.74). The explicit expressions for the $H_{XY}(\mathbf{k})$ values are given in Eq. (3.68).

$$\epsilon_{1,2}(\mathbf{k}) = \frac{H_{AA}(\mathbf{k}) + H_{BB}(\mathbf{k})}{2} \pm \sqrt{\frac{(H_{AA}(\mathbf{k}) - H_{BB}(\mathbf{k}))^2}{4} + H_{AB}(\mathbf{k})H_{BA}(\mathbf{k})} \tag{3.74}$$

$$H_{XY}(\mathbf{k}) = \sum_{m \in \{\mathbf{G_m}\}} t_m^{XY} e^{i\mathbf{kG_m}} \tag{3.75}$$

For understanding the functionality and construction of the obtained model function, an example of a 1D-system is shown next. The illustrative system of two molecules A, B per unit cell, repeated in the direction $\mathbf{a_1}$, is presented in Fig. 3.7. First of all, the symmetric terms AA, BB are constructed, whereby the resulting equation is stated in Eq. (3.76). The first parameter t_{off}^{AA} describes the on-site energy of molecule A, where the phase factor equals one. The coupling between molecule A at the middle unit cell to molecule A localized at the right ($+\mathbf{a_1}$) is represented by t_{a1}^{AA} and to the left ($-\mathbf{a_1}$) by t_{-a1}^{AA}. In the present case, those are equal for symmetry reasons $t_{a1}^{AA} = t_{-a1}^{AA}$. The couplings for molecule B can be derived analogously.

$$H_{AA} = t_{off}^{AA} + t_{a1}^{AA} e^{i\mathbf{ka_1}} + t_{-a1}^{AA} e^{-i\mathbf{ka_1}} \tag{3.76}$$

For the couplings between different types A, B, one can write the expression stated in Eq. (3.77). The first parameter t_0^{AB} describes the coupling between A and B in the middle unit cell. Due to that, the corresponding phase factor equals one. The next coupling t_{a1}^{AB} originates from molecule A in the middle to molecule B at the right unit cell. In the opposite direction, the coupling t_{-a1}^{AB} can be stated. Important at this point is the fact that those couplings are not the same. The couplings from molecule B in the middle unit cell to molecules of type A can be derived analogous as shown in Eq. (3.78). From
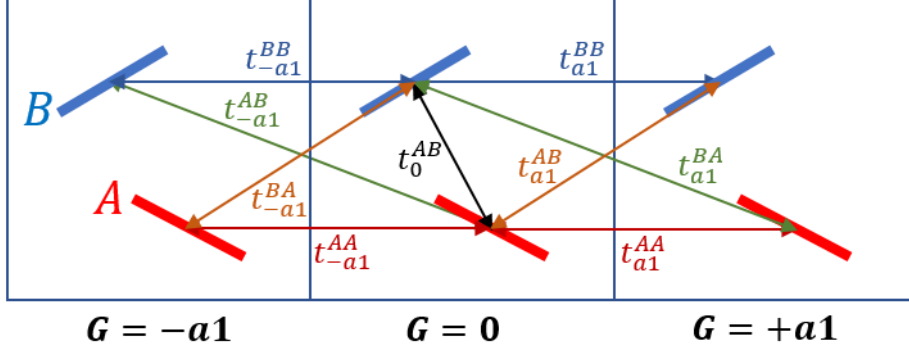
Fig. 3.7: Illustrative example of a system containing two molecules A, B per unit cell. The periodicity is given by the vector $\mathbf{a_1}$. The graph shows the couplings between the nearest and next nearest neighbours.

that, it is possible to identify equalities of couplings, namely $t_{a1}^{AB} = t_{-a1}^{BA}$, $t_{-a1}^{AB} = t_{a1}^{BA}$ and $t_0^{AB} = t_0^{BA}$.

$$H_{AB} = t_0^{AB} + t_{a1}^{AB} e^{i\mathbf{ka_1}} + t_{-a1}^{AB} e^{-i\mathbf{ka_1}} \tag{3.77}$$

$$H_{AB} = t_0^{BA} + t_{a1}^{BA} e^{i\mathbf{ka_1}} + t_{-a1}^{BA} e^{-i\mathbf{ka_1}} \tag{3.78}$$

The constructed expressions for H_{AA}, H_{BB}, H_{AB} and H_{BA} are now plugged into Eq. (3.74), which results in Eq. (3.79). The latter represents the tight-binding model function for the above-shown system. For simplification of this equation, one can rewrite the exponential terms by using Euler's formula $e^{iy} = cos(x) + isin(x)$. Further, one can for example neglect next nearest neighbours, which results in Eq. (3.80). Note, that in general all derived tight-binding functions have to fulfil the constraint of lattice periodicity $E(\mathbf{k}) = E(\mathbf{k} + \mathbf{P})$, whereby $\mathbf{P}$ represents a reciprocal lattice vector.

$$\epsilon_{1,2}(\mathbf{k}) = \frac{t_{off}^{AA} + t_{a1}^{AA} e^{i\mathbf{ka_1}} + t_{-a1}^{AA} e^{-i\mathbf{ka_1}} + t_{off}^{BB} + t_{a1}^{BB} e^{i\mathbf{ka_1}} + t_{-a1}^{BB} e^{-i\mathbf{ka_1}}}{2}$$

$$\pm \left[\frac{(t_{off}^{AA} + t_{a1}^{AA} e^{i\mathbf{ka_1}} + t_{-a1}^{AA} e^{-i\mathbf{ka_1}} - t_{off}^{BB} - t_{a1}^{BB} e^{i\mathbf{ka_1}} - t_{-a1}^{BB} e^{-i\mathbf{ka_1}})^2}{4} \right.$$

$$\left. + (t_0^{AB} + t_{a1}^{AB} e^{i\mathbf{ka_1}} + t_{-a1}^{AB} e^{-i\mathbf{ka_1}})(t_0^{BA} + t_{a1}^{BA} e^{i\mathbf{ka_1}} + t_{-a1}^{BA} e^{-i\mathbf{ka_1}}) \right]^{\frac{1}{2}} \tag{3.79}$$

$$\epsilon_{1,2}(\mathbf{k}) = \frac{t_{off}^{AA} + 2t_{|a1|}^{AA}cos(\mathbf{ka_1}) + t_{off}^{BB} + 2t_{|a1|}^{BB}cos(\mathbf{ka_1})}{2}$$
$$\pm \left[\frac{(t_{off}^{AA} + 2t_{|a1|}^{AA}cos(\mathbf{ka_1}) - t_{off}^{BB} - 2t_{|a1|}^{BB}cos(\mathbf{ka_1}))^2}{4} \right.$$
$$\left. + (t_0^{AB})^2 + (t_{a1}^{AB})^2 + 2t_0^{AB}t_{a1}^{AB}cos(\mathbf{ka_1}) \right]^{\frac{1}{2}} \quad (3.80)$$

3.4.2 Implementation

The implementation of the tight-binding method is realized by a modular concept. The coding language is Python, which includes several advantages for the fitting procedure. First of all, a suitable fitting package called LMFit is integrated. That is used to construct a universal fit module, which is explained in detail further below. Furthermore, additional modules including read functions, plot routines and analysis tools are developed to provide a fully functioning package. The most relevant tools are listed below, whereby the corresponding source codes are given in the appendix. The present implementation is written for data derived with FHI-*aims*, but can be easily adapted to other DFT-packages.

- **Fitting module:** The most relevant module includes all functions regarding the fitting process itself. The two main functions are *construct_parameters()* and *tight_binding()*. The first one initializes all necessary quantities for the fit, like parameters, initial values and names of the fit parameters. The input for the present function is simply a set of linear combinations of lattice vectors, which represent the included neighbours for the fit. The second function from above includes the main task of fitting the model function to appropriate DFT-data. Therefore, two model functions, explained in Ch. 3.4, are implemented. Hence, the number of fit parameters is not fixed and the functions are generated at every call automatically. For the fit procedure, the package LMFit is used. That means the *minimize()* function is used in combination with the above-mentioned functions to fit the analytical function. The minimization is based on calculating the residual of the model function with respect to the DFT-data by varying the fit parameters according to a chosen algorithm. The LMfit-package provides different methods for the purpose of fitting. For example, that would be Levenberg-Marquardt [38, 39], Powell [40], Conjugate-Gradient [41] and Nelder-Mead [42]. Nevertheless, to rate the quality of the fit, a statistical evaluation is needed. In this work, the results are analysed by taking the mean-squared-error and the square root of it. The corresponding mathematical expressions are given in Eq. (3.81) and (3.82), whereby $\epsilon_{\mathbf{k}}$ represents the value of the analytical function and $\hat{\epsilon}_{\mathbf{k}}$ states the DFT-value. The total number of fitted data points is given by N.

$$MSE = \frac{1}{N} \sum_{i=1}^{N} (\epsilon_{\mathbf{k}} - \hat{\epsilon}_{\mathbf{k}})^2 \tag{3.81}$$

$$RMSE = \sqrt{\frac{1}{N} \sum_{i=1}^{N} (\epsilon_{\mathbf{k}} - \hat{\epsilon}_{\mathbf{k}})^2} \tag{3.82}$$

- **Effective mass module:** For the estimation of the effective mass, one has to evaluate the second derivative of the analytical function $\epsilon(\mathbf{k})$. The corresponding expression for the model function, describing one molecule per unit cell, is shown in Eq. (3.83).

$$\frac{\partial^2 \epsilon(\mathbf{k})}{\partial k_i \partial k_j} = \frac{\partial^2}{\partial k_i \partial k_j} \sum_{m \in \{\mathbf{G_m}\}} t_m e^{i\mathbf{k}\mathbf{G_m}} \equiv - \sum_{m \in \{\mathbf{G_m}\}} t_m G_{m,i} G_{m,j} e^{i\mathbf{k}\mathbf{G_m}} \tag{3.83}$$

More complex is the case for two molecules per unit cell, which is demonstrated in Eq. (3.84). The first and second derivations of this expression are given in Eq. (3.85) and (3.86).

$$
\begin{aligned}
\frac{d^2 \epsilon_{1,2}(\mathbf{k})}{d\mathbf{k}^2} &= \frac{H''_{AA}(\mathbf{k}) + H''_{BB}(\mathbf{k})}{2} \\
&\mp \frac{\left(\frac{1}{2}(H_{AA}(\mathbf{k}) - H_{BB}(\mathbf{k}))(H'_{AA}(\mathbf{k}) - H'_{BB}(\mathbf{k})) + 2H_{AB}(\mathbf{k})H'_{AB}(\mathbf{k})\right)^2}{4\left(\frac{1}{2}(H_{AA}(\mathbf{k}) - H_{BB}(\mathbf{k}))^2 + H_{AB}(\mathbf{k})^2\right)^{\frac{3}{2}}} \\
&\pm \frac{\frac{1}{2}(H_{AA}(\mathbf{k}) - H_{BB}(\mathbf{k}))(H''_{AA}(\mathbf{k}) - H''_{BB}(\mathbf{k})) + \frac{1}{2}(H'_{AA}(\mathbf{k}) - H'_{BB}(\mathbf{k}))^2}{2\sqrt{\frac{1}{4}(H_{AA}(\mathbf{k}) - H_{BB}(\mathbf{k}))^2 + H_{AB}(\mathbf{k})^2}} \\
&\pm \frac{2H_{AB}(\mathbf{k})H''_{AB}(\mathbf{k}) + 2H'_{AB}(\mathbf{k})^2}{2\sqrt{\frac{1}{4}(H_{AA}(\mathbf{k}) - H_{BB}(\mathbf{k}))^2 + H_{AB}(\mathbf{k})^2}} \tag{3.84}
\end{aligned}
$$

$$H'_{XY}(\mathbf{k}) = \frac{\partial H_{XY}(\mathbf{k})}{\partial k_i} = \sum_{m \in \{\mathbf{G_m}\}} i t_m^{XY} G_{m,i} e^{i\mathbf{k}\mathbf{G_m}} \tag{3.85}$$

$$H''_{XY}(\mathbf{k}) = \frac{\partial^2 H_{XY}(\mathbf{k})}{\partial k_i \partial k_j} = - \sum_{m \in \{\mathbf{G_m}\}} t_m^{XY} G_{m,i} G_{m,j} e^{i\mathbf{k}\mathbf{G_m}} \tag{3.86}$$

The result of taking the second derivative is the inverse effective mass tensor as discussed in Ch. 2.3.

- **Analysis module:** This module is written to analyse the band structure by decomposing it. That means, the bands can be split according to the contributing electronic couplings. For that purpose, two different functions are available, namely *crop()* and *add()*. The former starts with the full analytical function from the fit and neglects contributions of chosen directions/neighbours. The *add()* function starts at the opposite end and builds the band from zero by adding desired couplings. The input for both functions is given by the corresponding names of the fit parameters, which should be included/neglected.

- **Plotting module:** This module allows to plot electronic band structures in an appropriate way. Therefore, the k-paths are scaled by their lengths of chosen reciprocal points. The input requires a selection of k-points and the corresponding reciprocal lattice vectors.

4 Test Systems

This chapter presents different systems to test and benchmark the obtained methodologies of the previous chapters. For the validation of the Fragment Orbital implementation and Block Decomposition method, the so-called HAB11 database is shown. That database was proposed by Kubas et al. [43] in their work about benchmarking different density functional based methodologies. Therefore, the use of this database allows a comparison of the Block Decomposition method with other cluster-based approaches. For the tight-binding method, two organic semiconductors are used as test systems. The first one is quinacridone in the α-phase. This allows performing several tests on a one molecule per unit cell system. Pentacene is presented as second system. It includes two molecules per unit cell and, therefore, it is used to test the second model function from Ch. 3.4.
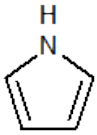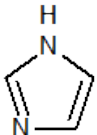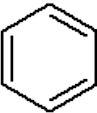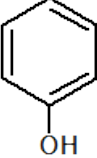
4.1 HAB11 Database

The HAB11 database including 11 different organic molecules is shown in Tab. 4.1. For a detailed description of the database and relevant chemical properties of the molecules see [43]. The choice of molecules is based on the idea of providing a wide spread on different bond types and chemical structures. The database listed in the above-mentioned table gives the structures of the molecules, while for the subsequent tests dimers are used.

4.2 Quinacridone

Quinacridone provides a great variety of different polymorphs. There are at least three stable phases α, β, γ, but even more have been measured in the past [44]. Quinacridone is widely used as a pigment, due to its red-violet appearance. The chemical structure of a single molecule of quinacridone is shown in Fig. 4.2. For the purpose of fitting a

Tab. 4.1: Chemical structures as well as the related names of molecules, which are included in the HAB11 database. For benchmark calculations, symmetric dimers are used. A schematic illustration for the construction of the corresponding symmetric dimers is given in Fig. 5.1. A more detailed description of the database can be found in the work of Kubas Et al. [43].

Name	Structure	Name	Structure
Ethylene	$H_2C\!=\!CH_2$	Pyrrole	
Acetylene	$HC\!\equiv\!CH$	Thiophene	
Cyclopropene		Imidazole	
Cyclobutadiene		Benzene	
Cyclopentadiene		Phenol	
Furane			

**Tab. 4.2:** Lattice parameters of the quinacridone α-phase and of pentacene. Both systems are of the same triclinic P-1 crystal class. The quinacridone α-phase includes one molecule per unit cell. The respective lattice parameters and the 3D-structure were taken from [44]. Pentacene consists of two molecules per unit cell. The corresponding parameters such as the 3D-structure are derived from [47].

	Quinacridone	Pentacene
Structure	triclinic P-1	triclinic P-1
$\mathbf{a}$ / Å	3.802	6.275
$\mathbf{b}$ / Å	6.612	7.714
$\mathbf{c}$ / Å	14.485	14.442
α / °	100.680	76.752
β / °	94.400	88.011
γ / °	102.110	84.524

tight-binding function to the electronic structure, the α polymorph turns out to be an ideal test system. The chemical environment in each lattice direction is quite different in the α-phase. That includes π-stacking, H-bonding and van der Waals interactions. Furthermore, the α-phase contains just one molecule per unit cell, which allows testing the simple tight-binding function discussed in Ch. 3.4. The lattice structure of the quinacridone α-phase is illustrated in Fig. 4.1. The corresponding lattice vectors and the geometry are taken from Paulus et al. [44]. Further, the values of the lattice vectors and angles can be found in Tab. 4.2. The crystalline structure of the present phase is triclinic, whereby the corresponding 1st-Brillouin zone is shown in Fig. 4.3.

4.3 Pentacene

For the sake of testing the tight-binding model function describing two molecules per unit cell, the well-known organic semiconductor pentacene is investigated. The structure of a pentacene molecule is given by five benzene rings, as shown in Fig. 4.4. In the periodic case, pentacene shows layers forming a herringbone structure, whereby different spacings between the layers are related to different polymorphs [46]. In this work, the phase measured by Holmes et al. [47] is studied. The corresponding lattice and the geometry of the present system are illustrated in Fig. 4.5. The values for lattice vectors and angles are tabulated in Tab. 4.2. Furthermore, this lattice shows a triclinic crystalline structure consisting of two molecules per unit cell. The corresponding 1st-Brillouin zone is illustrated in Fig. 4.3.
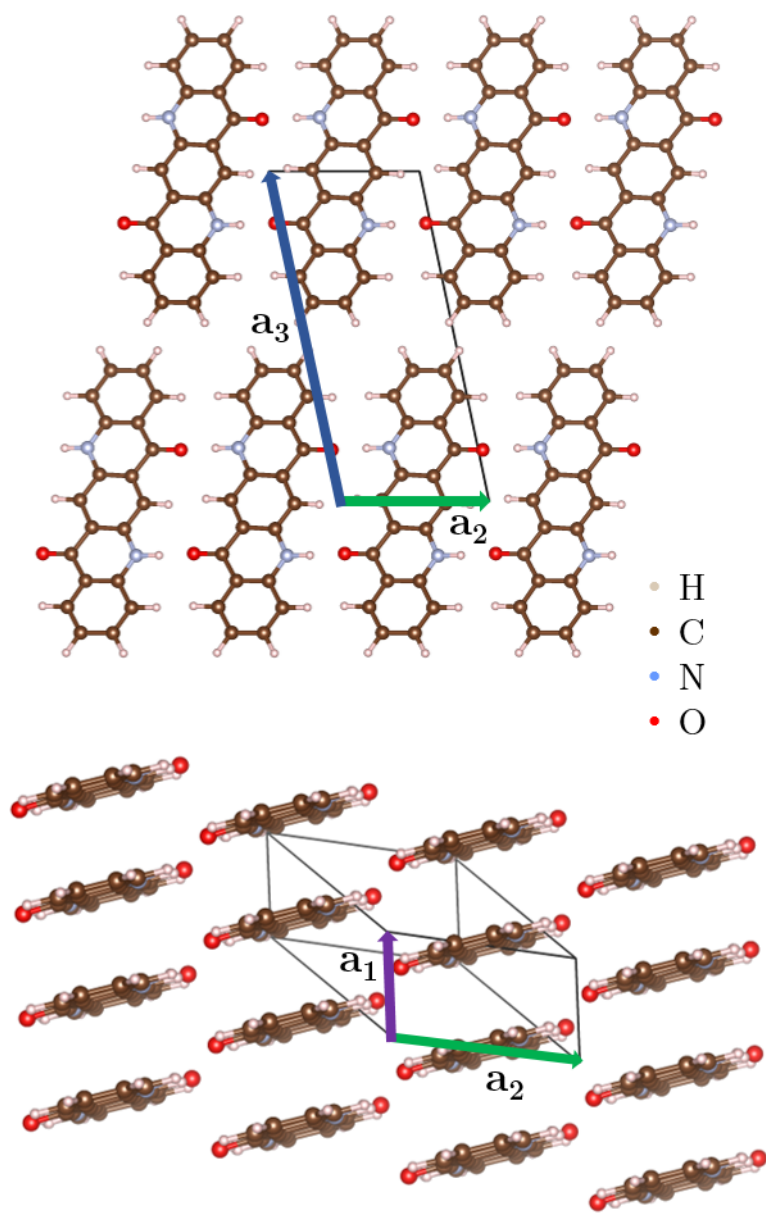
Fig. 4.1: The quinacridone α-phase and its corresponding triclinic crystal structure. The lattice vectors spanning the primitive unit cell are given by $\mathbf{a_1}, \mathbf{a_2}, \mathbf{a_3}$. Numerical values for the present structure are tabulated in Tab. 4.2.
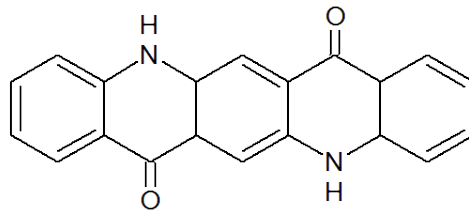
Fig. 4.2: Chemical structure of quinacridone. Molecular formula: $C_{20}H_{12}N_2O_2$
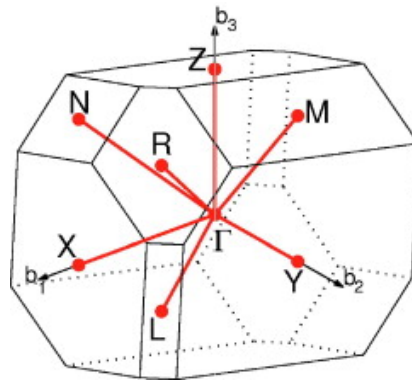
Fig. 4.3: The 1st-Brillouin zone of the triclinic P-1 structures of quinacridone α-phase and pentacene. The corresponding k-path of high-symmetry directions is given by $X-\Gamma-Y|L-\Gamma-Z|N-\Gamma-M|R-\Gamma$. Reprinted from [45], Copyright (2019), with permission from Elsevier.
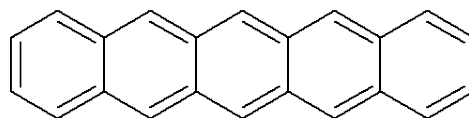
Fig. 4.4: Chemical structure of pentacene. Molecular formula: $C_{22}H_{14}$
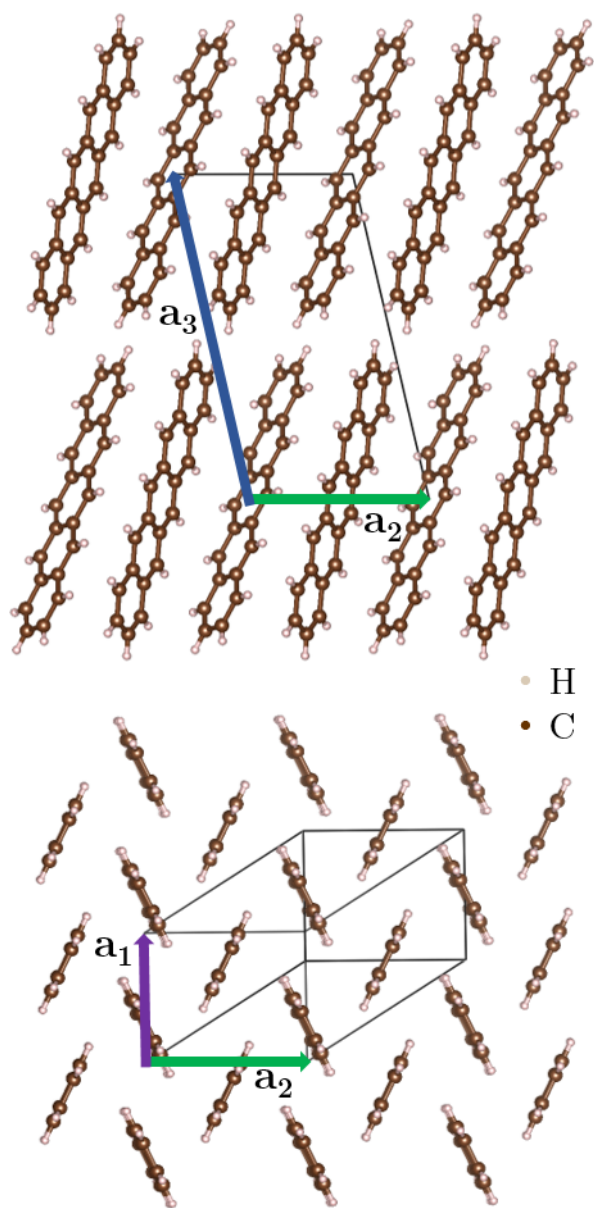
Fig. 4.5: Pentacene and its corresponding triclinic crystal structure. The structure consists of two molecules per unit cell. The lattice vectors spanning the primitive unit cell are given by $\mathbf{a_1}, \mathbf{a_2}, \mathbf{a_3}$. Numerical values for the present structure are tabulated in Tab. 4.2.

5 Modelling Results

5.1 Validation of Cluster-Based Methods

This chapter is about the validation of the previously discussed cluster-based methods. A set of different dimers, namely the HAB11 database, are used to test the functionality and limits of the approaches. The first part of this chapter is based on the latest research from Kubas et al. [43]. They performed a Benchmark of Constrained Density Functional Theory (CDFT), Fragment Orbital Density Functional Theory (FODFT) and Fragment Orbital Density Functional Tight Binding (FODFTB) against high-level ab-initio calculations. Particularly, they calculated the electronic couplings of a chosen test set by varying the spacing of symmetric dimers. Therefore, their results and the respective high-level ab-initio calculations are going to serve as a reference for the first part of this chapter, which investigates such symmetric dimers. The second part discusses the non-symmetric case, where dimers are rotated from a face-to-face into a (non-symmetric) face-to-edge configuration. That investigation is related to the work of Valeev et al. [35].

5.1.1 Distance Variation

The simple case of different symmetric dimers forms the basis of the first validation step. As a first step, the geometry of all molecules (HAB11 database) was optimized using FHI-*aims* [9] and the PBE [7] functional. A list of relevant settings used in the optimization calculations can be found in Tab. 5.1. Moreover, the 2nd-tier, tight settings were used as basis set for all atoms in the structure.

Tab. 5.1: Main settings of DFT-calculations using FHI-*aims* for cluster and periodic systems. The meaning of each Keyword can be found in the application manual of the FHI-*aims* package, see [49].

Keyword	Setting
relativistic	atomic_zora scalar
spin	none
charge	0.0
sc_accuracy_eev	1E-2
sc_accuracy_etot	1E-5
sc_accuracy_rho	1E-4
sc_accuracy_forces	5E-4
vdw_correction_hirshfeld	.true.
compensate_multipole_errors	.true.
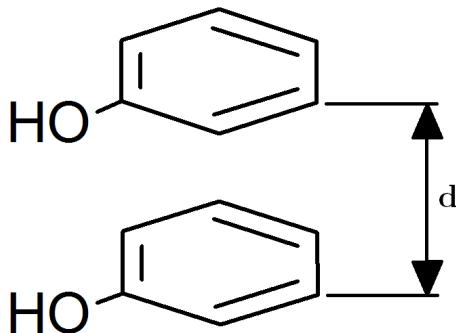
Fig. 5.1: Schematic illustration of varying the distance in a dimer for the example of phenol. Both molecules are aligned to enter a symmetric face-to-face configuration. The spacing is given by the parameter d.

Furthermore, the van der Waals correction according to [48] was applied. After relaxing the geometries, symmetric dimers were constructed as schematically shown in Fig. (5.1). The corresponding alignment of molecules is called a face-to-face configuration. For every molecule, four symmetric dimers with different spacings d of 3.5, 4.0, 4.5 and 5.0 Å were built. The geometry input files were written with the right order of atoms in it, which is important for the application of post-processing tools. That means, the files start with all atoms of molecule A followed by the atoms of molecule B. The next step included the single-point calculations with DFT, in order to solve the electronic structures. Again, the FHI-*aims* package was used with the same settings from above (now without a geometry relaxation). Convergence was tested for the basis set with respect to the change of electronic couplings derived by the procedures as described below. The use of 2nd-tier, tight settings turned out to be sufficient, due to the minimal change (magnitude of sub-meV) in the electronic couplings when using a higher amount of basis functions (e.g. including also 3rd-tier functions). For showing the influence of exact exchange-energy two calculations for every system were performed, one using the PBE functional and a second one employing the hybrid functional PBE0 [8]. The corresponding discussion is shown in the next sub-chapter. For the estimation of the hole couplings, the post-processing tools implemented as discussed in Ch. 3 were applied to the electronic structures obtained by the DFT-calculations. I.e. the molecular HOMO orbitals of the fragments were used for the Fragment Orbital approach. For the Block decomposition method, the HOMO and HOMO-1 of the combined system were picked. The Electronic Splitting in Dimers (ESD) method was also applied to estimate the hole couplings. In this case the splitting was taken from the HOMO and HOMO-1 states of the corresponding DFT-calculations. A table including the obtained results for the absolute values of hole couplings of the HAB11 database can be found in Tab. 5.2. The table shows also high-level ab-initio results as reference data. The values for the hole couplings are taken from Kubas et al. [43]. In their work they performed MRCI+Q [50, 51] (multi reference configuration interaction + Davidson correction [52]) and NEVPT2 [53, 54] (n-electron valence perturbation theory) calculations, which allow a sophisticated esti-

mation of electronic couplings. Nevertheless, these approaches are very computational expensive and, therefore, not suitable for bigger systems. Furthermore, also results obtained with the implementation of the Fragment Orbital approach in FHI-*aims* are listed in Tab. 5.2. Those values are taken from the work of C. Schober et al. [55].

Discussion: The results for the absolute values of hole couplings, tabulated in Tab. 5.2, are visualized in Fig. 5.2. The hole couplings obtained with the PBE functional coincide between Electronic Splitting in Dimers (ESD), Fragment Orbital (FO) and Block Decomposition (BD) method. That can be explained by the theoretical construction of all three approaches. For example, the Block Decomposition method is based on taking the energy splitting for the estimation of couplings. Therefore, for the symmetric case and using the PBE functional, it is equal to the ESD approach.
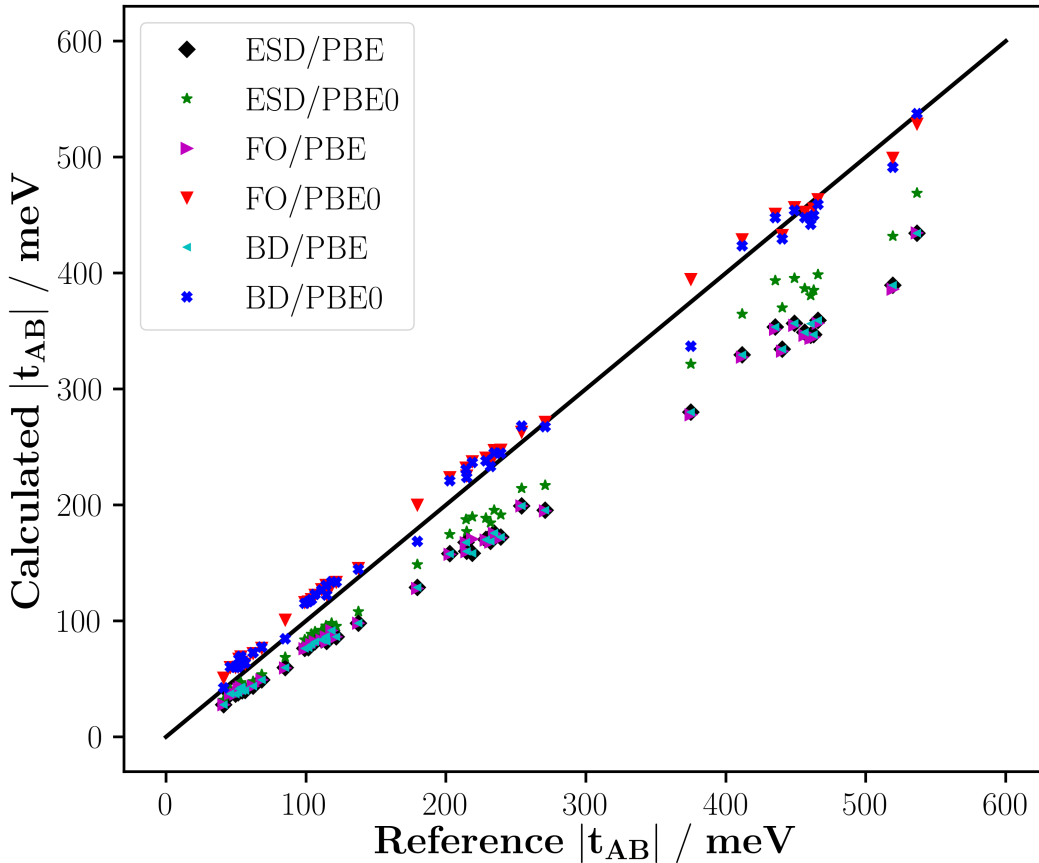
Fig. 5.2: Absolute values of hole couplings $|t_{AB}|$ calculated with Electronic Splitting in Dimers (ESD), Fragment Orbital (FO) and Block Decomposition (BD) method. The graph shows the correlation between those methodologies compared to high-level ab-initio reference data [43]. The couplings were derived with PBE and the hybrid functional PBE0.

The Fragment Orbital method uses single electron wave functions of the individual molecules, derived with DFT, as basis. Therefore, the coupling between the resulting orbitals spanning an orthogonal basis yield an energy splitting (nearly) equal to the other methodologies. This is not valid for all cases, e.g. if the isolated fragments are no longer a suitable basis for the combined system. The results obtained with the cluster-based methods linearly underestimate the reference values derived with high-level ab-initio calculations. To test the influence of non-local exchange energy, the hybrid functional PBE0 was used (see next sub-chapter for a detailed description). The ESD method improves slightly compared to the reference values. The energy splitting determined by the Block Decomposition method is now different (relative to the ESD results) due to the fact of the theoretical definition as stated in Ch. 3.3. Therefore, the obtained results are higher in absolute values and can match up with the high-level reference data. The same behaviour occurs in the case of the Fragment Orbital method. Here, the hybrid calculations of the isolated fragments show slightly different shaped HOMOs compared to the PBE case. For all dimers in the HAB11 database, that results in a higher effective hole coupling. Note that, this behaviour of an increase is not observed for every chemical system (e.g. certain directions in quinacridone α-phase). Summarizing, this section supports the suitability of both methodologies applied to different symmetric dimer systems. The results coincide at various distances as well as for different chemical structures. Further by using hybrid functionals the Fragment Orbital and Block Decomposition method can compete with high-level computations as shown above.

Tab. 5.2: HAB11 database: Results for absolute values of hole couplings $|t_{AB}|$ of symmetric dimers at various distances. The table shows couplings derived with Fragment Orbital (FO), Block Decomposition (BD) and the Electronic Splitting method (ESD). Dist. represents the spacing of the dimers in Å. Ref. are reference values from high-level ab-initio calculations [43](^{a}MRCI+Q, ^{b}NEVPT2). AIMS are values derived with the FO implementation of FHI-*aims*, taken from [43]. All couplings are given in meV.

	Dist.	Ref.	FO			BD		ESD	
			AIMS	PBE	PBE0	PBE	PBE0	PBE	PBE0
Ethylene	3.5	519.2^a	381.2	386.1	499.2	389.4	491.2	389.4	431.8
	4	270.8	193.4	194.9	271.3	195.4	267.4	195.4	216.8
	4.5	137.6	97.4	98.0	145.4	98.0	144.6	98.0	108.1
	5	68.5	49.0	49.2	76.7	49.1	77.5	49.1	53.6
Acetylene	3.5	460.7^a	340.1	343.8	448.3	356.3	441.9	346.3	380.7
	4	231.8	166.8	168.1	236.1	168.5	233.1	168.5	184.7
	4.5	114.8	81.8	82.1	122.9	82.2	122.4	82.2	89.2
	5	56.6	40.1	40.2	63.0	40.1	63.8	40.1	42.9
Cyclo-propene	3.5	536.6^a	436.7	434.7	528.5	434.4	537.3	434.4	468.8
	4	254	200.8	199.2	262.8	199.2	268.1	199.2	214.4
	4.5	118.4	92.7	91.8	130.3	91.8	133.7	91.8	97.9
	5	54.0	43.1	42.7	64.5	42.7	66.7	42.7	44.9
Cyclo-butadiene	3.5	462.7^a	339.9	344.5	455.3	346.9	449.8	347.0	385.2
	4	239.1	170.3	171.8	247.4	172.2	244.7	172.2	191.4
	4.5	121.7	85.6	86.3	133.5	86.3	133.4	86.3	95.4
	5	62.2	43.3	43.6	71.9	43.6	72.6	43.6	47.7
Cyclo-pentadiene	3.5	465.8^a	352.2	356.6	463.5	359.2	459.1	359.2	398.6
	4	234.4	174.0	175.3	247.1	175.8	244.9	175.8	195.3
	4.5	114.3	86.0	86.4	130.8	86.5	130.5	86.5	95.6
	5	53.4	42.6	42.8	69.1	42.8	69.4	42.8	46.8
Furane	3.5	440.3^a	328.7	332.6	432.6	334.3	429.4	334.3	370
	4	214.9	158.5	159.7	225.1	160.0	223.8	160.0	177.1
	4.5	101.8	76.5	76.9	116.5	77.0	116.5	77.0	84.7
	5	46.0	37.0	37.2	60.1	37.2	60.4	37.2	40.5
Pyrrole	3.5	456.3^a	340.0	346.4	452.6	349.0	447.6	349.0	386.5
	4	228.6	167.5	169.6	240.7	170.1	238.1	170.2	188.5
	4.5	111.3	82.6	83.5	127.2	83.6	126.6	83.6	92.0
	5	52.2	41.0	41.3	67.1	41.3	67.2	41.3	45.0

|								
Thiophene	3.5	449.0[b]	349.3	354.8	456.7	356.6	454	356.6	395.4
	4	218.9	168.7	170.6	237.5	158.4	236.6	158.4	189.7
	4.5	106.5	81.3	82.0	122.4	82.1	122.8	82.1	90.6
	5	54.4	39.3	39.5	62.8	39.6	63.4	39.6	43.2
Imidazole	3.5	411.6[b]	323.7	327.4	428.8	329.4	423.3	329.4	364.5
	4	202.8	156.2	157.4	223.6	157.8	220.8	157.9	174.5
	4.5	99.1	75.7	76.0	115.9	76.2	115.1	76.2	83.6
	5	49.7	36.8	36.9	59.9	36.9	59.9	36.9	40.1
Benzene	3.5	435.2[b]	346.4	351.5	450.8	353.3	447.6	353.3	393.5
	4	214.3	165.8	167.4	232	167.8	230.7	167.8	187.3
	4.5	104	79.1	79.7	118.5	79.7	118.2	79.7	88.7
	5	51.7	37.7	37.9	60.4	37.9	60.3	38.0	41.8
Phenol	3.5	375.0[b]	273.3	277.7	394.6	280.0	337	280.0	321.3
	4	179.6	126.6	128.1	200	128.8	168.7	128.8	148.6
	4.5	85.2	58.8	59.3	100.8	59.6	84.6	59.6	68.7
	5	41.3	27.5	27.7	50.8	27.8	42.4	27.8	31.8

5.1.1.1 Influence of Hartree-Fock Exchange

For the symmetric dimers included in the HAB11 database, the use of hybrid functionals increases the absolute value of the effective hole couplings, as shown above. In this sub-chapter, a short discussion about the influence of non-local exchange-energy, so-called Hartree-Fock exchange (HFX), for the case of a symmetric dimer is given. The studied system is phenol, which is also part of the HAB11 database. First, the behaviour of the Fragment Orbital method is investigated. The influence of different amounts of exchange-energy at various distances is illustrated in Fig. 5.3. The reference is given by high-level ab-initio calculations as already discussed in the previous chapter. It can be seen that for small spacings the amount of about 25 % is needed to keep up with the reference values. At larger distances the necessary amount of HFX decreases, which comes along with less interaction between the molecules. The dependence of the absolute value of hole couplings on the amount of HFX is shown in Fig. 5.4 for different distances. A linear dependence occurs for all four spacings in the dimer. The gradient decreases by increasing the spacing between the molecules, which is in agreement with the above-mentioned influence at larger distances. The Block decomposition method shows a similar behaviour: The results for the absolute hole couplings in phenol at various distances with different amounts of HFX are shown in Fig. 5.5. In this case, the amount of 37.5 % HFX at small distances is slightly higher as for the Fragment Orbital approach. Furthermore, at larger distances, the influence decreases but not as much as in the former case. Therefore, the amount of HFX needed to increase the absolute values

of the effective hole couplings are slightly higher through all distances for Block decomposition compared to the Fragment Orbital approach. A possible explanation for that can be found by the isolated fragments used in the Fragment Orbital method. The use of hybrid functionals enhances the delocalization of the HOMOs in the stacking direction (observed for phenol). Therefore, in the combined system the electronic coupling is most likely overestimated by using the isolated HOMOs as basis. Conversely, the Block Decomposition method is based on results of the combined system, whereby the behaviour of de-/localization acts different. In this case, the bonding between molecules is included, which results in less delocalization with the same amount of HFX. Nevertheless, the dependence of absolute couplings as a function of HFX shows a similar behaviour for the Block Decomposition method, as is shown in Fig. 5.6. Also in this case, the linear proportionality is given, whereby the gradient is slightly smaller compared to Fragment Orbital.
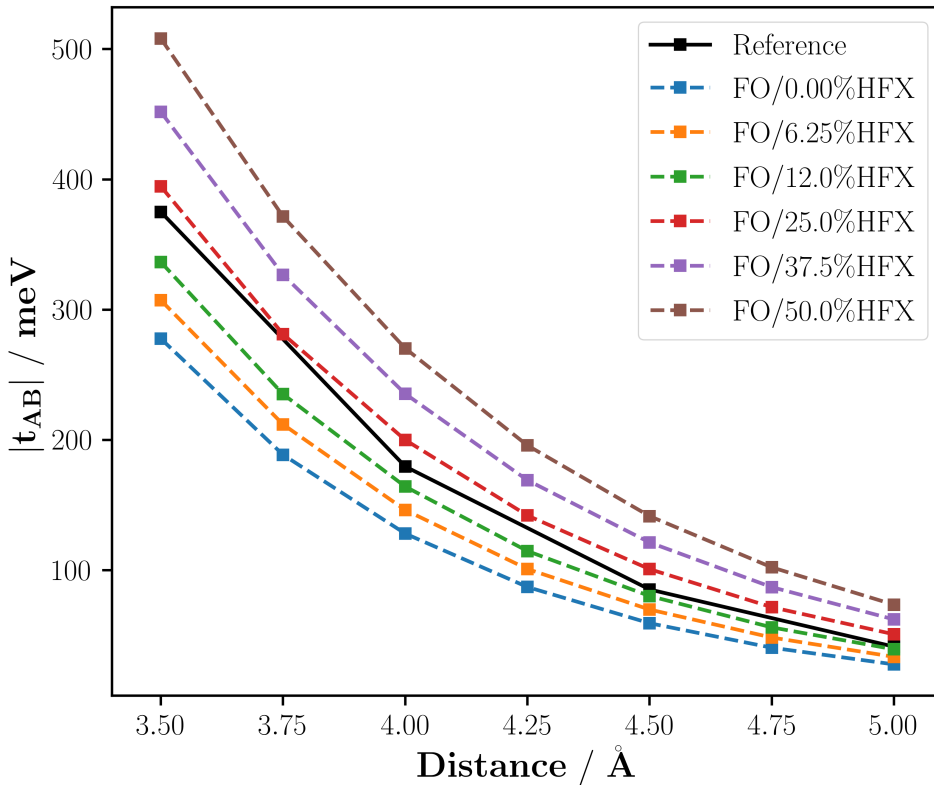
Fig. 5.3: Influence of Hartree Fock exchange-energy (HFX) on the absolute values of hole couplings derived with the **Fragment Orbital** approach for the example of phenol. The graph shows the evolution of the coupling with different amounts of HFX at various distances. Reference are results from high-level ab-initio calculations (NEVPT2), taken from [43].
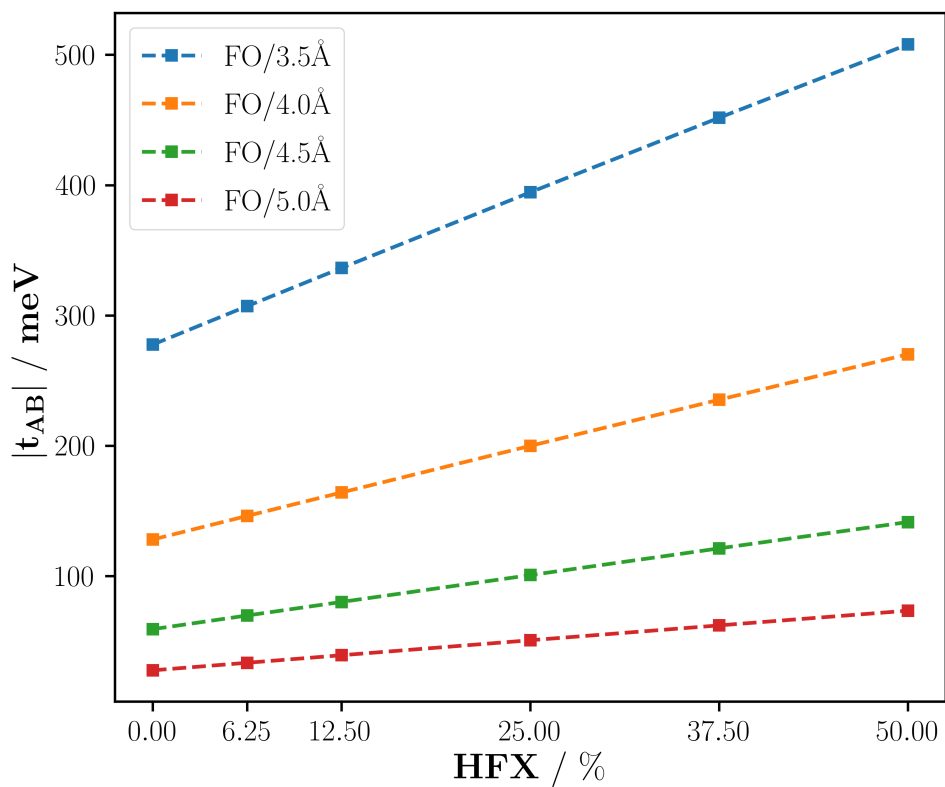
Fig. 5.4: Correlation between distance and amount of Hartree-Fock exchange-energy (HFX). The graph shows absolute values of hole couplings of the symmetric phenol dimer derived with **Fragment Orbital**. The four lines represent the different distances between the molecules in the dimer.
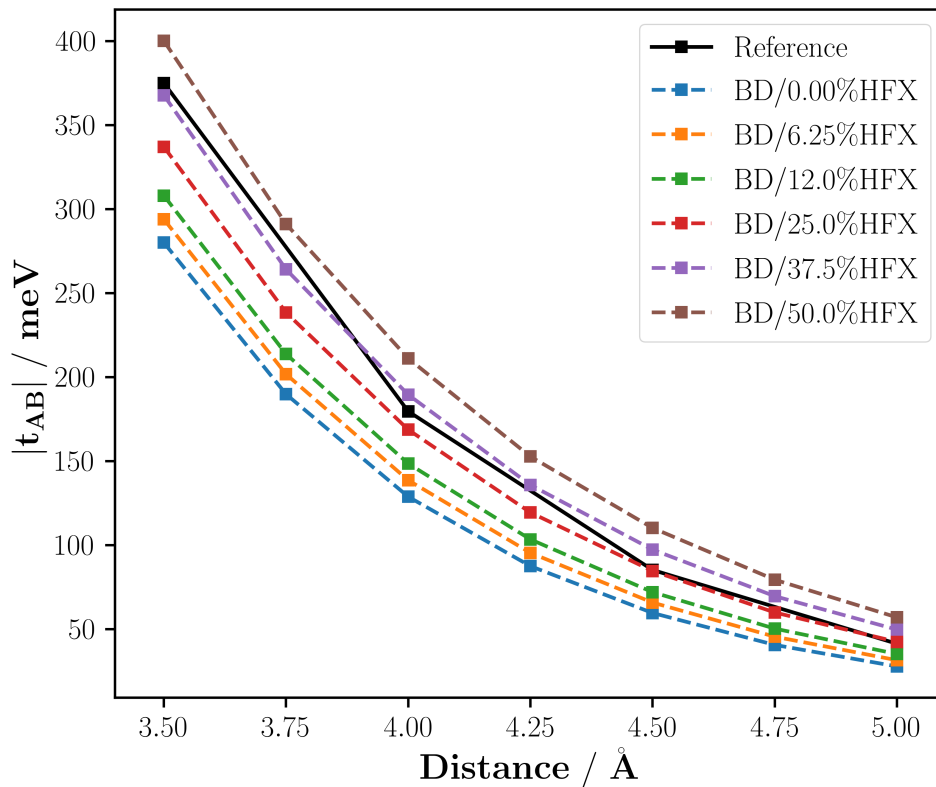
Fig. 5.5: Influence of Hartree Fock exchange-energy (HFX) on the absolute values of hole couplings derived with the **Block Decomposition** approach for the example of phenol. The graph shows the evolution of the coupling with different amounts of HFX at various distances. Reference are results from high-level ab-initio calculations (NEVPT2), taken from [43].
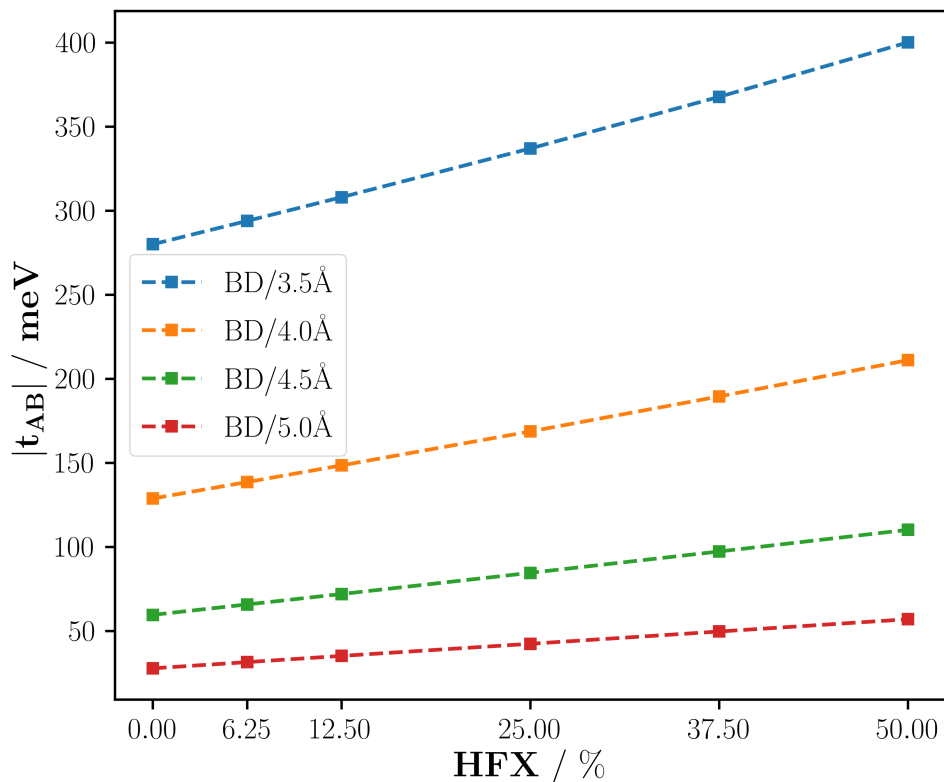
Fig. 5.6: Correlation between distance and amount of Hartree-Fock exchange-energy (HFX). The graph shows absolute values of hole couplings of the symmetric phenol dimer derived with **Block Decomposition**. The four lines represent the different distances between the molecules in the dimer.

5.1.1.2 Picking the Right Orbitals

In previous chapters (3.3, 3.2 and 5.1.1) the problem of picking the right orbitals for describing electronic couplings within the Fragment Orbital and Block Decomposition method was mentioned. The present discussion is based on two different dimer systems, namely ethylene and acetylene. In Fig. 5.7 one can see the corresponding orbitals of those systems derived with DFT. As already stated in Ch. 3.2, the Fragment Orbital approach is based on using single electron wave functions of the isolated fragments for the description of the combined system. For example, the hole couplings can be derived by using the HOMO states of the molecules. Solving the corresponding Schrödinger equation results in two states, a bonding and anti-bonding one. In Fig. 5.7 one can see that for ethylene this would coincide with the HOMO and HOMO-1 of the respective DFT calculation. Therefore, the Fragment Orbital approach describes the right coupling for holes. For the Block Decomposition method, the HOMO and HOMO-1 lead to the same result. However, the case of acetylene shows a quite different behaviour. The visualization of the corresponding orbitals indicates that the HOMO and HOMO-3 belong together and represent the anti-bonding and bonding linear combination of the

HOMOs of the molecules. In between, there are two different states, which are formed by the HOMO-1 states of the molecules. Therefore, one has to keep in mind that the Fragment Orbital approach estimates the coupling between HOMO and HOMO-3 when considering the HOMO states of the isolated molecules. Importantly, the Block Decomposition method has to be applied also on those states to get the same result. That means the Block Decomposition method allows to calculate any coupling between states of the combined system. However, to obtain comparable results between both methodologies, one has to be sure that the above-mentioned case is treated in the right way.

	Ethylene	Acetylene
HOMO		
HOMO-1		
HOMO-2		
HOMO-3		
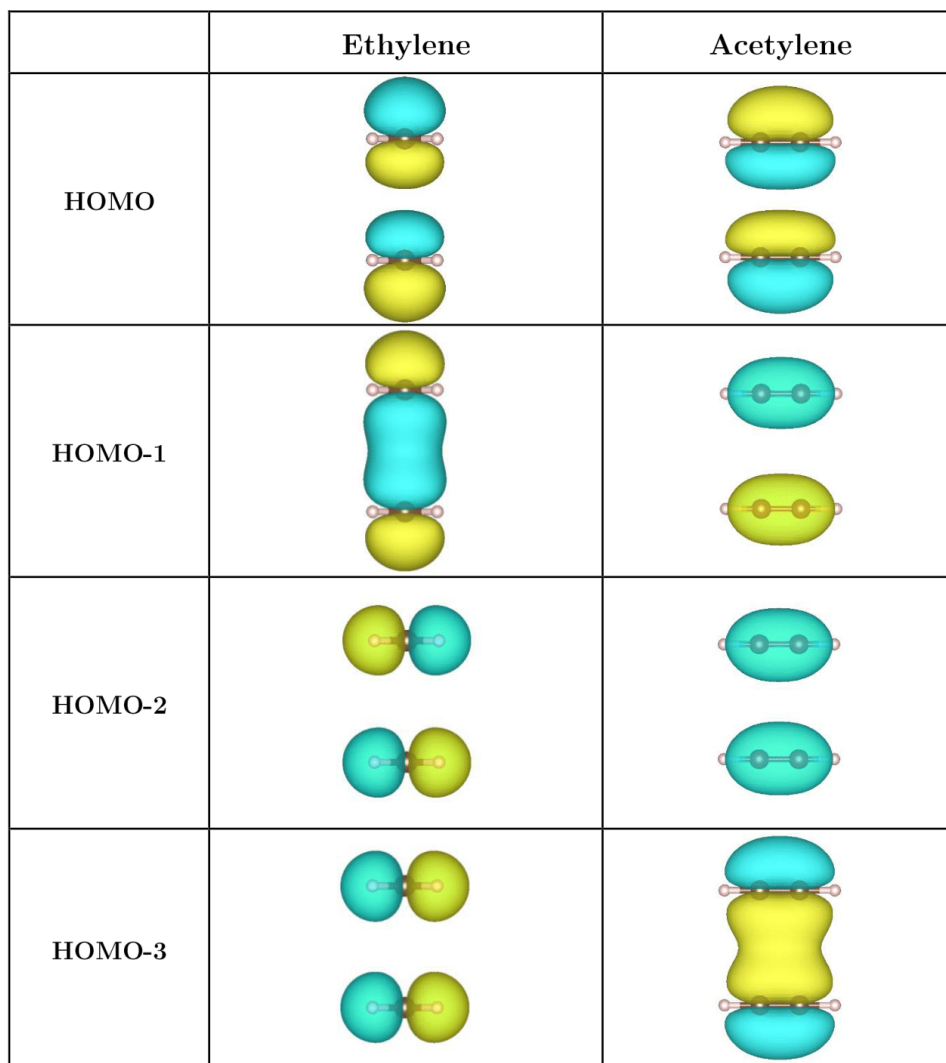
Fig. 5.7: Illustration of DFT calculated molecular orbitals for ethylene and acetylene. The HOMO and further three energetic below lying states are shown for both systems. Owing to theoretical considerations of the Block Decomposition concept, in the case of ethylene the HOMO and HOMO-1 form the two-state system. For acetylene, the HOMO and HOMO-3 belong together.

5.1.2 Rotation: Non-Symmetric Case

In Ch. 5.1.1, the suitability of the Fragment Orbital and Block Decomposition method for symmetric dimers has been shown. Nevertheless, for many systems the assumption of high symmetry does not apply. For such systems, the simple ESD approach does fail, as already shown in Ch. 3.1.1. Therefore, the right estimation of electronic couplings in non-symmetric systems relies on more sophisticated methodologies like Fragment Orbital and Block Decomposition. This chapter shows the validation of both methodologies for the example of ethylene. For that purpose, a symmetric dimer (face-to-face configuration) was constructed, which was then rotated into a non-symmetric system (face-to-edge configuration). A schematic illustration of the rotation is shown in Fig. 5.8. The distance between the molecules was fixed for all configurations at 5 Å.
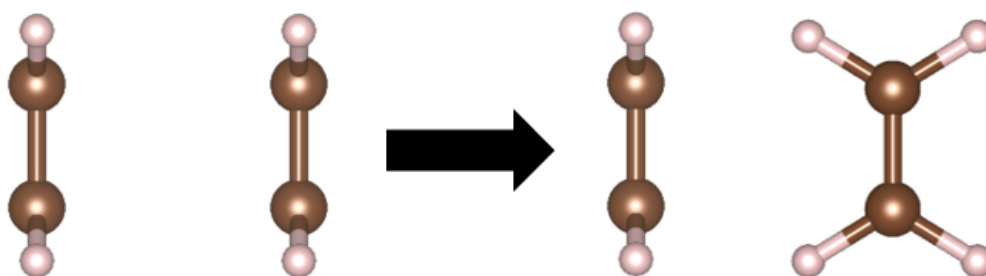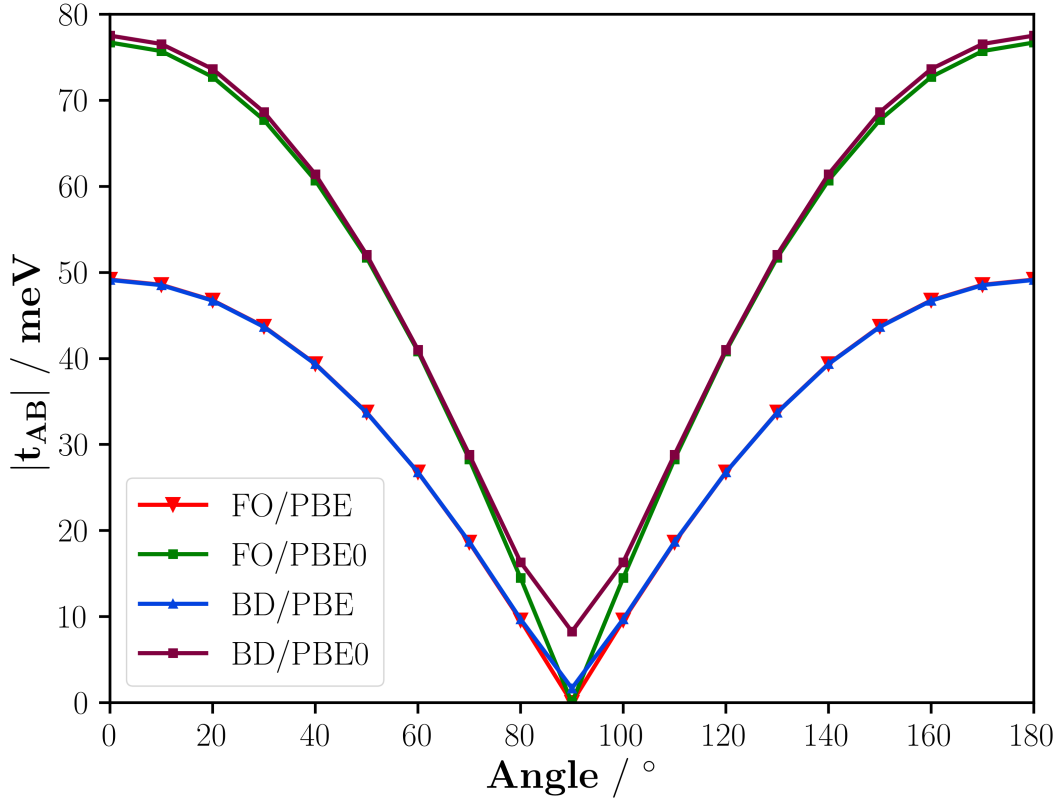

Fig. 5.8: Illustration of an ethylene dimer at two different configurations. On the left side, the symmetric face-to-face configuration is presented. The non-symmetric face-to-edge configuration is shown on the right side.

Furthermore, at various angles, the dimer was calculated with FHI-*aims*, whereby the same settings as explained in Ch. 5.1.1 were used. Also, in this case, the calculations were performed with PBE and the hybrid functional PBE0. From the derived DFT-data, the absolute values of hole couplings were calculated using the implementations of Fragment Orbital and Block Decomposition. The corresponding results are visualized in Fig. 5.9. For the case of PBE, one can see an excellent agreement between both methodologies throughout the entire variety of angles. The hybrid functional PBE0 indicates larger absolute values, whereas the slopes coincide also in this case. Except near the face-to-edge configuration, where the coupling derived with Block Decomposition overestimates the Fragment Orbital result. That issue is still under investigation at the time of writing this thesis.

Fig. 5.9: Ethylene Dimer: Absolute values of hole couplings $|t_{AB}|$ at different configurations. A rotation of one molecule relative to the second one was applied according to Fig 5.8. At zero degrees the system shows a (symmetric) face-to-face configuration, whereas at 90 ° the (non-symmetric) face-to-edge configuration is reached. The couplings were calculated with Fragment Orbital (FO) and Block Decomposition (BD). For both approaches, the PBE and the (hybrid) PBE0 functional in FHI-*aims* were used.

5.1.3 Universal application

The validation of the Fragment Orbital and Block decomposition method showed the suitability of both approaches. Obviously, the next step would be to use those methodologies for the estimation of couplings in bigger systems. Therefore, quinacridone in the α-phase and pentacene were investigated. First, the periodic structures for both systems were optimized using FHI-*aims* [9]. The settings for DFT of this step and for further calculations were equal to the ones in Ch. 5.1.1. Except for an additional definition of an appropriate k-grid. For the relaxation, a k-grid of the dimension $4 \times 4 \times 4$ was chosen. As a next step, the molecule geometries were extracted from the periodic structures. Those structures were then used to construct dimers, according to directions of the periodic lattice. That is relevant for a comparison between cluster-based methods

and the tight-binding approach as shown later in Ch. 6. The DFT-calculations to solve the electronic structures, again with the above-mentioned settings, were performed as a next step. The convergence was tested using different basis sets. As a result, the 2nd-tier, tight settings turned out to be the best choice as basis set based on the relation between computational effort and accuracy. The Fragment Orbital, Block decomposition and Electronic Splitting in Dimers method were then applied to estimate the absolute values of electronic couplings, for the hole and electron case. For the Fragment Orbital method, the HOMOs of the isolated molecules were used to calculate the hole couplings. The electron couplings were derived by using the corresponding LUMOs. The input for the Block decomposition method was the HOMO and HOMO-1 states for the hole case and the LUMO and LUMO+1 for the electron couplings. Further, the whole procedure was repeated with the hybrid functional PBE0 [8], except for the geometry relaxation step.

- Quinacridone α-phase: The absolute values of electronic couplings for the α-phase of quinacridone are shown in Fig. 5.10. The corresponding values of the hole and electron couplings can be found in Tab. 6.1 and Tab. 6.2. The comparison of hole couplings derived with Fragment Orbital (F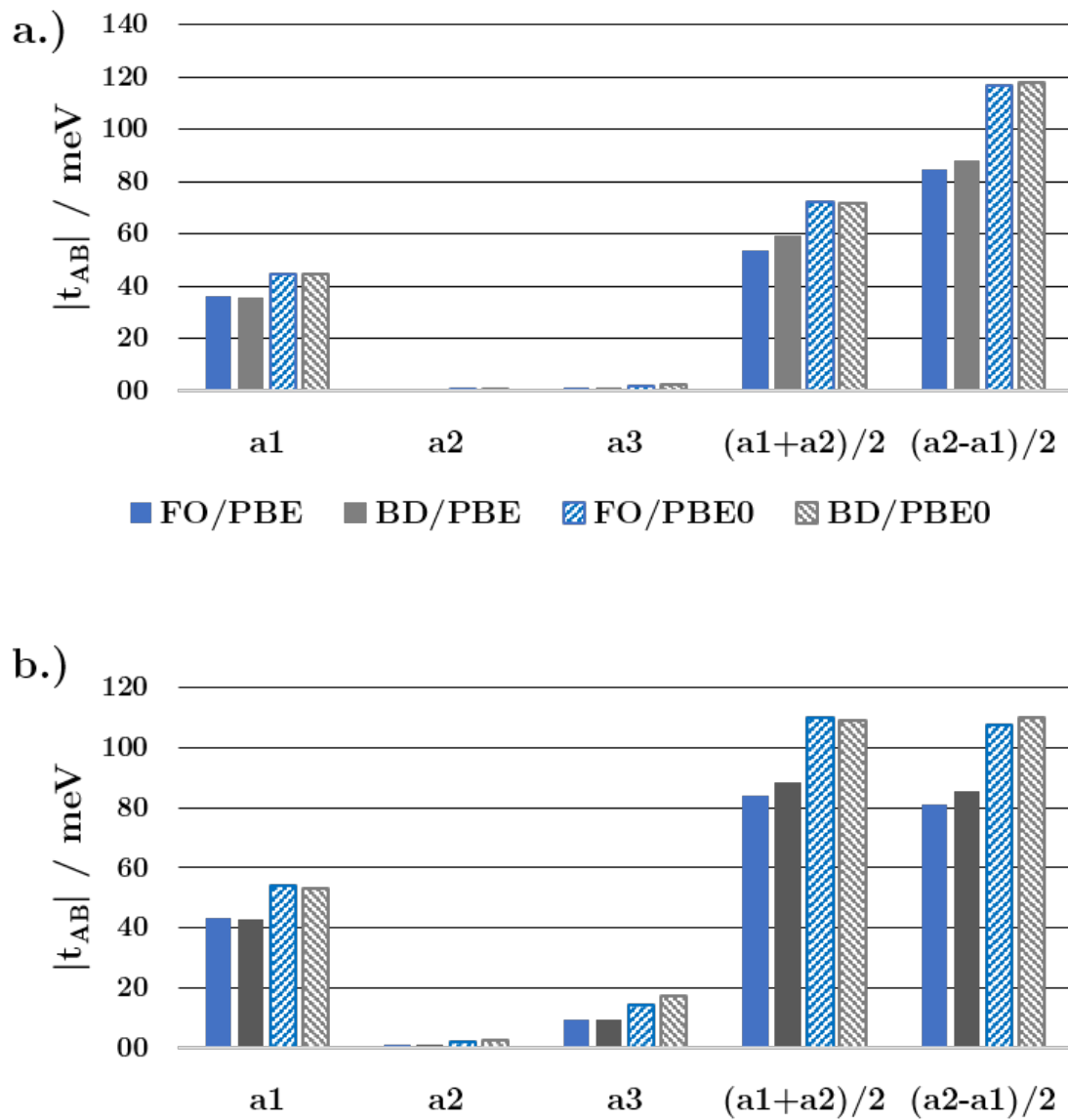O) and Block Decomposition (BD) using the PBE functional results in a good agreement in every direction. The couplings calculated by including Hartree-Fock exchange-energy (HFX) show deviations between FO and BD for certain directions. For example, in $\mathbf{a_2}$, the Fragment Orbital method suggests an increase, whereas Block decomposition shows a decrease of the coupling in comparison to the PBE values. The opposite occurs at the $\mathbf{a_1} + \mathbf{a_2}$ direction, where the Block Decomposition method shows the higher value. Owing to that, it seems that just directions with a contribution of $\mathbf{a_2}$ show this issue. The $\mathbf{a_1} + \mathbf{a_2}$ direction includes hydrogen bondings, whereas the $\mathbf{a_2}$ shows electrostatic interactions. Therefore, the treatment of HFX in those directions turns out to be very critical. As already discussed in Ch. 5.1.1.1, the BD method and the FO approach strongly depend on the amount of HFX. That means the usage of HFX has to be considered well since there is no reference value for the coupling and it could lead to wrong results. Nevertheless, a trend of an increase of the absolute values can be seen for most directions by including HFX in comparison to PBE. The results for the absolute values of electron couplings show a good agreement between FO and BD method, in the case of using the PBE functional. The hybrid calculations with PBE0 are slightly higher in absolute values, except for the $\mathbf{a_1}$ direction. Here, the Fragment Orbital method yields a quite small coupling by using LUMOs of the isolated molecules as a basis.

- Pentacene: The obtained results for electronic couplings in pentacene are visualized in Fig. 5.11. For hole and electron couplings the graph shows a very good agreement between Fragment Orbital and Block Decomposition using the PBE functional. Furthermore, the results obtained by including Hartree-Fock exchange (HFX) coincide between both approaches. The comparison of PBE and PBE0 indicates an increase in the absolute values of the couplings. That is consistent with the observed behaviour in Ch. 5.1.1. Furthermore, the discussed issue of polarization effects on the electronic splitting method (ESD) is visualized in Fig. 5.12.

60

The unit cell of pentacene contains two molecules, which are aligned in a non-symmetric way. The bar plot shows the over-estimation of electronic couplings by using the ESD method at such configurations.
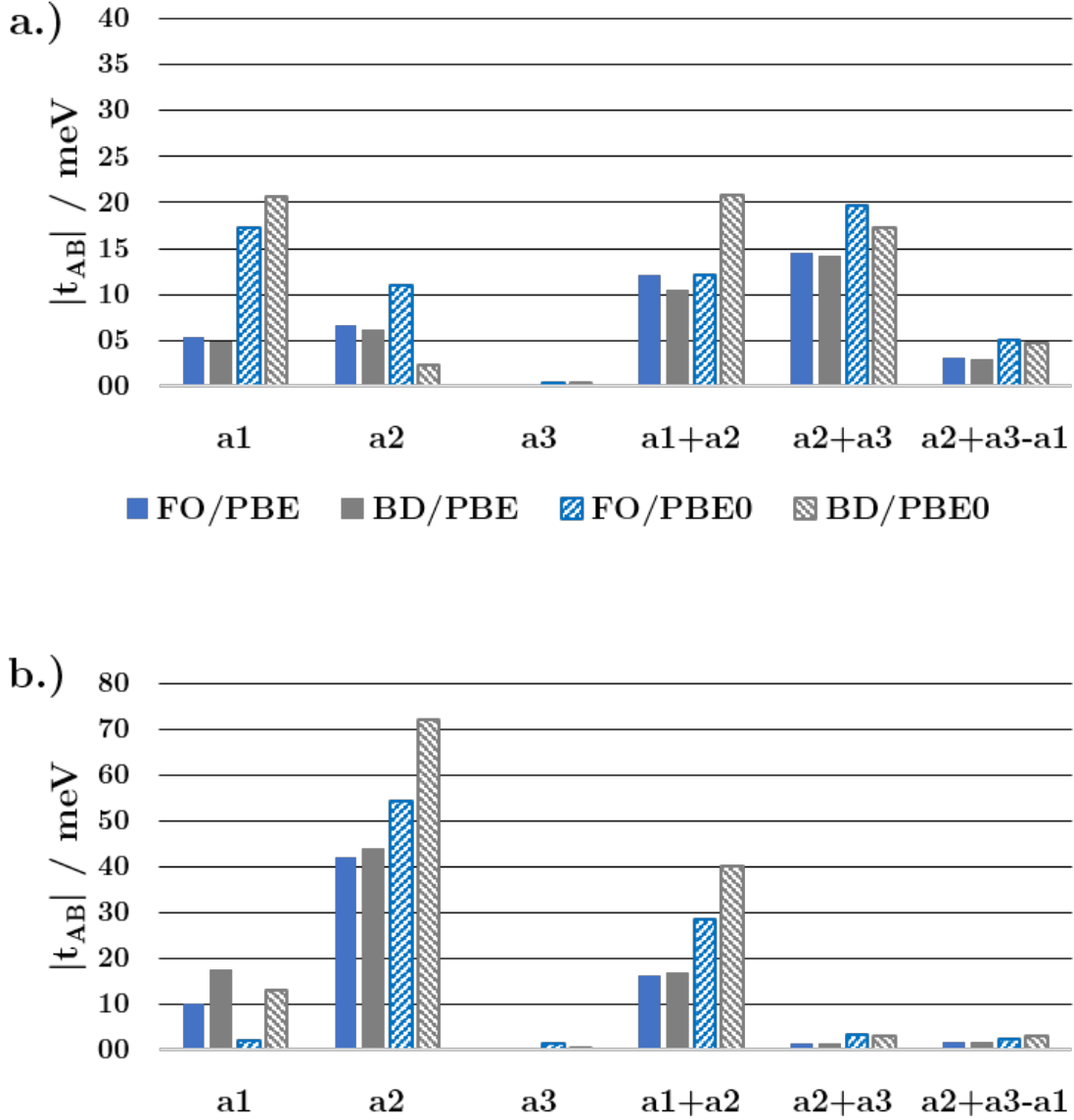
Fig. 5.10: Absolute values of electronic couplings of the quinacridone α-phase estimated with the Fragment Orbital (FO) and Block Decomposition (BD) method. Furthermore, results for PBE and the hybrid functional PBE0 are presented. The diagram shows the hole couplings in the top panel and the electron couplings in the bottom panel. The directions are given by linear combinations of lattice vectors $\mathbf{a_i}$.

Fig. 5.11: Absolute values of electronic couplings of pentacene estimated with the Fragment Orbital (FO) and Block Decomposition (BD) method. Furthermore, results for PBE and the hybrid functional PBE0 are presented. The diagram shows the hole couplings in the top panel and the electron couplings in the bottom panel. The directions are given by linear combinations of lattice vectors $\mathbf{a_i}$.
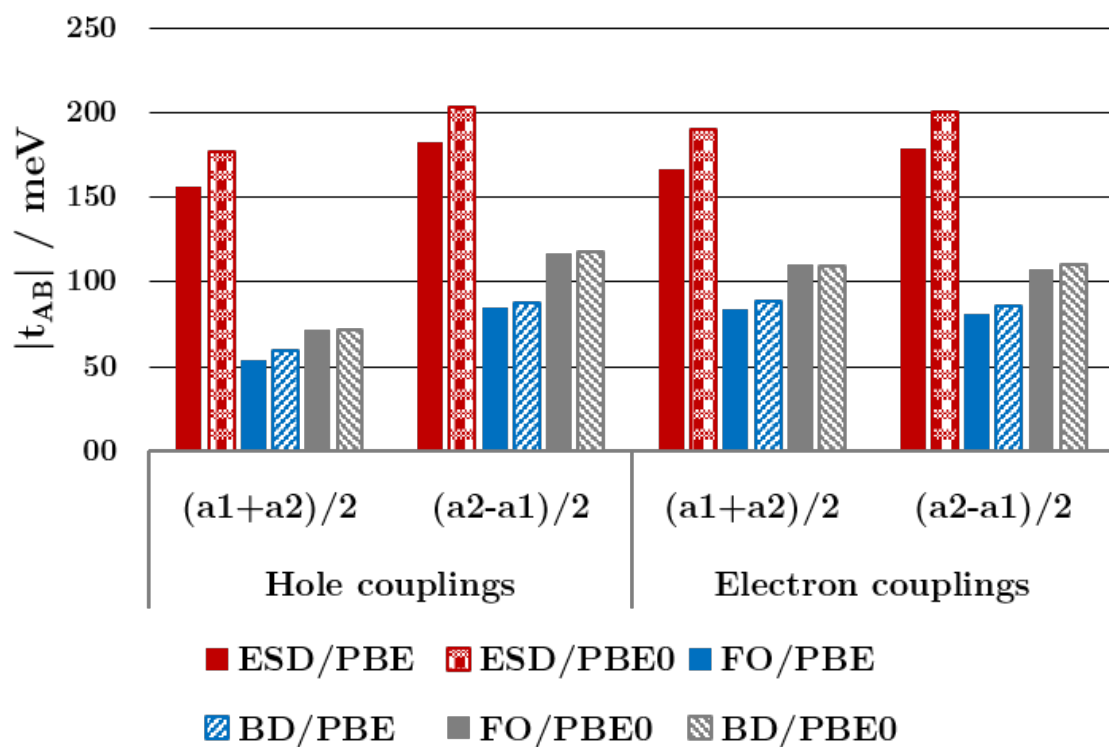
Fig. 5.12: The failure of the Electronic Splitting in Dimers (ESD) method at non-symmetric configurations on the example of pentacene. The latter includes two molecules per unit cell, which are aligned in a non-symmetric manner. The ESD method overestimates the electronic couplings by a factor of two, which follows the discussion of polarization in Ch. 3.1.1.

5.2 Tight-Binding Fits

In this chapter, the application of the tight-binding fit approach for determining electronic couplings is shown. Two different systems, namely the quinacridone α-phase and pentacene, are studied to investigate the suitability of this approach. The corresponding structures have already been discussed in Ch. 4. First of all, the calculations of both systems and the corresponding fits are discussed. The results include the obtained fit parameters (electronic couplings) for the hole and electron case. Furthermore, the estimation of effective masses on the example of quinacridone is presented. Finally, it follows a discussion about the stability and limitations of the fitting procedure. Note that the results shown below are for the purpose of investigating the functionality of tight-binding fits. That means a detailed description of material properties is not the aim within this work. However, many of the results obtained for quinacridone were used in the publication, *C. Winkler, F. Mayer, and E. Zojer. Analyzing the Electronic Coupling in Molecular Crystals-The Instructive Case of α-Quinacridone. Advanced Theory and Simulations, 1800204,2019*, which focusses on material properties.

5.2.1 Results

The procedure to provide dense grids of energy points for fitting suitable functions should be discussed first. Therefore, the calculations started with generating the corresponding geometries (see Ch. 4). As a next step, the geometries were optimized using FHI-*aims* [9]. The main settings for the DFT-calculation are analogous to Ch. 5.1.1. Nevertheless, the treatment of periodic structures requires a few more parameters. The first one is the k-point grid, which has to be chosen right to obtain reliable electronic structures. The convergence tests and the settings for the single point calculations are discussed separately further below since they depend on the system. However, for the purpose of geometry relaxation, it turned out to be sufficient to use a k-grid of $4 \times 4 \times 4$ for both systems. Furthermore, the structures were optimized using the PBE functional. Another parameter for the DFT-calculation would be the k-path, which allows evaluating the electronic structure at certain k-points. Analogously, one is able to evaluate the electronic structure at an uniformly distributed extended k-grid. Note that the electron density used in the DFT-calculation is computed on the original k-grid, not on the chosen k-path or extended grid. Therefore, the original k-grid has to be chosen big enough to justify such a procedure, i.e. convergence must be reached.

5.2.1.1 Quinacridone

For the purpose of fitting a suitable function to the band structure of the quinacridone α-phase, a dense grid of energies has to be evaluated first. Therefore, the optimized structure, as described above, was used to perform an appropriate DFT-calculation. Again, the FHI-*aims* package with main settings already stated in Ch. 5.1.1 was used. As basis set the 2nd-tier, tight settings were used. That is justified by several convergence tests, where deviations in the band structure served as the criterion. As a next step, the convergence of the k-grid was investigated. That means, different grid sizes starting

from $2 \times 2 \times 2$ up to $8 \times 8 \times 8$ were tested. It turned out that a $4 \times 4 \times 4$ k-grid is sufficient to fulfil the convergence criterion of stable band structures. That means a further increase of the k-grid size does not change the bands dramatically (less than 2 meV in high symmetry directions). Nevertheless, the use of such a grid size results in just 64 energy points. That number is not big enough to fit a function. In order to solve this issue, two different strategies were considered. The first one, an increase of the k-grid to obtain more data points. This approach has the disadvantage of high computational costs. The second one, to use the converged electron density and evaluate it at an extended k-grid, as described above. Both approaches were tested, whereby the second one turned out to be the better choice. That is justified by the good agreement in energies of both attempts. Therefore, the energy points for the fit were obtained by using an extended k-grid of $16 \times 16 \times 16$. Additionally, even larger grids were tested but that is not required as discussed in Ch. 5.2.2.1. After finishing the DFT-calculations, the data were used to fit a tight-binding function to it. The quinacridone α-phase contains one molecule per unit cell, which means the model function specified in Eq. (3.69) has to be used. For the neighbours in the tight-binding model, different linear combinations of the lattice vectors $\mathbf{a_i}$ were chosen. The fit was then performed using the implementation discussed in Ch. 3.4.2. This was done for the valence and conduction band. The derived results for the fit parameters are shown in Tab. 5.3. Those values also represent the electronic couplings for the underlying system.

Tab. 5.3: Results for fit parameters of the quinacridone α-phase. The corresponding model function is stated in Eq. (3.69). Vectors...linear combinations of lattice vectors, representing the neighbours in those directions. Valence...fit parameters for the valence band. Conduction...fit parameters for the conduction band. All values given in meV.

Vector	Valence / meV	Conduction /meV
t_{off}	852.67	2462.09
t_{a1}	4.78	-18.39
t_{a2}	-9.73	38.32
t_{a3}	0.40	-0.47
t_{a1+a2}	-9.89	-5.13
t_{a1-a3}	-0.04	-0.04
t_{a2+a3}	-12.15	-1.30
$t_{a1-a2-a3}$	-5.19	-1.03
t_{2a1+a2}	-0.11	-0.39
t_{2a1-a3}	-0.03	0.09
t_{2a1}	2.00	-13.17
$t_{a1+a2+a3}$	3.26	-0.93
t_{a1-a2}	-0.62	1.28
t_{2a2}	0.45	0.02
t_{3a1}	1.45	-0.43

The fit was performed using the Levenberg-Marquardt [38,39] algorithm. For the sake of comparison, other algorithms like Powell [40], Conjugate-Gradient [41] and Nelder-Mead [42] were tested too. All of them were able to reproduce the same results, which approves consistency. The statistical characterization of the fits are shown in Tab. 5.4. The root mean squared error shows a maximal value of about 3 meV for the valence band. That result satisfies the requirements for an accurate estimation of electronic couplings.

Tab. 5.4: Quinacridone α-phase: Statistical values characterizing the quality of the tight-binding fit. VB...valence band, CB...conduction band, DG points... number of points in dense grid, $(R)MSE$... (root) mean squared error of fit, HS points... number of high symmetry points, $(R)MSE_{HS}$...(root) mean squared error evaluated at high symmetry k-path

	VB	CB
DG points	4096	4096
MSE / eV	0.0479	0.0135
RMSE / eV	0.0031	0.0016
HS points	350	350
MSE$_{HS}$ / eV	0.0019	0.0004
RMSE$_{HS}$ / eV	0.0023	0.0010

Furthermore, an optical validation of the obtained fit was performed. That means the band structure was computed with DFT in high symmetry directions. The same k-path was then used to evaluate the tight-binding function at those points. The corresponding result is shown in Fig. 5.13. The optical agreement indicates that the tight-binding function reproduces the electronic structure.
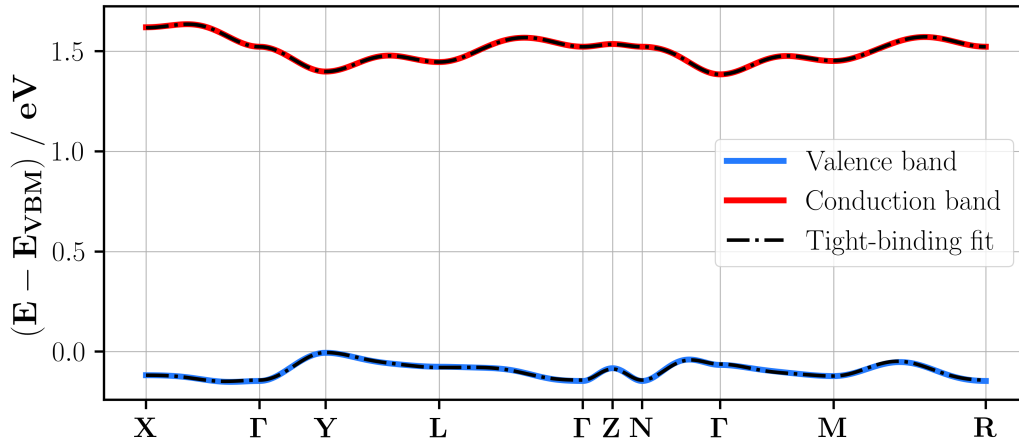
Fig. 5.13: Quinacridone α-phase: Electronic band structure along high symmetry directions. The graph shows the valence and conduction band derived with DFT. The dashed lines represent the corresponding tight-binding fits. In this case, the fit was performed using the one molecule per unit cell approach.

Nevertheless, to be more accurate, an enlarged graph of the valence band is shown in Fig. 5.14. In this plot, one can see small deviations in certain areas. However, the

root mean squared error (see Tab. 5.4) with respect to high symmetry points turns out to be in the region of 1 meV. Due to that, one can conclude that the tight-binding fit accurately reproduces the band structure for the case of the quinacridone α-phase. Furthermore, the number of fit parameters could be increased to enhance the agreement, but that is not necessary to obtain correct electronic couplings. The latter is justified by the stability of the fit, as shown in Ch. 5.2.2.1.
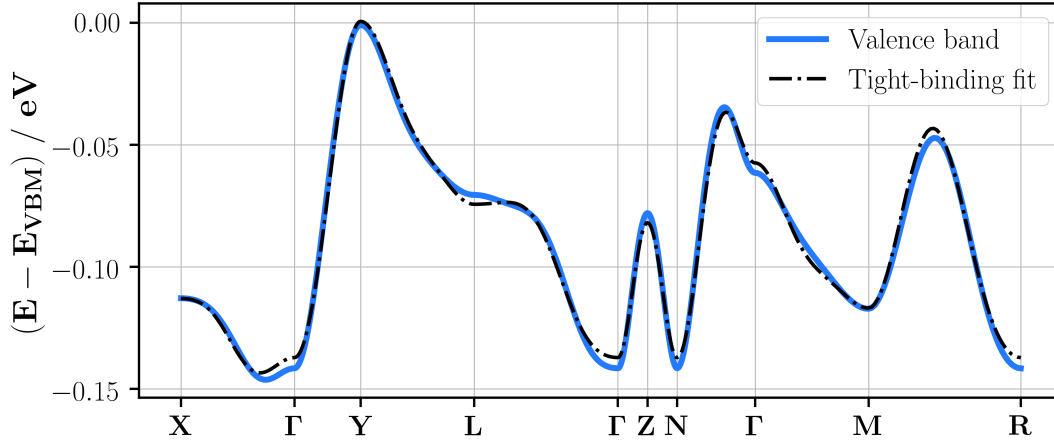
Fig. 5.14: Detailed illustration of the valence band of the quinacridone α-phase. The graph shows the valence band derived with DFT and the corresponding tight-binding fit.

The derived tight-binding function allows analysing the band structure in different ways. For example, one can take a look at the high-symmetry direction Γ-X of the conduction band (see Fig. 5.13), which processes parallel to the real space vector $\mathbf{a_1}$. There is a peak near the middle, which indicates deviations from a cosine shape of the band. From this, the question of how this can be understood arises. For the investigation, one can use the in Ch. 3.4.2 explained analysis tool. The latter makes it possible to decompose the bands in certain directions. An example for the above mentioned direction is illustrated in Fig. 5.15. It turns out that the band in the Γ-X direction has two main contributions. First, the electronic coupling in $\mathbf{a_1}$, which gives a cosine shape to the band. Secondly, there is a contribution from the next nearest neighbour in $\mathbf{2 \cdot a_1}$. The corresponding coupling shows a doubled frequency and is responsible for the peak in the middle of the band. A physical interpretation and more on this topic can be found in our publication [56].

The knowledge of an analytical function for the valence and conduction band brings several advantages. As already shown, by fitting this function the electronic couplings are estimated. Further, a decomposition of bands is possible due to the nature of the model function. Another advantage is that the effective mass (as the most important parameter for band transport) can be determined in a straightforward manner at the desired k-points. Note that for accurate effective masses the agreement between tight-binding

68
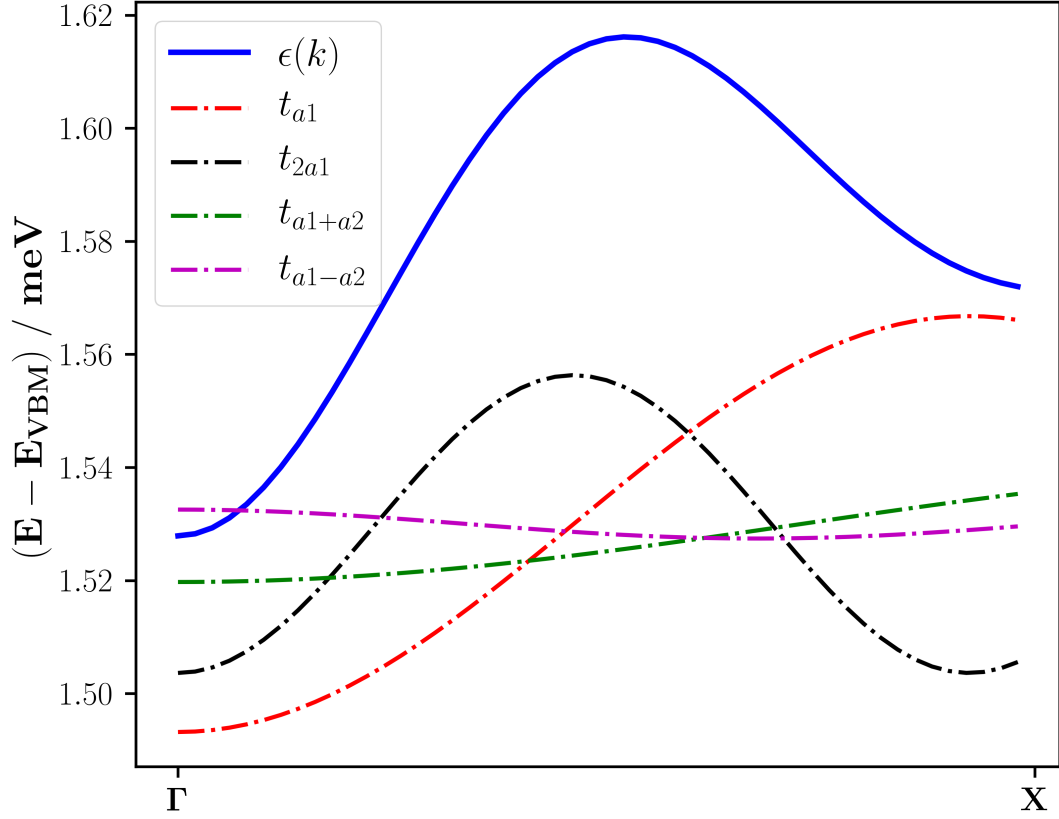
Fig. 5.15: Conduction band of the quinacridone α-phase in the Γ-X direction. This direction is parallel to the real-space vector $\mathbf{a_1}$. The graph shows the entire tight-binding function $\epsilon(\mathbf{k})$ at this direction. Furthermore, the contributions of couplings in $\mathbf{a_1}$, $\mathbf{2 \cdot a_1}$, $\mathbf{a_1 + a_2}$ and $\mathbf{a_1 - a_2}$ to $\epsilon(\mathbf{k})$ are shown.

function and DFT-data is crucial. Due to that, it might be advantageous to increase the number of fit parameters. For the quinacridone α-phase, the above-shown fitted function, however, satisfies these requirements. For hole transport, the maximum of the valence band is of great interest. Analogously, the conduction band minimum presents the point to study for electron transport. For the quinacridone α-phase, the valence band minimum (VBM) is found at reciprocal point X, whereas the conduction band minima is at Y. The implementation, shown in Ch. 3.4.2, was used to calculate the effective mass tensor at those points. However, to present the results more descriptive, the tensor was multiplied from both sides with direction vectors $\mathbf{d}$. The corresponding mathematical expression is stated in Eq. (5.1). That leads to scalar values for the effective mass, which describe the motion of charge in direction $\mathbf{d}$, when an external field is applied in the same direction. The visualization of the obtained results as 3D-plots is shown in

Fig. 5.16. The plot shows effective masses for the valence and conduction band at their respective extrema. In the following section, a short interpretation of results derived for band and hopping transport is given. For further details, see our publication [56].

$$[m_{\mathbf{d}}^*]^{-1} = \mathbf{d}^T \left(\frac{\partial^2 \epsilon(\mathbf{k})}{\partial k_i \partial k_j} \right) \mathbf{d} \tag{5.1}$$

The effective mass for the valence band shows rather small values for the directions $\mathbf{a_3}$, $\mathbf{a_2} + \mathbf{a_3}$ and $\mathbf{a_2}$. That indicates preferable good transport for holes in those directions.
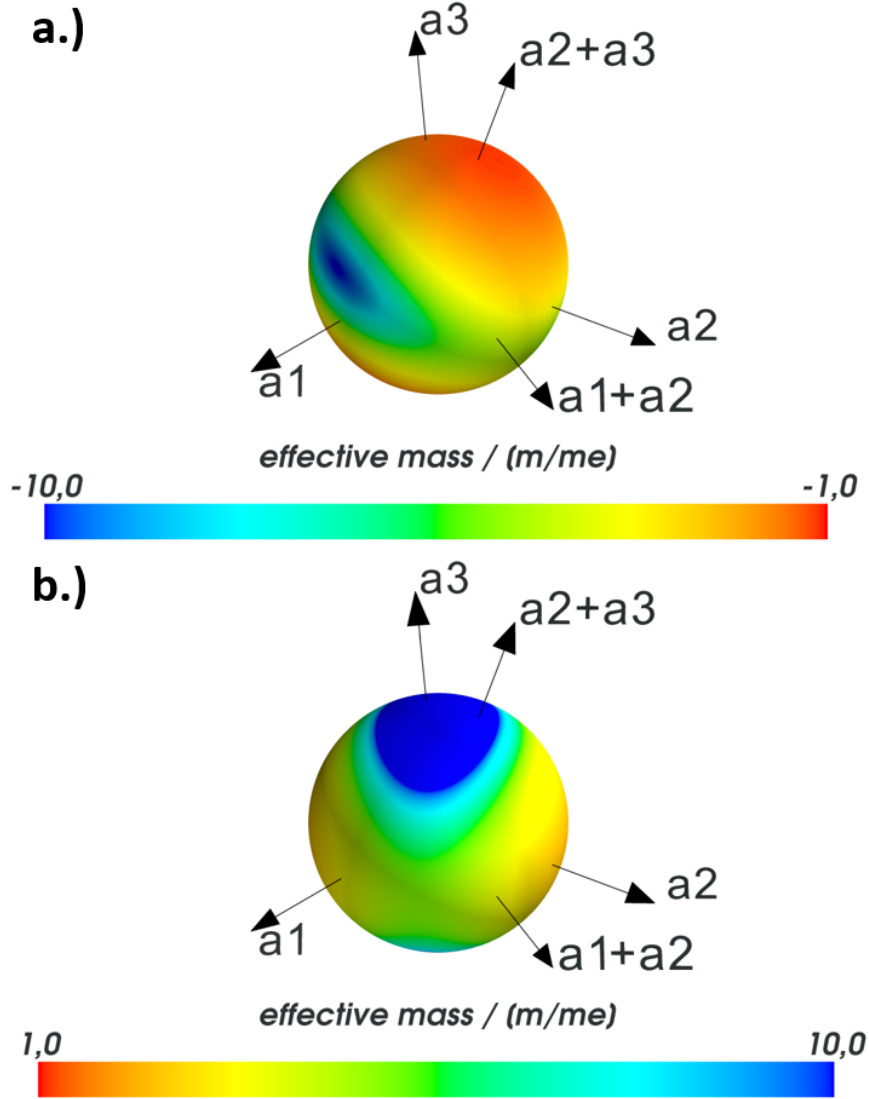
Fig. 5.16: Effective mass of the quinacridone α-phase illustrated by a 3D-sphere plot. The sphere is coloured according to values of the effective mass in every direction. a.) shows the effective mass at the valence band maximum, which is found at X. b.) the effective mass at the conduction band minima, which is at Y.

For the case of hopping transport, the respective hole couplings (see Tab. 5.3) are decisive. The values of the couplings in $\mathbf{a_2} + \mathbf{a_3}$ and $\mathbf{a_2}$ show consistently the same behaviour as for band transport. However, the coupling in $\mathbf{a_3}$ is rather low, which indicates that hopping rates in this direction will be lower too. Owing to that, it seems that a difference between band and hopping transport behaviour occurs. The explanation can be found in the structure of the energy dispersion in this direction. The energy slope $\epsilon(\mathbf{k})$ is given by the sum of couplings weighted with their corresponding phase factors. As already mentioned, the coupling in $\mathbf{a_3}$ is rather low, but there are other contributions which increase the dispersion. For the present case this would be the coupling in $\mathbf{a_2} + \mathbf{a_3}$ and $\mathbf{a_1} - \mathbf{a_2} - \mathbf{a_3}$. That shows the importance of a detailed investigation of the band structure to accomplish an accurate description of transport phenomena.

5.2.1.2 Pentacene

For the purpose of testing the suitability of model functions describing two molecules per unit cell, results on pentacene are shown. As mentioned at the beginning of this chapter, the geometry was optimized by using FHI-*aims*. The estimation of the electronic structure started with several convergence tests. First, the basis set was converged to accomplish accurate results for the valence and conduction band. That means, different basis set sizes were tested, whereby deviations in the band structure were measured. The 2nd-tier, tight settings turned out to be sufficient to obtain a converged band structure. The use of more basis functions yields a massive increase in computational time, which was not justified by the minor increase of accuracy for the present purpose. As a next step, the convergence of the k-grid was investigated. Different grid sizes starting from $2 \times 2 \times 2$ up to $8 \times 8 \times 8$ were set in the DFT-calculation. As convergence criterion, again, deviations in the valence and conduction band energies were measured. As a result, the $4 \times 4 \times 4$ k-grid turned out to fulfil the requirement of a change less than 1 meV in high symmetry directions of those bands. With those settings, the single point calculation was performed. As already discussed for quinacridone, the use of an extended grid allows estimating a higher number of k-points. Therefore, an extended grid of $16 \times 16 \times 16$ was chosen to evaluate 4096 energy points. The latter provides a dense enough grid to fit a suitable function. For the present case of two molecules per unit cell, the corresponding model function discussed in Ch. 3.4 has to be used. Due to the fact that the couplings in symmetric directions A-A and B-B turned out to be almost (less than 2 meV) the same, the function was modified by assuming $H_{AA}(\mathbf{k}) = H_{BB}(\mathbf{k}) - t_{off}^{BB}$. The additional fit parameter t_{off}^{BB} describes the on-site energy of molecule B. This is justified by the structure of the unit cell, which indicates that the offsets (on-site energies) of both molecules are not equal. Note that in the present case, the model function is fitted to two energy bands. That would be either the VB (valence band) and VB-1 or the CB (conduction band) and CB+1. The fitting was performed using the implementation explained in Ch. 3.4.2. For the sake of fitting the model function, different algorithms were tested to check for reproducibility of the obtained results. That included the Levenberg-Marquardt [38, 39], Powell [40], Conjugate-Gradient [41] and Nelder-Mead [42] algorithm. All of them yielded the same global minima by fitting
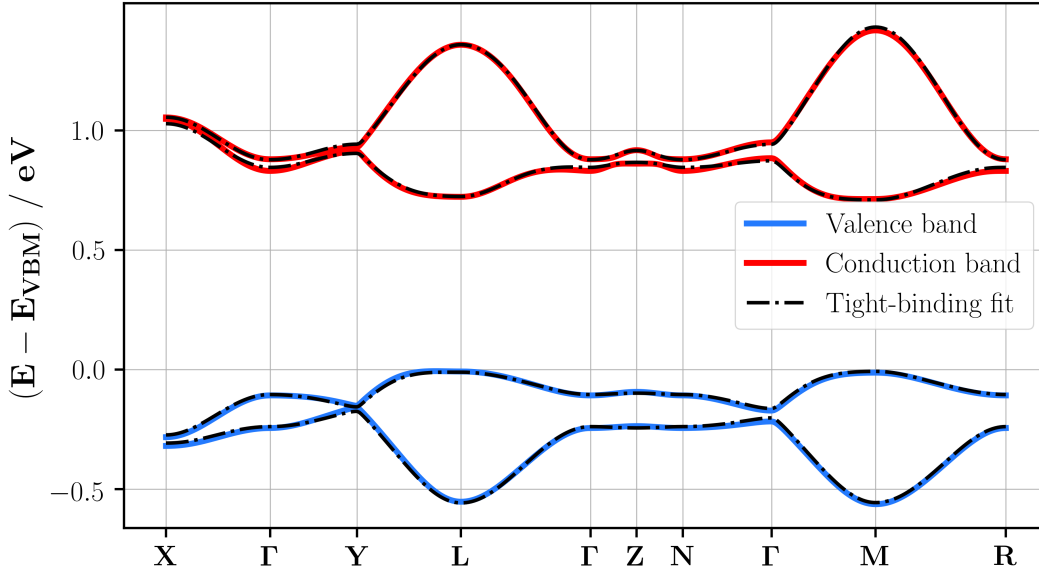
Fig. 5.17: Pentacene: Electronic band structure in high symmetry directions. The graph shows the valence and conduction band derived with DFT. The dashed lines represent the corresponding tight-binding fits. In the present case, the fit was performed using the two molecules per unit cell approach, see Ch. 3.4.

the same parameters, which indicates consistency. The band structure derived with DFT and the corresponding fits evaluated in high symmetry directions are given in Fig. 5.17. The graph shows a good optical agreement between analytical function and DFT-data, i.e. for the valence and conduction band. The corresponding statistical values characterizing the fits are presented in Tab. 5.7. The root mean squared error justifies the obtained results for the purpose of extracting electronic couplings. The results for fit parameters using the Levenberg-Marquardt algorithm are shown in Tab. 5.5 and Tab. 5.6. The former presents the couplings between molecules of the same type. The second table includes couplings between molecules of type A and B. In these tables, the neighbours can be found by the following rule. For example, the coupling from molecule A in the zeroth unit cell to molecule B, which is localized in a unit cell shifted by a vector $\mathbf{a_x}$, is given by the notation $t^{AB}_{|\mathbf{a_x}|}$. An illustration of important fit parameters and their appearance in the lattice can be found in Fig. 5.18.
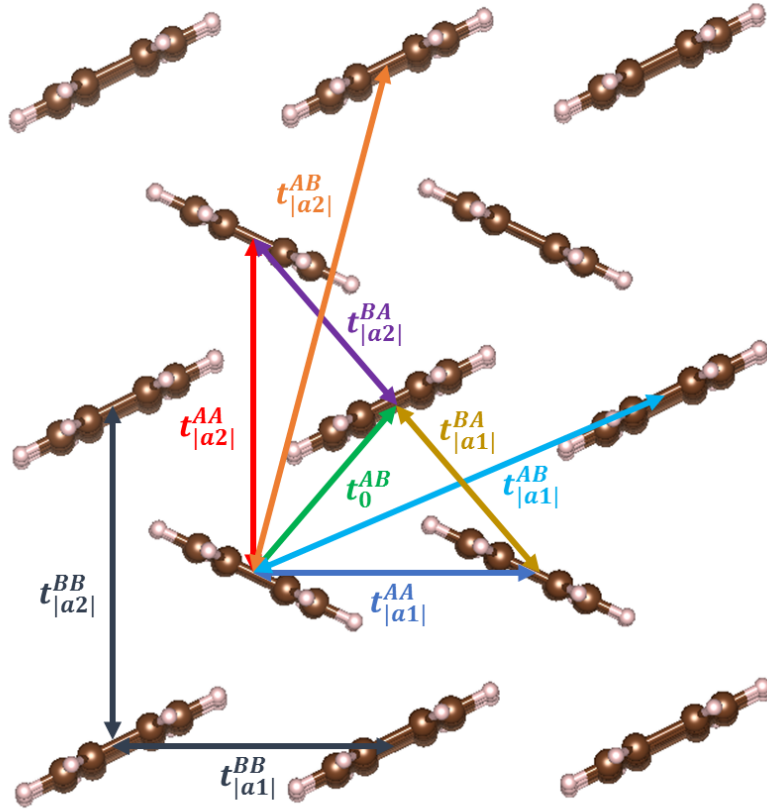
Fig. 5.18: Pentacene: Illustration of important fit parameters and their respective directions. The corresponding values derived by fitting an analytical function to the band structure can be found in Tab. 5.5 and Tab. 5.6. Due to the shape of the periodic structure, the assumptions of $t^{BB}_{|a2|} = t^{AA}_{|a2|}$ and $t^{BB}_{|a1|} = t^{AA}_{|a1|}$ are used in the fit.

With the knowledge of those couplings, it is possible to screen for preferable hopping transport directions. For hole transport, the couplings belonging to the valence band are of interest. For example, the coupling in $\mathbf{a_1}$ direction indicates preferable hopping in that direction. In contrast, the $\mathbf{a_2}$ direction shows an almost vanishing coupling, which implies rather low transfer rates. However, the values for directions $(\mathbf{a_1} + \mathbf{a_2})/2$ and $(\mathbf{a_1} - \mathbf{a_2})/2$ indicate even better hopping rates. Analogously, the behaviour of electrons can be studied. In this case, the corresponding conduction band couplings are relevant. Notably, there are also some problems, when employing the fitting method. First, the stability of the two molecules per unit cell approach, which is discussed in detail in Ch. 5.2.2.2. Further, for two molecules per unit cell, crossings in the band structure can occur, that issue is investigated in Ch. 5.2.3.

Tab. 5.5: Pentacene: Fit parameters between molecules of the same type, i.e. A-A and B-B. The results were derived using the model function describing two molecules per unit cell, see Eq. (3.74). Vector...linear combinations of lattice vectors, identifying the neighbours. Valence...represents the fit parameters of the valence band (VB) and VB-1. Conduction...represents the fit parameters of the conduction band (CB) and CB+1. All values given in meV.

Vector	Valence / meV	Conduction / meV
t_{off}^{AA}	-6862.11	-5648.19
t_{off}^{BB}	-6856.33	-5671.94
$t_{\|a1\|}^{AA}$	29.40	-37.24
$t_{\|a2\|}^{AA}$	-1.86	-7.28
$t_{\|a1+a2\|}^{AA}$	2.09	-2.05
$t_{\|a3\|}^{AA}$	1.78	-1.70
$t_{\|a1+a3\|}^{AA}$	0.34	-0.03
$t_{\|a2+a3\|}^{AA}$	-0.04	0.02
$t_{\|a1+a2+a3\|}^{AA}$	0.02	-0.03
$t_{\|2a1\|}^{AA}$	-0.99	0.33
$t_{\|2a2\|}^{AA}$	-0.08	0.05
$t_{\|2a3\|}^{AA}$	0.00	0.00
$t_{\|2a1-a2\|}^{AA}$	0.38	-0.42
$t_{\|a1+a2+a3\|}^{AA}$	-2.12	-5.70

Tab. 5.6: Pentacene: Fit parameters between the different types of molecules A-B and B-A. The results were derived using the model function describing two molecules per unit cell (see Eq. (3.74)). Vector...linear combinations of lattice vectors identifying the neighbours. Valence...fit parameters of the valence band (VB) and VB-1. Conduction...fit parameters of the conduction band (CB) and CB+1. All values given in meV.

Vector	Valence / meV	Conduction / meV
$t_{\mathbf{off}}^{\mathbf{AB}}$	46.32	79.58
$t_{\mathbf{|a1|}}^{\mathbf{AB}}$	-0.60	-86.59
$t_{\mathbf{|a1|}}^{\mathbf{BA}}$	-84.70	2.48
$t_{\mathbf{|a2|}}^{\mathbf{AB}}$	0.89	-80.92
$t_{\mathbf{|a2|}}^{\mathbf{BA}}$	-86.54	-0.14
$t_{\mathbf{|a1+a2|}}^{\mathbf{AB}}$	0.81	92.18
$t_{\mathbf{|a1+a2|}}^{\mathbf{BA}}$	57.94	0.54
$t_{\mathbf{|a3|}}^{\mathbf{AB}}$	0.04	-3.87
$t_{\mathbf{|a3|}}^{\mathbf{BA}}$	1.83	-0.26
$t_{\mathbf{|a1+a3|}}^{\mathbf{AB}}$	0.06	3.94
$t_{\mathbf{|a1+a3|}}^{\mathbf{BA}}$	2.12	0.05
$t_{\mathbf{|a2+a3|}}^{\mathbf{AB}}$	-0.05	-0.01
$t_{\mathbf{|a2+a3|}}^{\mathbf{BA}}$	-0.47	0.02
$t_{\mathbf{|a1+a2+a3|}}^{\mathbf{AB}}$	-0.03	0.41
$t_{\mathbf{|a1+a2+a3|}}^{\mathbf{BA}}$	0.47	-0.01
$t_{\mathbf{|2a1|}}^{\mathbf{AB}}$	0.18	-1.89
$t_{\mathbf{|2a1|}}^{\mathbf{BA}}$	-2.39	0.03
$t_{\mathbf{|2a2|}}^{\mathbf{AB}}$	0.03	-0.55
$t_{\mathbf{|2a2|}}^{\mathbf{BA}}$	-0.84	-0.15
$t_{\mathbf{|2a3|}}^{\mathbf{AB}}$	0.01	0.11
$t_{\mathbf{|2a3|}}^{\mathbf{BA}}$	-0.02	0.14
$t_{\mathbf{|2a1-a2|}}^{\mathbf{AB}}$	-0.20	-0.79
$t_{\mathbf{|2a1-a2|}}^{\mathbf{BA}}$	-0.73	-0.17
$t_{\mathbf{|a1+a2+a3|}}^{\mathbf{AB}}$	-0.29	-13.07
$t_{\mathbf{|a1+a2+a3|}}^{\mathbf{BA}}$	-0.85	-0.59

Tab. 5.7: Pentacene: Statistical values characterizing the quality of the tight-binding fit. VB...valence band, CB...conduction band, DG points...number of points in dense grid, $(R)MSE$... (root) mean squared error of fit, HS points... number of high symmetry points, $(R)MSE_{HS}$...(root) mean squared error evaluated at high symmetry k-path

	VB	CB
DG points	8192	8192
MSE / eV	0.3649	0.2312
RMSE / eV	0.0067	0.0053
HS points	300	300
MSE$_{HS}$ / eV	0.0102	0,0054
RMSE$_{HS}$ / eV	0.0058	0.0042

5.2.2 Stability of Tight-Binding Fits

The present chapter is about the stability of fitting tight-binding functions. It is divided into two parts. As a first part, the stability of the model function describing one molecule per unit cell is studied. For this purpose, a simple 1D-example is shown to demonstrate stability by varying different parameters. The second part includes the two molecules per unit cell approach and its corresponding behaviour.

5.2.2.1 One Molecule per Unit Cell

The model function for one molecule per unit cell is stated in Eq. (3.69) in Ch. 3.4. The mathematical structure of this function can be identified as a Fourier series. For the sake of illustrating the stability of fitting this function to data, an example of a 1D-series is discussed. For this purpose, the model function stated in Eq. (5.2) representing a 1D-Fourier series, is used. The fit parameters are represented by the t_n, while the phase factor is given by the cosine. The cosine functions can be used if there is an inversion symmetry. The periodicity of this function is given by the parameter a in real space and $\frac{2\pi}{a}$ in reciprocal space. However, to demonstrate stability, the function is fitted to a rectangular curve of points. The point density is adjustable as shown further below.

$$E(k) = \sum_n t_n cos(nka) \tag{5.2}$$

The first test was performed to demonstrate the improvement of the model function with respect to the rectangular shape when increasing the number of fit parameters. The corresponding graph is shown in Fig. 5.19. The illustration shows single contributions to the model function on the left side, while on the right side the entire model function is presented. As expected, the increase of fit parameters yields a better reproduction of

the rectangular shape. Furthermore, the evolution of fit parameters and their respective values was investigated. For that purpose, the number of parameters was steadily increased to observe possible changes in their values. The obtained results are visualized in Fig. 5.20. The graph starts with one fit parameter used to fit the rectangular shaped curve. Then, a second parameter was added and so forth. It can be seen that the values of the fit parameters are constant, which implies they are not influenced by the presence of other parameters. This behaviour was also observed for the 3D tight-binding model function for the example of the quinacridone α-phase [56]. Another aspect would be the density of points of the rectangular shape, which are used in the fit. For the above-shown results, the number of points was set to 4000. However, one can vary this number to show the evolution of the absolute error of the fit parameters. The reference values for the fit parameters to obtain the absolute errors were taken from a fit to 4000 points. An example of fitting the rectangular shape by increasing the point density is illustrated in Fig. 5.21. As a result, one can see that the absolute error decreases by increasing the density of points. Nevertheless, also with a small number of points, the absolute error is rather small. For a real application of the tight-binding fitting method, the number of necessary energy points was tested analogously for the quinacridone α-phase. It turned out to be sufficient to calculate about 200 points in the 1st-Brillouin zone to guarantee the reproduction of the band structure. However, an individual test of convergence is recommended for employing the fitting method to a specific system.

5.2.2.2 Two Molecules per Unit Cell

In the present chapter, the stability of the model function for two molecules per unit cell is discussed. The corresponding model function is given in Eq. (3.74) in Ch. 3.4. For the sake of testing the stability, the situation for pentacene was investigated. The first attempt included the repetition of the fitting procedure, whereby the number of fit parameters was held constant. Furthermore, the initial values of the fit parameters were generated randomly. That means, the fit was performed several times on the same data with the same number of parameters. The graph in Fig. 5.22 shows the corresponding results, whereby the assumption of $H_{AA}(\mathbf{k}) = H_{BB}(\mathbf{k})$ was made. The fit parameters for couplings between molecules of the same type, e.g. $H_{AA}(\mathbf{k})$, are stable. This can be related to the behaviour of the one molecule per unit cell approach (discussed in the prior chapter). However, the fit parameters describing couplings between two different types of molecules A, B indicate some kind of inconsistency. For the meaning of those parameters see Fig. 5.18. In Fig. 5.22, one can see that by repeating the same fitting procedure, some values change at a certain point. For the present attempt, the $t_{|a1|}^{AB}$ and $t_{|a1|}^{BA}$ swap their value. Further, the parameters $t_{|a2|}^{AB}$ and $t_{|a2|}^{BA}$ show the same behaviour. It seems that the fit is not stable, but there is a simple explanation for this issue. The $t_{|a1|}^{AB}$ and $t_{|a1|}^{BA}$ parameters have the same phase factor, which implies a degree of freedom in the fit. For example, there is no restriction that $t_{|a1|}^{AB}$ describes always the coupling to the next nearest neighbour (see Fig. 5.18). Therefore, one has to figure out which parameter describes the nearest neighbour coupling or the next nearest neighbour one. In most cases, the larger value can be identified with the nearest neighbour, but a chance
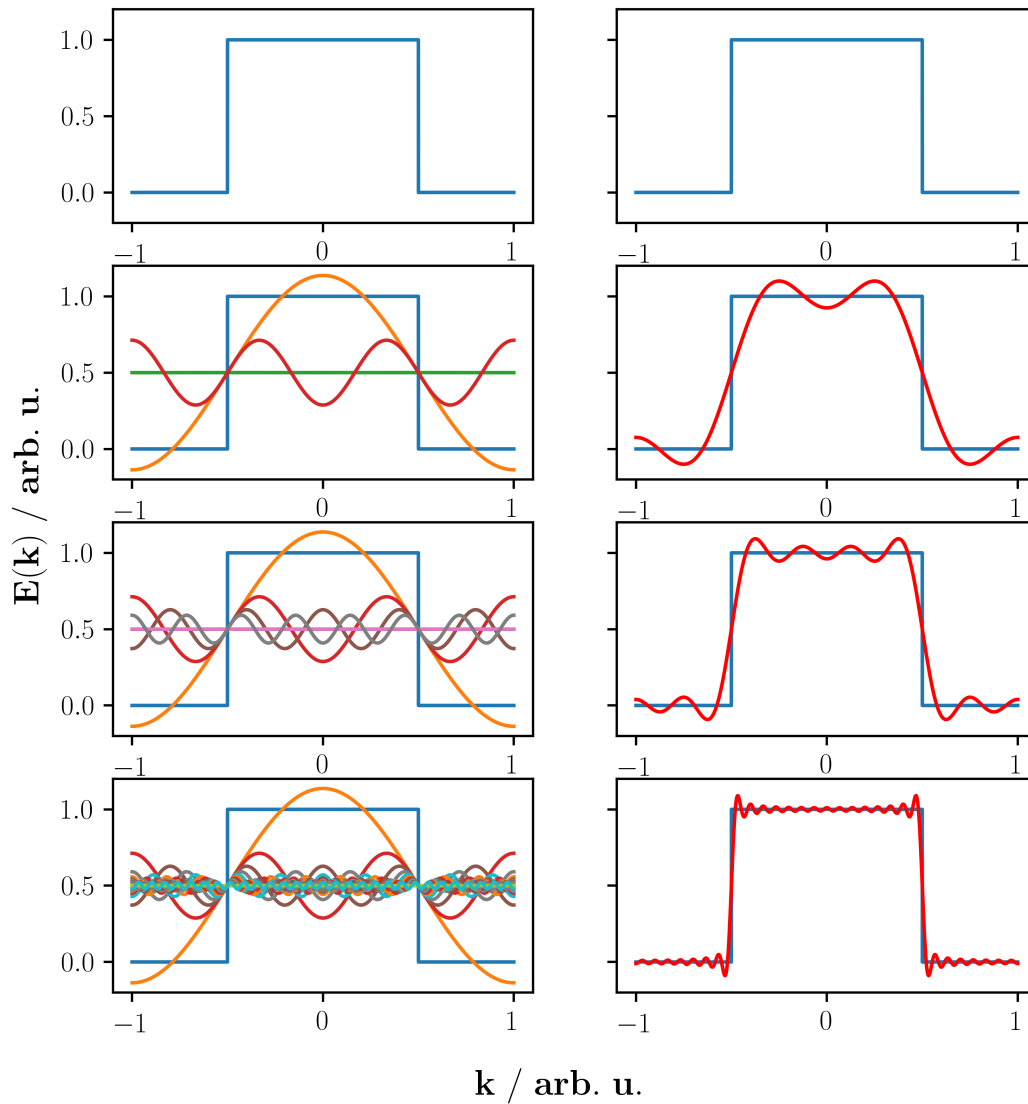
Fig. 5.19: The illustrative case of a 1D-Fourier series used to fit a rectangular function. The rectangular curve consisting of 4000 individual data points is represented by the blue line. The left side shows contributions to the Fourier series, which are cosines with different periodicities of na. The number of used parameters is increased from the top to the bottom. On the right side, the sum of those contributions forming the Fourier series (red line) is shown.

78
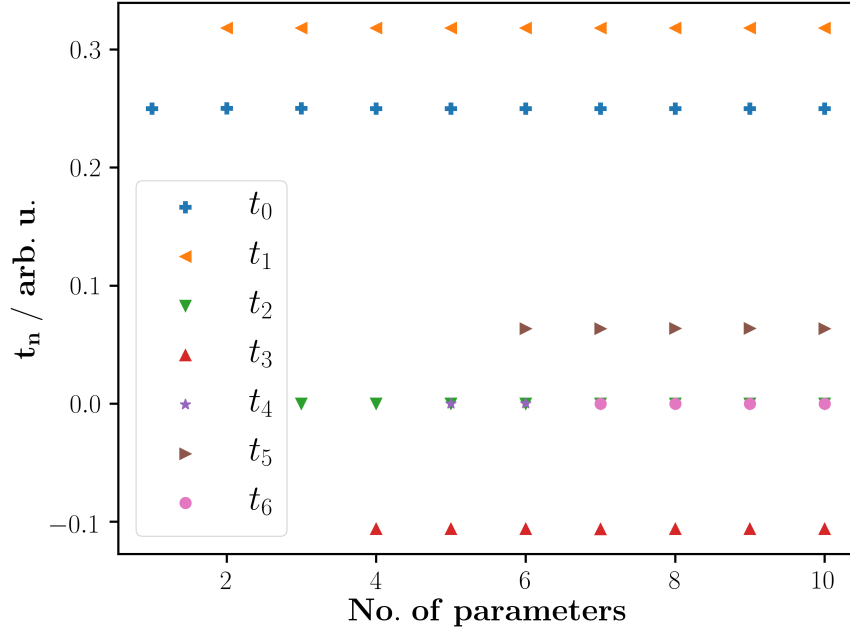
Fig. 5.20: Evolution of obtained values for the fit parameters t_n upon increasing the total number of parameters. The index n represents the periodicity of $cos(nka)$. The graph starts on the left side with one parameter used to fit the rectangular shaped curve. Then, the number of parameters was increased steadily.
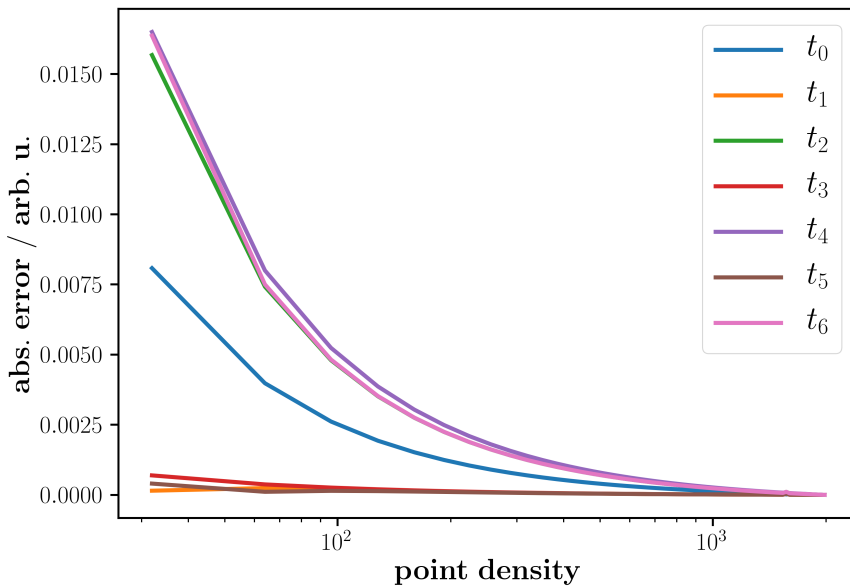
Fig. 5.21: Evolution of absolute error of fit parameters by increasing the point density. The point density is given by the points used to form the rectangular shape at which the fit of the 1D-Fourier series is performed. The fit parameters are given by t_n, whereby the index n also represents the periodicity of $cos(nka)$.
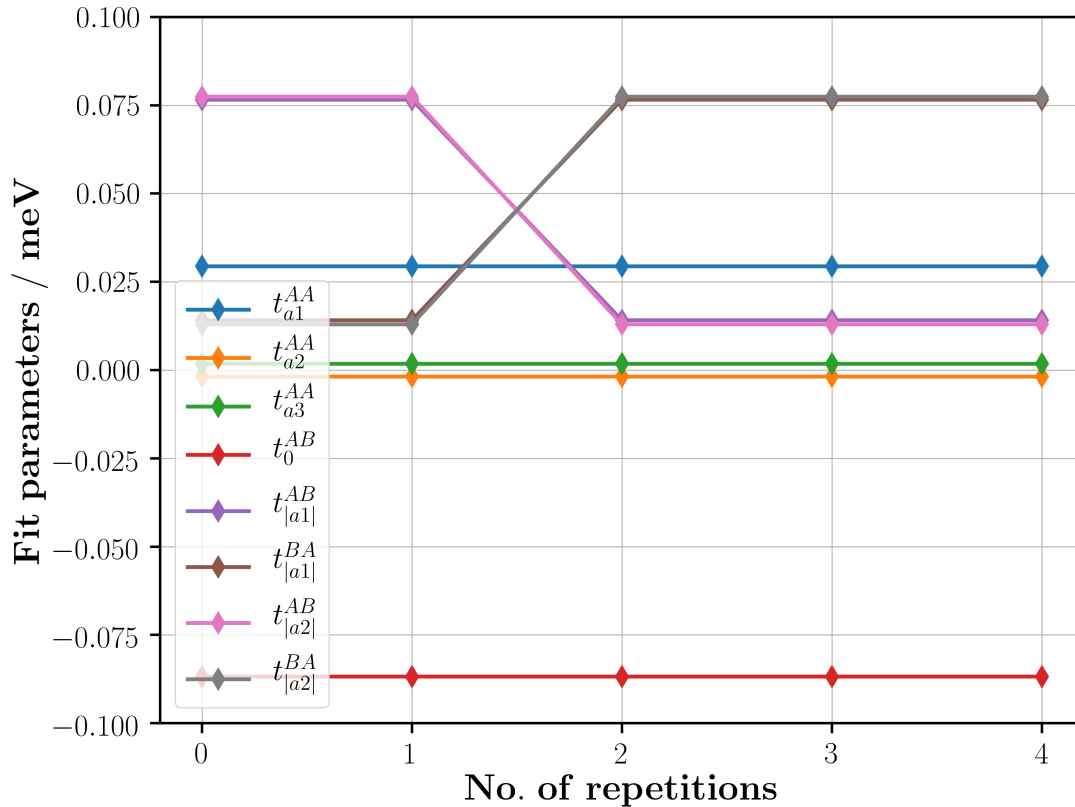
Fig. 5.22: Pentacene: The fitting procedure was repeated several times, which is indicated by the number of repetitions. The parameters were randomly initialized for every iteration. The graphs shows relevant fit parameters to demonstrate their behaviour.

for the reversed case will never vanish. The same arguments are valid for the parameters $t_{|a2|}^{AB}$ and $t_{|a2|}^{BA}$. To conclude this section, the stability of the two molecules per unit cell approach is given. Nevertheless, one has to keep in mind that the degree of freedom leads to different interpretations of the obtained results.

5.2.3 Limitations

Tight-binding fits present an efficient way to calculate electronic couplings of periodic structures. However, this methodology also includes limitations regarding the application on certain systems. The first limitation is simply that one has to use an appropriate model function. That means, if the system has a certain number of molecules in the unit cell, the tight-binding formalism has to be used to derive a suitable function. In this work, the case of one and two molecules are discussed, but there are also systems including more molecules per unit cell. In that case, the model function becomes quite
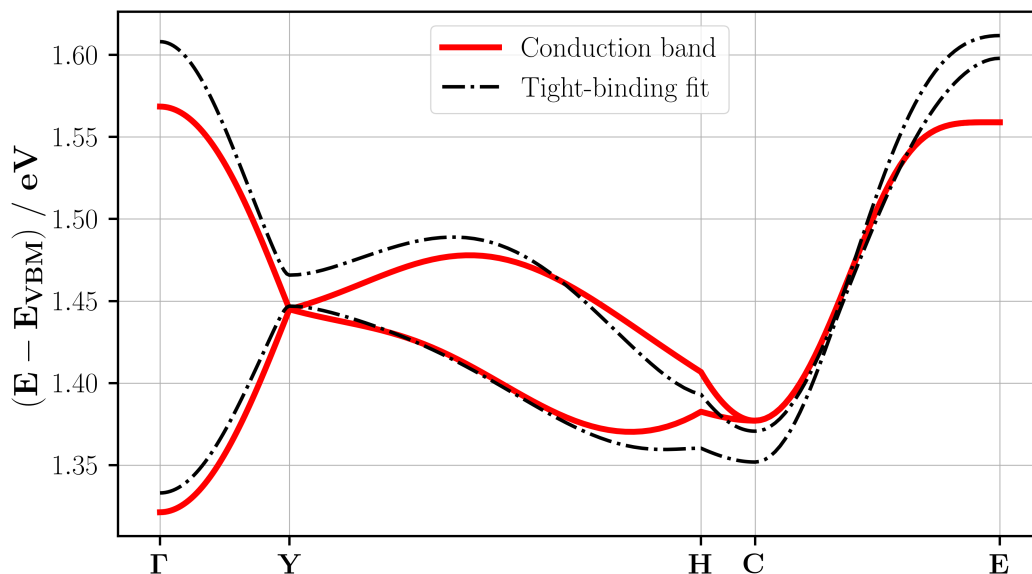
Fig. 5.23: The band structure of α-tetrathiafulvalene (TTF) indicates a crossing between CB (conduction band) and CB+1 at point Y. The model function for two molecules per unit cell (see Ch. 3.4) does not allow such crossings due to its mathematical structure.

complex and therefore an increase of instability is expected. The next issue is unique to the two (or more) molecules per unit cell approach. The possibility of band crossings arises. For example, the conduction band (CB) and the CB+1 can cross at a certain point. The latter can be found in the band structure of α-tetrathiafulvalene (TTF) as shown in Fig. 5.23. The lattice of α-TTF includes two molecules per unit cell and shows a triclinic crystalline structure. For more details on the structure, the work of Ellern et al. [57] is recommended. The band structure along high symmetry directions indicates a crossing at reciprocal point Y. As shown in the appendix A.1, the tight-binding model function from Ch. 3.4 does not allow such crossings due to its mathematical structure. Therefore, the application of this function to systems including crossings is limited. However, there would be possibilities to solve this issue. As first idea, one could write out the corresponding eigenvectors of the DFT-calculations. Further, one would have to project these eigenvectors on the basis functions of the molecules in the unit cell. From this, one could identify whether there is a crossing or an avoided-crossing. If there was a crossing, a simple virtual exchange of the bands at this point could be applied. Finally, the newly arranged data points could be fitted with the model function from above. Another idea would be to adapt the model function to be able to describe such crossings, but one would also have to know whether there is really a crossing in the band structure.

6 Comparison of Methodologies

In the present chapter, a comparison between cluster-based methods and tight-binding fits is presented. The results shown in this chapter were derived as explained in the corresponding chapters. Therefore, for the cluster-based approaches, namely Electronic splitting in Dimers, Fragment Orbital and Block Decomposition, see Ch. 5.1.3. The tight-binding fits are discussed in Ch. 5.2. The studied systems are the quinacridone α-phase and pentacene. The crystal structures and the chemical composition of those materials can be found in Ch. 4. The following results were obtained using the implementations shown in Ch. 3.

6.1 Quinacridone

The electronic couplings for the quinacridone α-phase were estimated for the hole and electron case. The absolute values of hole couplings are tabulated in Tab. 6.1, whereas the absolute values of electron couplings are listed in Tab. 6.2. For the sake of a more illustrative comparison, a bar plot of those couplings derived with PBE [7] is given in Fig. 6.1. The values for both cases, namely holes and electrons, show a good agreement in each direction. Small deviations occur for the tight-binding approach, but this is justified by taking the environment of the system into account. The results obtained by using the hybrid functional PBE0, as listed in the above-mentioned tables, indicate an increase of the absolute couplings. Nevertheless, in some directions, the PBE0 results show inconsistent behaviour. For possible interpretations of this behaviour see Ch. 5.2.

Tab. 6.1: Quinacridone α-phase: Absolute values of **hole** couplings estimated with cluster-based methods and a tight-binding (TB) fit. For cluster-based approaches, the Electronic splitting in Dimers (ESD), Fragment Orbital (FO) and Block Decomposition (BD) method were used. The couplings were calculated using the PBE and PBE0 functional. Direction... linear combinations of lattice vectors, which represent the coupling in those directions. All couplings are given in meV.

	ESD		FO		BD		TB	
Direction	PBE	PBE0	PBE	PBE0	PBE	PBE0	PBE	PBE0
a1	4.9	5.4	5.4	17.3	4.9	20.7	4.8	4.8
a2	6.1	7.5	6.6	10.9	6.1	2.2	9.7	11.9
a3	0.2	0.3	0.2	0.4	0.2	0.4	0.4	0.3
a1+a2	10.5	10.7	12.2	12.2	10.5	20.8	9.9	10.4
a2+a3	14.3	16.3	14.4	19.7	14.3	17.2	12.2	14.3
a2+a3-a1	3.0	3.3	3.0	5.0	3.0	4.8	5.2	5.8
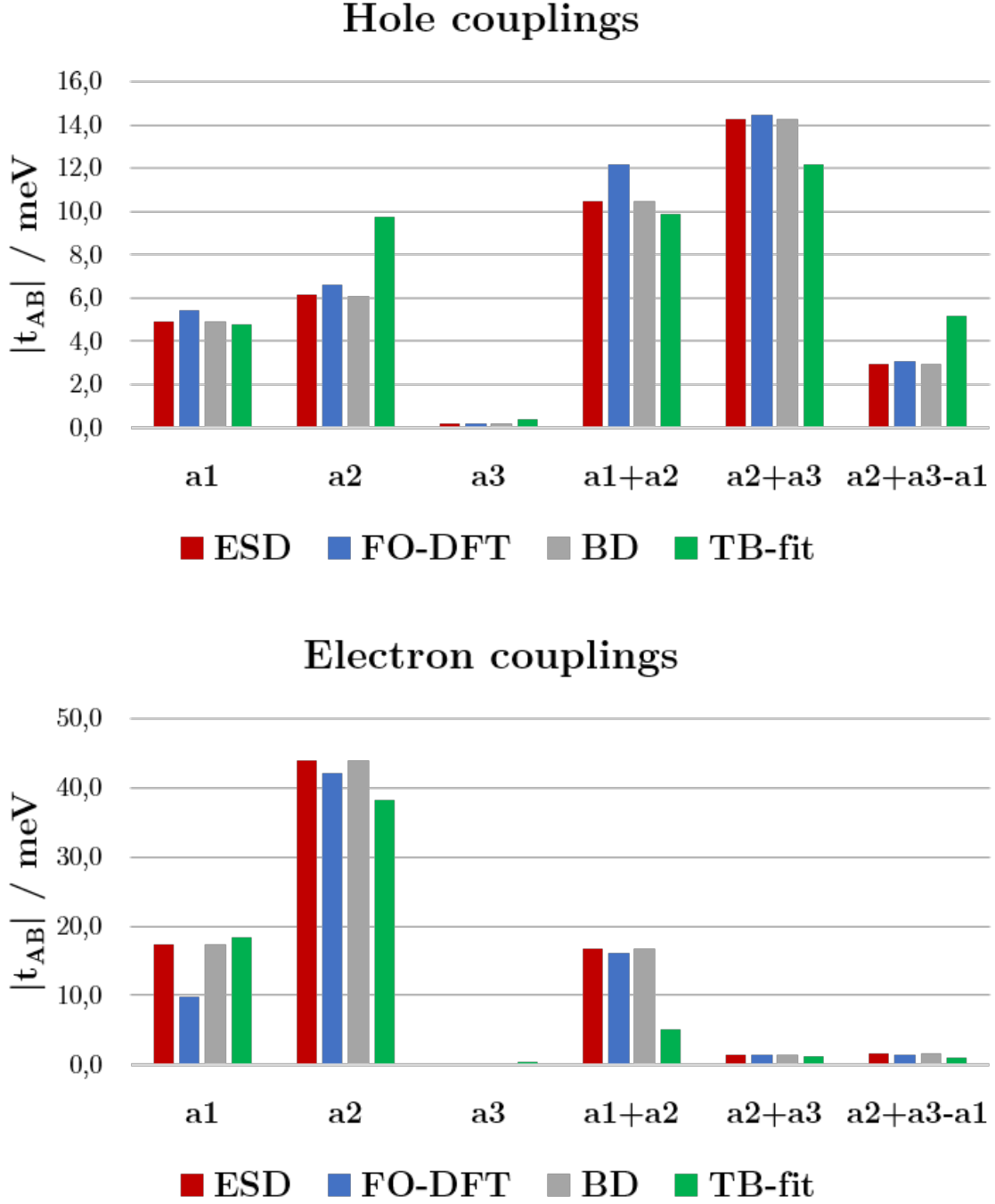
Fig. 6.1: Quinacridone α-phase: Comparison between cluster-based methods and a tight-binding fit. The bar plot shows absolute values of hole and electron couplings calculated with Electronic splitting in Dimers (ESD), Fragment Orbital (FO) and Block Decomposition (BD) method, representing cluster-based approaches. For the periodic case, the results of a tight-binding fit (TB) are shown. All couplings were obtained with the PBE functional. The couplings correspond to linear combinations of lattice vectors $\mathbf{a_i}$.

Tab. 6.2: Quinacridone α-phase: Absolute values of **electron** couplings estimated with cluster-based methods and a tight-binding (TB) fit. For cluster-based approaches, the Electronic splitting in Dimers (ESD), Fragment Orbital (FO) and Block Decomposition (BD) method were used. The couplings were calculated using the PBE and PBE0 functional. Direction... linear combinations of lattice vectors, which represent the coupling in those directions. All couplings are given in meV.

Direction	ESD		FO		BD		TB	
	PBE	PBE0	PBE	PBE0	PBE	PBE0	PBE	PBE0
a1	17.4	21.0	9.9	2.1	17.4	13.0	18.4	21.8
a2	43.9	50.0	42.1	54.4	43.9	72.1	38.3	44.6
a3	0.2	0.5	0.2	1.2	0.2	0.4	0.5	0.3
a1+a2	16.8	18.6	16.1	28.4	16.8	40.1	5.1	6.0
a2+a3	1.4	1.9	1.5	3.2	1.4	2.8	1.3	1.9
a2+a3-a1	1.6	1.8	1.5	2.1	1.6	3.0	1.0	1.3

6.2 Pentacene

For the pentacene structure, the absolute values of couplings for holes and electrons are tabulated in Tab. 6.3 and Tab. 6.4. The tables show results obtained with PBE and the hybrid functional PBE0 for cluster-based methods. For the tight-binding fits, couplings were calculated using the PBE functional. In this case, the PBE0 functional was not used due to the computational effort. For the sake of comparison, the results are visualized by a bar plot in Fig. 6.2. The graph shows the electronic couplings obtained with the PBE functional in certain directions. The results of the different approaches point a good agreement in all directions. Furthermore, the tight-binding fit shows just small deviations, which indicates that the influence of the environment is not that big for pentacene as for quinacridone.

Tab. 6.3: Pentacene: Absolute values of **hole** couplings estimated with cluster-based methods and a tight-binding (TB) fit. For cluster-based approaches, the Electronic splitting in Dimers (ESD), Fragment Orbital (FO) and Block Decomposition (BD) method were used. The couplings were calculated using the PBE and PBE0 functional, except for the tight-binding fit. Direction... linear combinations of lattice vectors, which represent the coupling in those directions. All couplings are given in meV.

	ESD		FO		BD		TB
Direction	PBE	PBE0	PBE	PBE0	PBE	PBE0	PBE
a1	35.5	42.5	36.0	44.8	35.5	44.5	29.4
a2	0.4	0.5	0.4	0.9	0.4	0.8	1.9
a3	1.3	1.4	1.3	2.0	1.3	2.3	2.1
(a1+a2)/2	156.2	176.7	53.6	72.1	59.4	71.8	46.3
(a2-a1)/2	182.7	203.4	84.9	116.7	88.1	117.6	84.6

Tab. 6.4: Pentacene: Absolute values of **electron** couplings estimated with cluster-based methods and a tight-binding (TB) fit. For cluster-based approaches, the Electronic splitting in Dimers (ESD), Fragment Orbital (FO) and Block Decomposition (BD) method were used. The couplings were calculated using the PBE and PBE0 functional, except for the tight-binding fit. Direction... linear combinations of lattice vectors, which represent the coupling in those directions. All couplings are given in meV.

	ESD		FO		BD		TB
Direction	PBE	PBE0	PBE	PBE0	PBE	PBE0	PBE
a1	42.7	51.2	43.2	54.1	42.7	53.3	37.2
a2	1.1	1.4	1.1	2.2	1.1	2.5	7.3
a3	9.4	11.1	9.2	14.3	9.3	17.3	1.7
(a1+a2)/2	166.8	190.4	83.9	109.9	88.2	109.0	79.6
(a2-a1)/2	179.2	200.4	80.9	107.4	85.4	110.1	80.9

Hole couplings

Electron couplings
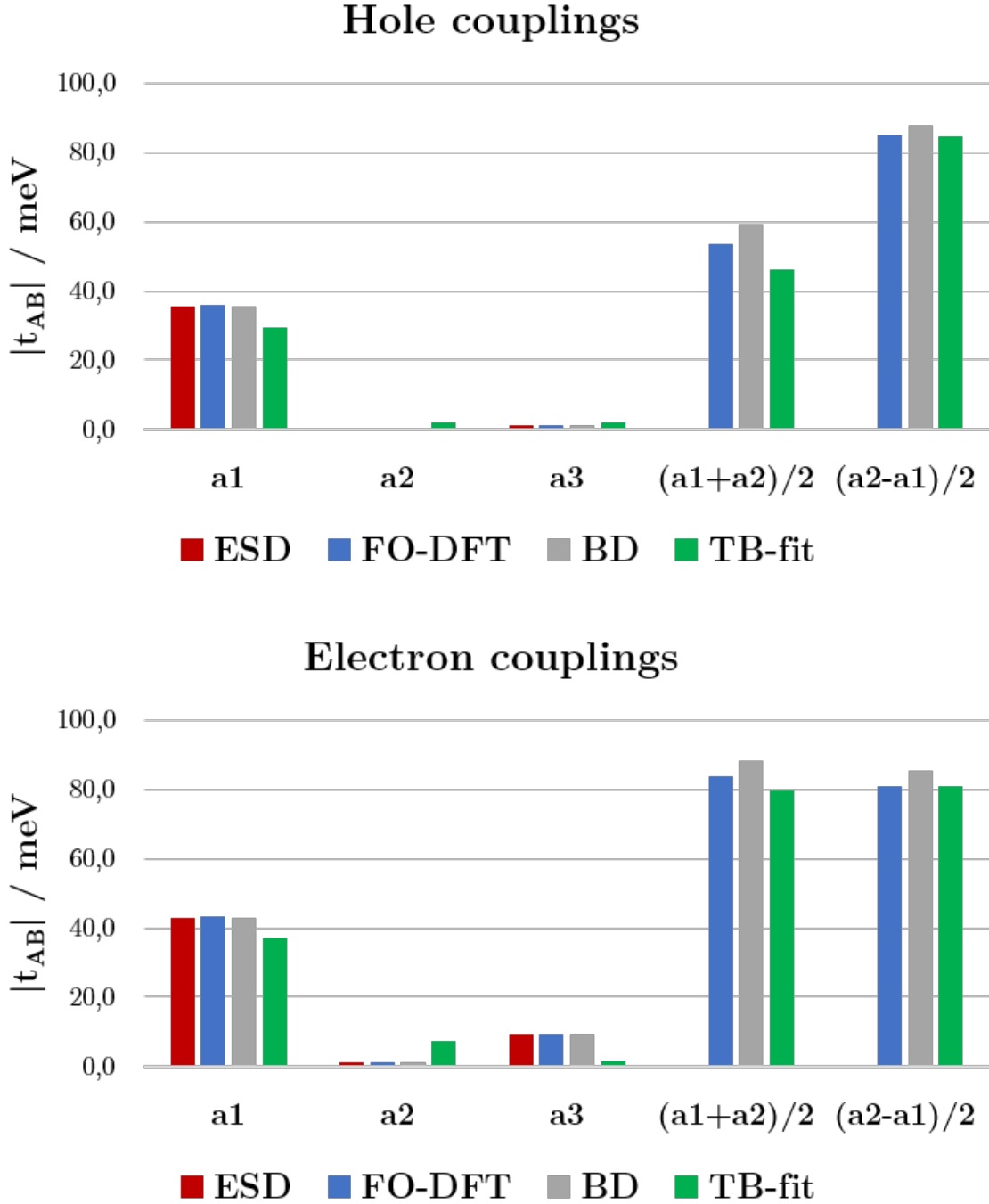
Fig. 6.2: Pentacene: Comparison between cluster-based methods and a tight-binding fit. The bar plot shows absolute values of hole and electron couplings obtained with Electronic splitting in Dimers (ESD), Fragment Orbital (FO) and Block Decomposition (BD) method, representing cluster-based approaches. For the periodic case, the results of a tight-binding fit (TB) are shown. All couplings were obtained with the PBE functional. The couplings correspond to linear combinations of lattice vectors $\mathbf{a_i}$.

7 Conclusion

The aim to provide accurate methodologies to estimate electronic couplings in organic systems has been achieved. Starting with the simplest approach, the so-called Electronic Splitting in Dimers method, the issue of polarization effects was discussed. The solution to this problem was found in the Fragment Orbital method, which is commonly used for estimating couplings. Furthermore, these methodologies were implemented and validated for different test systems. However, several considerations led to the idea of a new approach. Following the concept of decomposing matrices, a theoretical transformation was developed to evaluate electronic couplings without the requirement of fragment calculations. The suitability of this approach, which is called Block Decomposition, was tested on several organic systems. For that purpose, the results of the Block Decomposition approach were compared to those obtained using the well-established Fragment Orbital method. As a result, the suitability of the Block Decomposition method for different test systems was shown. Further, the behaviour of Fragment Orbital and Block Decomposition when using different functionals in the DFT calculation was studied. It turned out, that the use of hybrid functionals (e.g. PBE0) introduces inconsistencies at certain directions for quinacridone. Those inconsistencies occur for the Fragment Orbital and Block Decomposition method. Due to the fact that accurate high-level computed reference values were not available at the time of writing this thesis, a further investigation is still ongoing. Nevertheless, the use of GGA functionals, e.g. PBE, allows to accurately estimate electronic couplings.

The second part of this thesis showed the application of tight-binding fits to calculate electronic couplings of periodic structures. The suitability was shown for two systems, namely the quinacridone α-phase and pentacene. In general, the results for both systems were verified by comparing them to cluster-based methods. However, small deviations compared to the cluster-based results occur due to the inclusion of the environment. That indicates the importance of going beyond cluster-based approaches for certain directions. Nevertheless, there are still issues with the two molecules per unit cell approach. The additional degree of freedom within the fit has to be handled carefully to prevent wrong interpretations of results. Furthermore, if a system shows band-crossings, the discussed model function reaches its limits. However, there are possibilities to overcome this problem, which are mentioned in the corresponding sections.

Overall, the outcome of this thesis presents a tool-box including different implementations to accurately estimate electronic couplings. For the estimation of electronic couplings, the application of at least two different approaches is recommended. This allows to check the results and to exclude any errors in the calculation.

Bibliography

[1] Richard M. Martin. *Electronic structure : basic theory and practical methods.* Cambridge University Press, 2004.

[2] M. Born and R. Oppenheimer. Zur Quantentheorie der Molekeln. *Annalen der Physik*, 389(20):457–484, 1927.

[3] A Szabo and N S Ostlund. *Modern Quantum Chemistry: Introduction to Advanced Electronic Structure Theory.* Dover Books on Chemistry. Dover Publications, 1996.

[4] P. Hohenberg and W. Kohn. Inhomogeneous Electron Gas. *Physical Review*, 136(3B):B864–B871, nov 1964.

[5] W. Kohn and L. J. Sham. Self-Consistent Equations Including Exchange and Correlation Effects. *Physical Review*, 140(4A):A1133–A1138, nov 1965.

[6] John P. Perdew and Yue Wang. Accurate and simple analytic representation of the electron-gas correlation energy. *Physical Review B*, 45(23):13244–13249, jun 1992.

[7] John P. Perdew, Kieron Burke, and Matthias Ernzerhof. Generalized gradient approximation made simple. *Physical Review Letters*, 77(18):3865–3868, 1996.

[8] John P. Perdew, Matthias Ernzerhof, and Kieron Burke. Rationale for mixing exact exchange with density functional approximations. *Journal of Chemical Physics*, 105(22):9982–9985, 1996.

[9] Volker Blum, Ralf Gehrke, Felix Hanke, Paula Havu, Ville Havu, Xinguo Ren, Karsten Reuter, and Matthias Scheffler. Ab initio molecular simulations with numeric atom-centered orbitals. *Computer Physics Communications*, 180(11):2175–2196, 2009.

[10] F Bloch. Über die Quantenmechanik der Elektronen in Kristallgittern. *Zeitschrift fur Physik*, 52:555–600, 1929.

[11] Charles Kittel. *Introduction to Solid State Physics.* Wiley, 8 edition, 2004.

[12] Veaceslav Coropceanu, Jérôme Cornil, Demetrio A. da Silva Filho, Yoann Olivier, Robert Silbey, and Jean Luc Brédas. Charge transport in organic semiconductors. *Chemical Reviews*, 107(4):926–952, 2007.

[13] Harald Oberhofer, Karsten Reuter, and Jochen Blumberger. Charge Transport in Molecular Materials: An Assessment of Computational Methods. *Chemical Reviews*, 117(15):10319–10357, 2017.

[14] R Gross and A Marx. *Festkörperphysik.* Oldenbourg Wissenschaftsverlag, 2012.

[15] R. A. Marcus. On the theory of oxidation-reduction reactions involving electron transfer. I. *The Journal of Chemical Physics*, 24(5):966–978, 1956.

[16] R. A. Marcus. Electrostatic free energy and other properties of states having nonequilibrium polarization. I. *The Journal of Chemical Physics*, 24(5):979–989, 1956.

[17] Simone Fratini, Didier Mayou, and Sergio Ciuchi. The transient localization scenario for charge transport in crystalline organic materials. *Advanced Functional Materials*, 26(14):2292–2315, 2016.

[18] S. Fratini, S. Ciuchi, D. Mayou, G. Trambly De Laissardière, and A. Troisi. A map of high-mobility molecular semiconductors. *Nature Materials*, 16(10):998–1002, 2017.

[19] R. A. Marcus. On the theory of oxidation-reduction reactions involving electron transfer. II. Applications to data on the rates of isotopic exchange reactions. *The Journal of Chemical Physics*, 26(4):867–871, 1957.

[20] R. A. Marcus. On the theory of oxidation-reduction reactions involving electron transfer. III. applications to data on the rates of organic redox reactions. *The Journal of Chemical Physics*, 26(4):872–877, 1957.

[21] A Marcus Rudolph. Electron Transfer Reactions in Chemistry: Theory and Experiment (Nobel Lecture). *Angewandte Chemie International Edition in English*, 32(8):1111–1121, 1993.

[22] Harald Oberhofer and Jochen Blumberger. Revisiting electronic couplings and incoherent hopping models for electron transport in crystalline C60at ambient temperatures. *Physical Chemistry Chemical Physics*, 14(40):13846–13852, 2012.

[23] P W Atkins and J de Paula. *Atkins' Physical Chemistry*. OUP Oxford, 2014.

[24] Geoffrey R. Hutchison, Mark A. Ratner, and Tobin J. Marks. Hopping transport in conductive heterocyclic oligomers: Reorganization energies and substituent effects. *Journal of the American Chemical Society*, 127(7):2339–2350, 2005.

[25] T. Pacher, L. S. Cederbaum, and H. Köppel. Approximately diabatic states from block diagonalization of the electronic Hamiltonian. *The Journal of Chemical Physics*, 89(12):7367–7381, 1988.

[26] W. Domcke and C. Woywod. Direct construction of diabatic states in the CASSCF approach. Application to the conical intersection of the1A2and1B1excited states of ozone. *Chemical Physics Letters*, 216(3-6):362–368, 1993.

[27] Robert J. Cave and Marshall D. Newton. Generalization of the Mulliken-Hush treatment for the calculation of electron transfer matrix elements. *Chemical Physics Letters*, 249(1-2):15–19, 1996.

[28] Robert J. Cave and Marshall D. Newton. Calculation of electronic coupling matrix elements for ground and excited state electron transfer reactions: Comparison of the generalized Mulliken-Hush and block diagonalization methods. *Journal of Chemical Physics*, 106(22):9213–9226, 1997.

[29] Robert S. Mulliken. Molecular Compounds and their Spectra. II. *Journal of the American Chemical Society*, 74(3):811–824, 1952.

[30] K. Senthilkumar, F. C. Grozema, F. M. Bickelhaupt, and L. D.A. Siebbeles. Charge transport in columnar stacked triphenylenes: Effects of conformational fluctuations on charge transfer integrals and site energies. *Journal of Chemical Physics*, 119(18):9809–9817, 2003.

[31] Qin Wu and Troy Van Voorhis. Extracting electron transfer coupling elements from constrained density functional theory. *Journal of Chemical Physics*, 125(16), 2006.

[32] Qin Wu and Troy Van Voorhis. Constrained density functional theory and its application in long-range electron transfer. *Journal of Chemical Theory and Computation*, 2(3):765–774, 2006.

[33] O. Kwon, V. Coropceanu, N. E. Gruhn, J. C. Durivage, J. G. Laquindanum, H. E. Katz, J. Cornil, and J. L. Brédas. Characterization of the molecular parameters determining charge transport in anthradithiophene. *Journal of Chemical Physics*, 120(17):8186–8194, 2004.

[34] Jingsong Huang and Miklos Kertesz. Validation of intermolecular transfer integral and bandwidth calculations for organic molecular materials. *Journal of Chemical Physics*, 122(23), 2005.

[35] Edward F. Valeev, Veaceslav Coropceanu, Demetrio A. Da Silva Filho, Seyhan Salman, and Jean Luc Brédas. Effect of electronic polarization on charge-transport parameters in molecular organic semiconductors. *Journal of the American Chemical Society*, 128(30):9882–9886, 2006.

[36] Kittusamy Senthilkumar, Ferdinand C. Grozema, Célia Fonseca Guerra, F. Matthias Bickelhaupt, Frederick D. Lewis, Yuri A. Berlin, Mark A. Ratner, and Laurens D.A. Siebbeles. Absolute rates of hole transfer in DNA. *Journal of the American Chemical Society*, 127(42):14894–14903, 2005.

[37] Per Olov Löwdin. On the non-orthogonality problem connected with the use of atomic wave functions in the theory of molecules and crystals. *The Journal of Chemical Physics*, 18(3):365–375, 1950.

[38] By Kenneth and Levenberg Frankford. A Method for the Solution of Certain Non-Linear. 1(278):536–538, 1943.

[39] Donald W Marquardt. An algorithm for least-squares estimation of nonlinear parameters. *SIAM Journal on Applied Mathematics*, 11(2):431–441, 1963.

[40] M J D Powell. An efficient method for finding the minimum of a function of several variables without calculating derivatives. *The Computer Journal*, 7(2):155, 1964.

[41] M.R. Hestenes and E. Stiefel. Methods of conjugate gradients for solving linear systems. *Journal of Research of the National Bureau of Standards*, 49(6):409, 1952.

[42] J A Nelder and R Mead. A Simplex Method for Function Minimization. *The Computer Journal*, 7(4):308–313, 1965.

[43] Adam Kubas, Fruzsina Gajdos, Alexander Heck, Harald Oberhofer, Marcus Elstner, and Jochen Blumberger. Electronic couplings for molecular charge transfer: Benchmarking CDFT, FODFT and FODFTB against high-level ab initio calculations. II. *Physical Chemistry Chemical Physics*, 17(22):14342–14354, 2015.

[44] Erich F. Paulus, Frank J.J. Leusen, and Martin U. Schmidt. Crystal structures of quinacridones. *CrystEngComm*, 9(2):131–143, 2007.

[45] Wahyu Setyawan and Stefano Curtarolo. High-throughput electronic band structure calculations: Challenges and tools. *Computational Materials Science*, 49(2):299–312, 2010.

[46] Christine C. Mattheus, Anne B. Dros, Jacob Baas, Gert T. Oostergetel, Auke Meetsma, Jan L. De Boer, and T. T M Palstra. Identification of polymorphs of pentacene. *Synthetic Metals*, 138(3):475–481, 2003.

[47] Daniel Holmes, Sriram Kumaraswamy, Adam J Matzger, and K Peter C Vollhardt. On the Nature of Nonplanarity in the [N]Phenylenes. *Chemistry - A European Journal*, 5(11):3399–3412, 1999.

[48] Alexandre Tkatchenko and Matthias Scheffler. Accurate molecular van der Waals interactions from ground-state electron density and free-atom reference data. *Physical Review Letters*, 102(7):6–9, 2009.

[49] FHI-aims Team. Fritz Haber Institute ab initio molecular simulations: FHI- aims. Technical report, Berlin, 2016.

[50] Hans Joachim Werner and Ernst Albrecht Reinsch. The self-consistent electron pairs method for multiconfiguration reference state functions. *The Journal of Chemical Physics*, 76(6):3144–3156, 1982.

[51] Masaaki Saitow, Yuki Kurashige, and Takeshi Yanai. Multireference configuration interaction theory using cumulant reconstruction with internal contraction of density matrix renormalization group wave function. *Journal of Chemical Physics*, 139(4), 2013.

[52] Stephen R. Langhoff and Ernest R. Davidson. Configuration interaction calculations on the nitrogen molecule. *International Journal of Quantum Chemistry*, 8(1):61–72, 1974.

[53] C. Angeli, R. Cimiraglia, S. Evangelisti, T. Leininger, and J. P. Malrieu. Introduction of n-electron valence states for multireference perturbation theory. *Journal of Chemical Physics*, 114(23):10252, 2001.

[54] Celestino Angeli, Renzo Cimiraglia, and Jean Paul Malrieu. n-electron valence state perturbation theory: A spinless formulation and an efficient implementation of the strongly contracted and of the partially contracted variants. *Journal of Chemical Physics*, 117(20):9138–9153, 2002.

[55] Christoph Schober, Karsten Reuter, and Harald Oberhofer. Critical analysis of fragment-orbital DFT schemes for the calculation of electronic coupling values. *Journal of Chemical Physics*, 144(5), 2016.

[56] Christian Winkler, Florian Mayer, and Egbert Zojer. Analyzing the Electronic Coupling in Molecular Crystals—The Instructive Case of α-Quinacridone. *Advanced Theory and Simulations*, 1800204:1800204, 2019.

[57] Arkady Ellern, Joel Bernstein, James Y. Becker, Zamir Sharona, Shahal Leah, and Shmuel Cohen. A New Polymorphic Modification of Tetrathiafulvalene. Crystal Structure, Lattice Energy and Intermolecular Interactions. *Chemistry of Materials*, 6(8):1378–1385, 1994.

A Appendix

A.1 Non-Crossing Property

A proof of the non-crossing property for the model function below is provided:

$$\epsilon_{1,2}(\mathbf{k}) = \frac{H_{AA}(\mathbf{k}) + H_{BB}(\mathbf{k})}{2} \pm \sqrt{\frac{(H_{AA}(\mathbf{k}) - H_{BB}(\mathbf{k}))^2}{4} + |H_{AB}(\mathbf{k})|^2} \qquad \text{(A.1)}$$

The following relation has to be valid for all k-vectors to proof the non-crossing behaviour.

$$\epsilon_1(\mathbf{k}) > \epsilon_2(\mathbf{k}) \qquad \text{(A.2)}$$

The next step is to plug the expressions for $\epsilon_{1,2}$ into the equation above.

$$\frac{H_{AA}(\mathbf{k}) + H_{BB}(\mathbf{k})}{2} + \sqrt{\frac{(H_{AA}(\mathbf{k}) - H_{BB}(\mathbf{k}))^2}{4} + |H_{AB}(\mathbf{k})|^2} >$$
$$\frac{H_{AA}(\mathbf{k}) + H_{BB}(\mathbf{k})}{2} - \sqrt{\frac{(H_{AA}(\mathbf{k}) - H_{BB}(\mathbf{k}))^2}{4} + |H_{AB}(\mathbf{k})|^2} \quad \text{(A.3)}$$

Furthermore, the first terms on each side can be reduced. Finally, the square root terms remain on both sides. Since they have to be positive to garuantee real numbers for the energy $\epsilon(\mathbf{k})$, the left side will give the higher number in any case.

$$\sqrt{\frac{(H_{AA}(\mathbf{k}) - H_{BB}(\mathbf{k}))^2}{4} + |H_{AB}(\mathbf{k})|^2} > -\sqrt{\frac{(H_{AA}(\mathbf{k}) - H_{BB}(\mathbf{k}))^2}{4} + |H_{AB}(\mathbf{k})|^2} \quad \text{(A.4)}$$

That short derivation justifies the assumption of non-crossing within the tight-binding model function for two molecules per unit cell.

A.2 Source Code: Fragment Orbital

```python
1   """
2   Fragment Orbital Implementation
3   Created on 22.04.2019
4
5   @author: Florian Mayer
6   florian.mayer@student.tugraz.at
7   """
8   from read_functions_ESD import *
9   from scipy.sparse import coo_matrix
10  import scipy.linalg as LA
11
12  def fragment_orbital(main_path,state_f01,state_f02,state_d,pickstate):
13      """
14      USER INPUTS:
15          main_path...path to folder containing:
16              /dimer_01
17              /frag_01
18              /frag_02
19          state_f01...Fragment A state to be picked
20          state_f02...Fragment B state to be picked
21          state_d...Dimer state to be picked
22          pickstate...picks the corresponding dimer state for the 2 state system:
23              e.g. +1 picks the state_d+1
24                   -1 picks the state_d-1
25          Example: Phenol
26                  state_f01=24 (HOMO)
27                  state_f02=24 (HOMO)
28                  state_d=49 (HOMO)
29                  pickstate=-1 (HOMO-1)
30      """
31
32      """
33      Dimer data -> load dimer hamilton matrix, load dimer overlap matrix
34      """
35      dimer_path=main_path+'dimer_01/'
36      ham_dimer=read_hamiltonian(dimer_path)
37      ovp_dimer=read_overlap(dimer_path)
38      eigvec_dimer=read_eigenvectors(dimer_path)
39      eigvals_dimer=get_splitting(dimer_path)
40
41      """
42      Fragment 1 data -> load frag01 eigenvectors, load frag01 output.aims2 data
43      """
44      frag01_path=main_path+'frag_01/'
45      eigvals_f01=get_splitting(frag01_path)
46      eigvec_f01=read_eigenvectors(frag01_path)
47
48
49      equality='No'
50      """
51      Fragment 2 data -> if fragment1!=fragment2 then load frag02 eigenvectors,
52      load frag02 output.aims2 data
53      """
54      frag02_path=main_path+'frag_02/'
55      if equality=='No':
56          eigvals_f02=get_splitting(frag02_path)
57          eigvec_f02=read_eigenvectors(frag02_path)
58      else:
59          eigvals_f02=eigvals_f01
60          eigvec_f02=eigvec_f01
61
62
63      """Main Part: Estimation of Electronic Couplings"""
64
65
66      #First Task: Calculating the transfer integral in non-orthogonal basis
67      j_transfer=0
68      s_12=0
69      siz_ham=np.shape(ham_dimer)
70      siz_f01=np.shape(eigvec_f01)
71      siz_f02=np.shape(eigvec_f02)
72      n_basis1=siz_f01[0]
```

```python
 73            n_basis2=siz_f02[0]
 74            cnt=0
 75            for i1 in range(siz_ham[0]):
 76                if (ham_dimer[i1,1]>n_basis1) and (ham_dimer[i1,0]<=n_basis1):
 77                    f01_index=ham_dimer[i1,0].astype(int)-1
 78                    f02_index=ham_dimer[i1,1].astype(int)-1
 79                    f02_index=f02_index-n_basis1
 80                    j_transfer=j_transfer+eigvec_f01[f01_index,state_f01]*eigvec_f02[
                       f02_index,state_f02]*ham_dimer[i1,2]
 81                    s_12=s_12+eigvec_f01[f01_index,state_f01]*eigvec_f02[f02_index,state_f02
                       ]*ovp_dimer[i1,2]
 82                    cnt=cnt+1
 83
 84
 85            i_index=np.array(ovp_dimer[:,0],dtype=int)
 86            j_index=np.array(ovp_dimer[:,1],dtype=int)
 87
 88            #Reshaping of sparse matrices into full matrices
 89            ovp_dimer_full=coo_matrix((ovp_dimer[:,2], (i_index-1,j_index-1))).toarray()
 90            he2_mat=np.transpose(np.triu(ovp_dimer_full,1))
 91            ovp_dimer_full=ovp_dimer_full+he2_mat
 92
 93            ham_dimer_full=coo_matrix((ham_dimer[:,2], (i_index-1,j_index-1))).toarray()
 94            he_mat=np.transpose(np.triu(ham_dimer_full,1))
 95            ham_dimer_full=ham_dimer_full+he_mat
 96
 97            siz_full=ovp_dimer_full.shape
 98
 99            #Different operations to extract the overlap and on-site energies
100            #in the non-orthogonal basis
101
102            block_f1=np.zeros(siz_full)
103            block_s1=np.zeros(siz_full)
104            for n1 in range(siz_full[1]/2):
105                for n2 in range(siz_full[0]/2):
106                    block_f1[n1,n2]=ham_dimer_full[n1,n2]
107                    block_s1[n1,n2]=ovp_dimer_full[n1,n2]
108
109
110            block_f21=np.zeros(siz_full)
111            block_s21=np.zeros(siz_full)
112            for n1 in range(siz_full[1]/2,siz_full[1]):
113                for n2 in range(siz_full[0]/2):
114                    block_f21[n1,n2]=ham_dimer_full[n1,n2]
115                    block_s21[n1,n2]=ovp_dimer_full[n1,n2]
116
117            block_s12=np.zeros(siz_full)
118            block_f12=np.zeros(siz_full)
119            for n1 in range(siz_full[1]/2):
120                for n2 in range(siz_full[0]/2,siz_full[0]):
121                    block_s12[n1,n2]=ovp_dimer_full[n1,n2]
122                    block_f12[n1,n2]=ham_dimer_full[n1,n2]
123
124
125            block_trans12_ovp=block_s12[0:siz_full[0]/2,siz_full[1]/2:]
126            block_trans21_ovp=block_s21[siz_full[0]/2:,0:siz_full[1]/2]
127
128
129            psi_f1_homo=eigvec_f01[:,state_f01]
130            psi_f2_homo=eigvec_f02[:,state_f02]
131
132            block_f2=np.zeros(siz_full)
133            block_s2=np.zeros(siz_full)
134            for n1 in range(siz_full[1]/2,siz_full[1]):
135                for n2 in range(siz_full[0]/2,siz_full[0]):
136                    block_f2[n1,n2]=ham_dimer_full[n1,n2]
137                    block_s2[n1,n2]=ovp_dimer_full[n1,n2]
138
139            block_H11=block_f1[0:siz_full[0]/2,0:siz_full[1]/2]
140
141            block_trans12=block_f12[0:siz_full[0]/2,siz_full[1]/2:]
142            block_trans21=block_f21[0:siz_full[0]/2,siz_full[1]/2:]
```

```python
143
144         block_H22=block_f2[siz_full[0]/2:,siz_full[1]/2:]
145         block_H12=block_trans12
146
147         e_1=np.matmul(block_H11,psi_f1_homo)
148         e_1=np.matmul(np.transpose(psi_f1_homo),e_1)
149         e_1=e_1*27.211
150
151         e_2=np.matmul(block_H22,psi_f2_homo)
152         e_2=np.matmul(np.transpose(psi_f2_homo),e_2)
153         e_2=e_2*27.211
154
155         j_transfer=j_transfer*27.211
156
157         s_21_n=np.matmul(block_trans21_ovp,psi_f2_homo)
158         s_21_n=np.matmul(np.transpose(psi_f1_homo),s_21_n)
159         s_21=s_21_n
160
161         block_S11=block_s1[0:siz_full[0]/2,0:siz_full[1]/2]
162         block_S22=block_s2[siz_full[0]/2:,siz_full[1]/2:]
163
164         s_f1=np.matmul(block_S11,psi_f1_homo)
165         s_f1=np.matmul(np.transpose(psi_f1_homo),s_f1)
166         s_f2=np.matmul(block_S22,psi_f1_homo)
167         s_f2=np.matmul(np.transpose(psi_f1_homo),s_f2)
168
169         #Performing Löwdins symmetry transformation:
170         e_eff1=0.5*((e_1+e_2)-2*j_transfer*s_12+(e_1-e_2)*np.sqrt(1-s_12**2))/(1-s_12**2)
171         e_eff2=0.5*((e_1+e_2)-2*j_transfer*s_12-(e_1-e_2)*np.sqrt(1-s_12**2))/(1-s_12**2)
172         #Calculating final result for electronic coupling
173         j_eff=(j_transfer-0.5*(e_1+e_2)*s_12)/(1-s_12**2)
174
175         res_splitting=np.sqrt((e_eff1-e_eff2)**2+(2*j_eff)**2)
176         #Electronic splitting in Dimer method (using DFT-data)
177         ESD=eigvals_dimer[state_d]-eigvals_dimer[state_d-1]
178
179         t_eff=j_eff
180         results=np.array([[j_eff],[e_eff1],[e_eff2],[res_splitting],[e_1],[e_2],[ESD]])
181         add_data=np.transpose(results)
182         """OUTPUT"""
183         print "--------------------------------"
184         print "Fragment Orbital method..."
185         print "Florian Mayer / TUGraz 2018"
186         print "--------------------------------"
187         print "Inputs:"
188         print "Fragment A state: "+str(state_f01)+" | Fragment B state: "+str(state_f02)
189         print "Dimer state I: "+str(state_d)+" | Dimer state II: "+str(state_d+pickstate)
190         print "--------------------------------"
191         print "Detailed Results / eV :"
192         print "e_1  (non-ortho)       : "+str(e_1)
193         print "e_2  (non-ortho)       : "+str(e_2)
194         print "e_1eff  (ortho)        : "+str(e_eff1)
195         print "e_2eff  (ortho)        : "+str(e_eff2)
196         print "t_12 (non-ortho)       : "+str(j_transfer)
197         print "E_12 (splitting FO )   : "+str(res_splitting)
198         print "ESD  (splitting DFT)   : "+str(ESD)
199         print "ESD/2                  : "+str(ESD/2)
200         print "e_1-e_2 (onsite spl)   : "+str(e_1-e_2)
201         print "ESD-E_12 (hybrid hf)   : "+str(ESD-res_splitting)
202         print "--------------------------------"
203         print "Electronic coupling t_eff / meV"
204         print "t_eff : "+str(t_eff*1000)
205         print "--------------------------------"
206         return t_eff,add_data
```

A.3 Source Code: Block Decomposition

```python
"""
Block Decomposition Implementation
Created on 22.04.2019

@author: Florian Mayer
florian.mayer@student.tugraz.at
"""
from read_functions_ESD import *
from scipy.sparse import coo_matrix
import scipy.linalg as LA

def block_decomposition(main_path,state_d,pickstate):
    """
    USER INPUTS:
        main_path...path to folder containing:
            /dimer_01
        state_d...Dimer state to be picked
        pickstate...picks the corresponding dimer state for the 2 state system:
            e.g. +1 picks the state_d+1
                 -1 picks the state_d-1
        Example: Phenol
                state_d=49 (HOMO)
                pickstate=-1 (HOMO-1)
    """
    state_d2=state_d+pickstate
    """
    Dimer data -> load dimer hamilton matrix, load dimer overlap matrix
    """
    dimer_path=main_path+'dimer_01/'
    ham_dimer=read_hamiltonian(dimer_path)
    ovp_dimer=read_overlap(dimer_path)
    eigvec_dimer=read_eigenvectors(dimer_path)
    eigvals_dimer=get_splitting(dimer_path)

    """Main Part: Estimation of Electronic Couplings"""

    """
    Reshaping of sparse matrices into full matrices
    """
    i_index=np.array(ham_dimer[:,0],dtype=int)
    j_index=np.array(ham_dimer[:,1],dtype=int)
    ham_dimer_full=coo_matrix((ham_dimer[:,2], (i_index-1,j_index-1))).toarray()
    he_mat=np.transpose(np.triu(ham_dimer_full,1))
    ham_dimer_full=ham_dimer_full+he_mat
    ovp_dimer_full=coo_matrix((ovp_dimer[:,2], (i_index-1,j_index-1))).toarray()
    he2_mat=np.transpose(np.triu(ovp_dimer_full,1))
    ovp_dimer_full=ovp_dimer_full+he2_mat

    psi_dimer_homo=eigvec_dimer[:,state_d]
    psi_dimer_homo_m1=eigvec_dimer[:,state_d2]

    state_en=np.matmul(ham_dimer_full,psi_dimer_homo)
    state_en=np.matmul(np.transpose(psi_dimer_homo),state_en)
    state_en=state_en*27.211

    #Block Decomposition of Matrices
    siz_full=ham_dimer_full.shape
    block_f1=np.zeros(siz_full)
    block_s1=np.zeros(siz_full)
    for n1 in range(siz_full[1]/2):
        for n2 in range(siz_full[0]/2):
            block_f1[n1,n2]=ham_dimer_full[n1,n2]
            block_s1[n1,n2]=ovp_dimer_full[n1,n2]

    onsite_f1=np.matmul(block_f1,psi_dimer_homo)
    onsite_f1=np.matmul(np.transpose(psi_dimer_homo),onsite_f1)
    onsite_f1=onsite_f1*27.211

    onsite_s1=np.matmul(block_s1,psi_dimer_homo)
    onsite_s1=np.matmul(np.transpose(psi_dimer_homo),onsite_s1)
```

```
73          onsite_f1_h1=np.matmul(block_f1,psi_dimer_homo_m1)
74          onsite_f1_h1=np.matmul(np.transpose(psi_dimer_homo_m1),onsite_f1_h1)
75          onsite_f1_h1=onsite_f1_h1*27.211
76
77          onsite_s1_h1=np.matmul(block_s1,psi_dimer_homo_m1)
78          onsite_s1_h1=np.matmul(np.transpose(psi_dimer_homo_m1),onsite_s1_h1)
79
80      block_f2=np.zeros(siz_full)
81      block_s2=np.zeros(siz_full)
82      for n1 in range(siz_full[1]/2,siz_full[1]):
83          for n2 in range(siz_full[0]/2,siz_full[0]):
84              block_f2[n1,n2]=ham_dimer_full[n1,n2]
85              block_s2[n1,n2]=ovp_dimer_full[n1,n2]
86
87      onsite_f2=np.matmul(block_f2,psi_dimer_homo)
88      onsite_f2=np.matmul(np.transpose(psi_dimer_homo),onsite_f2)
89      onsite_f2=onsite_f2*27.211
90
91      onsite_s2=np.matmul(block_s2,psi_dimer_homo)
92      onsite_s2=np.matmul(np.transpose(psi_dimer_homo),onsite_s2)
93
94      onsite_f2_h1=np.matmul(block_f2,psi_dimer_homo_m1)
95      onsite_f2_h1=np.matmul(np.transpose(psi_dimer_homo_m1),onsite_f2_h1)
96      onsite_f2_h1=onsite_f2_h1*27.211
97
98      onsite_s2_h1=np.matmul(block_s2,psi_dimer_homo_m1)
99      onsite_s2_h1=np.matmul(np.transpose(psi_dimer_homo_m1),onsite_s2_h1)
100
101
102     block_f12=np.zeros(siz_full)
103     block_s12=np.zeros(siz_full)
104     for n1 in range(siz_full[1]/2):
105         for n2 in range(siz_full[0]/2,siz_full[0]):
106             block_f12[n1,n2]=ham_dimer_full[n1,n2]
107             block_s12[n1,n2]=ovp_dimer_full[n1,n2]
108
109     block_f21=np.zeros(siz_full)
110     block_s21=np.zeros(siz_full)
111     for n1 in range(siz_full[1]/2,siz_full[1]):
112         for n2 in range(siz_full[0]/2):
113             block_f21[n1,n2]=ham_dimer_full[n1,n2]
114             block_s21[n1,n2]=ovp_dimer_full[n1,n2]
115
116     block_fab=block_f12+block_f21
117     block_sab=block_s12+block_s21
118
119     trans_fab=np.matmul(block_fab,psi_dimer_homo)
120     trans_fab=np.matmul(np.transpose(psi_dimer_homo),trans_fab)
121     trans_fab=trans_fab*27.211
122
123     trans_fab2=np.matmul(block_fab,psi_dimer_homo)
124     trans_fab2=np.matmul(np.transpose(psi_dimer_homo_m1),trans_fab2)
125     trans_fab2=trans_fab2*27.211
126
127     trans_sab=np.matmul(block_sab,psi_dimer_homo)
128     trans_sab=np.matmul(np.transpose(psi_dimer_homo),trans_sab)
129
130     trans_fab_h1=np.matmul(block_fab,psi_dimer_homo_m1)
131     trans_fab_h1=np.matmul(np.transpose(psi_dimer_homo_m1),trans_fab_h1)
132     trans_fab_h1=trans_fab_h1*27.211
133
134     trans_sab_h1=np.matmul(block_sab,psi_dimer_homo_m1)
135     trans_sab_h1=np.matmul(np.transpose(psi_dimer_homo_m1),trans_sab_h1)
136
137     """Electronic Splitting in Dimers method"""
138     ESD_DFT=eigvals_dimer[state_d]-eigvals_dimer[state_d2]
139     t_check=ESD_DFT/2
140
141     """Approximation of on-site energies"""
142     EA=onsite_f1
143     EAH=onsite_f1_h1
144     EB=onsite_f2
```

```python
145         EBH=onsite_f2_h1
146         SA=onsite_s1
147         SAH=onsite_s1_h1
148         SB=onsite_s2
149         SBH=onsite_s2_h1
150         EAB=trans_fab
151         EABH=trans_fab_h1
152         SAB=trans_sab
153         SABH=trans_sab_h1
154
155         c=(SA+SAH)*(SB+SBH)-(SAB/2+SABH/2)**2
156
157         G11=1/c*((SB+SBH)*(EA+EAH)-(SAB/2+SABH/2)*(EAB/2+EABH/2))
158         G22=1/c*((SA+SAH)*(EB+EBH)-(SAB/2+SABH/2)*(EAB/2+EABH/2))
159
160         t_eff=np.sqrt(ESD**2-(G11-G22)**2)/2
161
162         add_data=np.array([G11,G22,ESD,ESD_DFT])
163         """OUTPUT"""
164         print "-------------------------------"
165         print "Block decomposition method..."
166         print "Florian Mayer / TUGraz 2018"
167         print "-------------------------------"
168         print "Inputs:"
169         print "Dimer state I: "+str(state_d)+" | Dimer state II: "+str(state_d+pickstate)
170         print "-------------------------------"
171         print "Detailed Results / eV :"
172         print "E_1  (onsite energy)  : "+str(G11)
173         print "E_2  (onsite energy)  : "+str(G22)
174         print "E_12 (splitting BD )  : "+str(ESD)
175         print "E_H  (HOMO energy)    : "+str(onsite_f1+onsite_f2+trans_fab)
176         print "E_Hm1(HOMOmebergy)    : "+str(onsite_f1_h1+onsite_f2_h1+trans_fab_h1)
177         print "S_H  (overlap HOMO)   : "+str(onsite_s1+onsite_s2+trans_sab)
178         print "S_hm1(overlap Hm1 )   : "+str(onsite_s1_h1+onsite_s2_h1+trans_sab_h1)
179         print "ESD  (splitting DFT)  : "+str(ESD_DFT)
180         print "ESD/2                 : "+str(ESD_DFT/2)
181         print "E_1-E_2 (onsite spl)  : "+str(G11-G22)
182         print "ESD-E_12 (hybrid hf)  : "+str(ESD_DFT-ESD)
183         print "-------------------------------"
184         print "Electronic coupling t_eff / meV"
185         print "t_eff : "+str(t_eff*1000)
186         print "-------------------------------"
187         return t_eff,add_data
```

A.4 Source Code: Tight-Binding Main Functions

```python
"""
Tight Binding: Fitting Module
Created on 22.04.2019

@author: Florian Mayer
florian.mayer@student.tugraz.at
"""
import numpy as np
import lmfit
from lmfit import Minimizer, Parameters, report_fit
import scipy.linalg as LA
import cmath as cm
from readinitialdata import *

def construct_parameters(mode,Raa,Rbb,Rab,r1,r2):
    """
    This function constructs the input for the tight_binding() fit function
    Inputs:
    mode="one" -> one molecule per unit cell
    mode="two" -> two molecules per unit cell
    Following Rxx parameters are linear combinations of lattice vectors
    Raa...Directions of fit parameters for molecule A
    Rbb...Directions of fit parameters for molecule B
    RAb...Directions of fit parameters for interactions between A and B
    r1...not used yet
    r2...not used yet
    """
    import numpy as np
    import cmath as cm
    from lmfit import Minimizer, Parameters, report_fit
    if mode=='one':
        Raa=Rbb

    if Raa.size==3:
        Raa=np.array([Raa])
    if Rbb.size==3:
        Rbb=np.array([Rbb])
    if Rab.size==3:
        Rbb=np.array([Rab])
    r1=np.array([r1])
    r2=np.array([r2])

    if mode[0]=='two':
        name_store=[]
        new_parameters=Parameters()
        for j in range(Raa.shape[0]):
            pa_name='t'+str(j)+'_AA'
            start_val=np.random.rand(1)*0.005
            new_parameters.add(pa_name,value=start_val, min=-10, max=10)
            name_store.append(pa_name)

        for j in range(Rbb.shape[0]):
            pa_name='t'+str(j)+'_BB'
            start_val=np.random.rand(1)*0.005
            new_parameters.add(pa_name,value=start_val, min=-10, max=10)
            name_store.append(pa_name)

        for j in range(Rab.shape[0]):
            pa_name='t'+str(j)+'_AB'
            start_val=np.random.rand(1)*0.005
            new_parameters.add(pa_name,value=start_val, min=-15, max=15)
            name_store.append(pa_name)
    if mode[0]=='one':
        name_store=[]
        new_parameters=Parameters()
        for j in range(Raa.shape[0]):
            pa_name='t'+str(j)+'_AA'
            start_val=np.random.rand(1)
            new_parameters.add(pa_name,value=start_val, min=-15, max=15)
            name_store.append(pa_name)
        for j in range(Rab.shape[0]):
            pa_name='t'+str(j)+'_AB'
```

```python
                    start_val=np.random.rand(1)
                    new_parameters.add(pa_name,value=start_val, min=-15, max=15)
                    name_store.append(pa_name)
        meta_data=np.array([Raa.shape[0],Rbb.shape[0],Rab.shape[0],r1.shape[0],r2.shape[0]])
        R=[Raa,Rbb,Rab,r1,r2]
        R=np.concatenate([[Raa],[Rbb],[Rab],[r1],[r2]],axis=1)
        R= np.squeeze(R)
        return name_store,new_parameters,R,meta_data


def tight_binding(pars,k,R,pa_names,meta,mode,S_dat=None,data=None):
    """
    pars... parameters needed to fit the function(construct_parameters delivers the
    right one)
    k...k_point vector in the shape of (n,3)
    R...position vector (construct_parameters delivers the right one)
    pa_names... list of parameter names (construct_parameters)
    meta... array of meta data, needed to build model function
    data... array of comparable data in the shape of (n,1)
    """

    overlap_c=mode[1]
    parvals = pars.valuesdict()
    t=np.zeros((len(pa_names),1))
    for j in range(len(pa_names)):
        t[j]=parvals[pa_names[j]]
    if mode[0]=='two':
        #next step: build the model function for two molecules per unit cell
        E_k_p=[]
        E_k_m=[]
        for i in range(k.shape[0]):
            H11_k_tot=[]
            H22_k_tot=[]
            H12_k_tot=[]
            H21_k_tot=[]
            for j in range(meta[0]):
                #here the H11(k) term is constructed:
                H11_k=t[j]*cm.exp(1j*np.dot(k[i,:],R[j,:]))
                H11_k_tot.append(H11_k)
            for j in range(meta[0],meta[0]+meta[1]):
                #here the H22(k) term is constructed:
                H22_k=t[j]*cm.exp(1j*np.dot(k[i,:],R[j,:]))
                H22_k_tot.append(H22_k)
            for j in range(meta[0]+meta[1],meta[0]+meta[1]+meta[2]):
                #here the H12(k) term is constructed:
                H12_k=t[j]*cm.exp(1j*np.dot(k[i,:],R[j,:]))
                H12_k_tot.append(H12_k)

            H11=sum(H11_k_tot)
            H22=sum(H22_k_tot)
            H12=sum(H12_k_tot)

            #finally we put things together and calculate the entire function
            if overlap_c=='No':
                E_p=(H11+H22)/2+np.sqrt((H11-H22)**2/4+np.abs(H12)**2)
                E_m=(H11+H22)/2-np.sqrt((H11-H22)**2/4+np.abs(H12)**2)
            #experimental, goes beyond tight-binding by including overlaps
            elif overlap_c=='Yes':
                eig_S=LA.inv(np.array([[S_dat[0][i],S_dat[2][i]],[S_dat[3][i],S_dat[1][i]]]))
                S11=eig_S[0,0]
                S12=eig_S[0,1]
                S21=eig_S[1,0]
                S22=eig_S[1,1]
                H21=np.conj(H12)
                E_p=(S11*H11+S12*H21+S21*H12+S22*H22)/2+np.sqrt(((S11*H11+S12*H21)-(S21*H12+S22*H22))**2/4+(S11*H12+S12*H22)*(S21*H11+S22*H21))
                E_m=(S11*H11+S12*H21+S21*H12+S22*H22)/2-np.sqrt(((S11*H11+S12*H21)-(S21*H12+S22*H22))**2/4+(S11*H12+S12*H22)*(S21*H11+S22*H21))
            E_k_p.append(E_p)
            E_k_m.append(E_m)
```

```
140
141         if mode[0]=='one':
142             #build model function for one molecule per unit cell
143             E_k_p=[]
144             E_k_m=[]
145             if data is not None:
146                 da_zw=data[0:data.size/2]
147                 data=np.concatenate((da_zw,da_zw))
148             for i in range(k.shape[0]):
149                 H11_k_tot=[]
150                 H12_k_tot=[]
151                 for j in range(meta[0]):
152                     #here we construct the H11 term:
153                     #not used in actual fit
154                     H11_k=t[j]*cm.exp(1j*np.dot(k[i,:],R[j,:]))
155                     H11_k_tot.append(H11_k)
156                     H11_k=0
157                 for j in range(meta[0]+meta[1],meta[0]+meta[1]+meta[2]):
158                     #here we construct the H12 term:
159                     H12_k=t[j-meta[1]]*cm.exp(1j*np.dot(k[i,:],R[j,:]))
160                     H12_k_tot.append(H12_k)
161
162                 H11=sum(H11_k_tot)
163                 H12=sum(H12_k_tot)
164                 #finally we put things together and calculate the entire function
165                 E_p=1.0*(H12)
166                 E_k_p.append(E_p)
167                 E_k_m.append(E_p)
168
169         cmp_dat=np.array([E_k_p,E_k_m])
170         func_val=np.squeeze(cmp_dat)
171         #print func_val.shape
172         cmp_dat=cmp_dat.flatten()
173         cmp_dat=cmp_dat.view(np.float)
174
175         if data is None:
176             return np.real(func_val)
177         else:
178             out=data-cmp_dat
179             return out.view(np.float)
180
181
182     def fit_bandstructure_two(k,data,Raa,Rbb,Rab,r1,r2,overlap_corr):
183         """
184         Wrapper for Tight-Binding fit with two molecules per unit cell
185         k...vector of k-points
186         data...reference data of DFT calculation/suitable shape is generated by read
                functions
187         Raa...Directions of fit parameters for molecule A
188         Rbb...Directions of fit parameters for molecule B
189         RAb...Directions of fit parameters for interactions between A and B
190         r_1,r_2 not used yet
191         overlap_corr="No"
192         """
193         mode=['two',overlap_corr]
194         names,para_set,R,metas=construct_parameters(mode,Raa,Rbb,Rab,r1,r2)
195         if overlap_corr=='Yes':
196             path22=''
197             S_dat2=read_entire_klist(path22,6,50,146)
198             minner = Minimizer(tight_binding, para_set, fcn_args=(k,R,names,metas, mode,
                S_dat2,data))
199         else:
200             S_dat2=[]
201             minner = Minimizer(tight_binding, para_set, fcn_args=(k,R,names,metas, mode,
                S_dat2,data))
202         result = minner.minimize(method='leastsq')
203         report_fit(result)
204         final = data + result.residual
205         new_para=result.params
206         plot_data=tight_binding(new_para,k,R,names,metas, mode, S_dat2,data=None)
207         return plot_data,new_para
208
```

```python
209   def fit_bandstructure_one(k,data,Raa,Rbb,Rab,r1,r2,overlap_corr):
210       """
211       Wrapper for Tight-Binding fit with one molecule per unit cell
212       k...vector of k-points
213       data...reference data of DFT calculation/suitable shape is generated by read
          functions
214       Raa...Directions of fit parameters for molecule A
215       Rbb...Directions of fit parameters for molecule B
216       RAb...Directions of fit parameters for interactions between A and B
217       r_1,r_2 not used yet
218       overlap_corr="No"
219       """
220       mode=['one','No']
221       S_dat2=[]
222       names,para_set,R,metas=construct_parameters(mode,Raa,Rbb,Rab,r1,r2)
223       minner = Minimizer(tight_binding, para_set, fcn_args=(k,R,names,metas, mode,
          S_dat2,data))
224       result = minner.minimize(method='leastsq')
225       report_fit(result)
226       final = data + result.residual
227       new_para=result.params
228       plot_data=tight_binding(new_para,k,R,names,metas,mode,data=None)
229       return plot_data,new_para
```

A.5 Source Code: Tight-Binding Effective Mass

```python
"""
Tight Binding: Effective Mass
Created on 22.04.2019

@author: Florian Mayer
florian.mayer@student.tugraz.at
"""
import numpy as np
from tight_binding_function_v02 import *

def analytical_effective_mass(pars,k,R,pa_names,meta,mode):
    """
    Calculates the effective mass for the one molecule per unit cell model function
    Inputs:
    pars...fit parameters derived with fit_bandstructure_one()
    k...k-point where the second derivative should be calculated
    pa_names...names of fit parameters
    meta...additional meta data -> output of fit_bandstructure_one()
    mode='one'
    Output:
    inverse effective mass tensor [3x3]
    """
    parvals = pars.valuesdict()
    t=np.zeros((len(pa_names),1))
    for j in range(len(pa_names)):
        t[j]=parvals[pa_names[j]]

    t=np.divide(t,27.211)
    k=np.divide(k,1.889725)
    R=np.multiply(R,1.889725)
    if mode[0]=='one':
        fin_dxdx=[]
        fin_dydy=[]
        fin_dzdz=[]
        fin_dxdy=[]
        fin_dxdz=[]
        fin_dydz=[]
        for i in range(k.shape[0]):
            dxdx_tot=[]
            dydy_tot=[]
            dzdz_tot=[]
            dxdy_tot=[]
            dxdz_tot=[]
            dydz_tot=[]

            for j in range(meta[0]+meta[1],meta[0]+meta[1]+meta[2]):
                dxdx=-(R[j,0]**2)*t[(j-meta[1])]*cm.exp(1j*np.dot(k[i,:],R[j,:]))
                dydy=-(R[j,1]**2)*t[(j-meta[1])]*cm.exp(1j*np.dot(k[i,:],R[j,:]))
                dzdz=-(R[j,2]**2)*t[(j-meta[1])]*cm.exp(1j*np.dot(k[i,:],R[j,:]))
                dxdy=-(R[j,0]*R[j,1])*t[(j-meta[1])]*cm.exp(1j*np.dot(k[i,:],R[j,:]))
                dxdz=-(R[j,0]*R[j,2])*t[(j-meta[1])]*cm.exp(1j*np.dot(k[i,:],R[j,:]))
                dydz=-(R[j,1]*R[j,2])*t[(j-meta[1])]*cm.exp(1j*np.dot(k[i,:],R[j,:]))
                dxdx_tot.append(dxdx)
                dydy_tot.append(dydy)
                dzdz_tot.append(dzdz)
                dxdy_tot.append(dxdy)
                dxdz_tot.append(dxdz)
                dydz_tot.append(dydz)
            fin_dxdx.append(np.sum(dxdx_tot))
            fin_dydy.append(np.sum(dydy_tot))
            fin_dzdz.append(np.sum(dzdz_tot))
            fin_dxdy.append(np.sum(dxdy_tot))
            fin_dxdz.append(np.sum(dxdz_tot))
            fin_dydz.append(np.sum(dydz_tot))

        rec_eff=np.array([[fin_dxdx,fin_dxdy,fin_dxdz],[fin_dxdy,fin_dydy,fin_dydz],[
        fin_dxdz,fin_dydz,fin_dzdz]])
        print np.squeeze(np.real(rec_eff))
        return np.squeeze(np.real(rec_eff))
```